ANOMALOUS TRANSPORT OF MICROALGAE *Chlorella vulgaris* IN MICROFLUIDIC CHANNEL

NUR IZZATI BINTI ISHAK

FACULTY OF SCIENCE
UNIVERSITY OF MALAYA
KUALA LUMPUR

2018

ANOMALOUS TRANSPORT OF MICROALGAE *Chlorella vulgaris* IN MICROFLUIDIC CHANNEL

NUR IZZATI BINTI ISHAK

DISSERTATION SUBMITTED IN FULFILMENT OF THE REQUIREMENTS FOR THE DEGREE OF MASTER OF SCIENCE

DEPARTMENT OF PHYSICS
FACULTY OF SCIENCE
UNIVERSITY OF MALAYA
KUALA LUMPUR

2018

UNIVERSITY OF MALAYA
ORIGINAL LITERARY WORK DECLARATION

Name of Candidate: **NUR IZZATI BINTI ISHAK**

Matric No: **SGR140083**

Name of Degree: **MASTER OF SCIENCE**

Title of Project Paper/Research Report/Dissertation/Thesis ("this Work"):

ANOMALOUS TRANSPORT OF MICROALGAE *Chlorella vulgaris* IN MICROFLUIDIC CHANNEL

Field of Study: **EXPERIMENTAL PHYSICS**

I do solemnly and sincerely declare that:

(1) I am the sole author/writer of this Work;
(2) This Work is original;
(3) Any use of any work in which copyright exists was done by way of fair dealing and for permitted purposes and any excerpt or extract from, or reference to or reproduction of any copyright work has been disclosed expressly and sufficiently and the title of the Work and its authorship have been acknowledged in this Work;
(4) I do not have any actual knowledge nor do I ought reasonably to know that the making of this work constitutes an infringement of any copyright work;
(5) I hereby assign all and every rights in the copyright to this Work to the University of Malaya ("UM"), who henceforth shall be owner of the copyright in this Work and that any reproduction or use in any form or by any means whatsoever is prohibited without the written consent of UM having been first had and obtained;
(6) I am fully aware that if in the course of making this Work I have infringed any copyright whether intentionally or otherwise, I may be subject to legal action or any other action as may be determined by UM.

Candidate's Signature Date:

Subscribed and solemnly declared before,

Witness's Signature Date:

Name:

Designation:

ANOMALOUS TRANSPORT OF MICROALGAE *Chlorella vulgaris* IN MICROFLUIDIC CHANNEL

ABSTRACT

Transport phenomena occur in diverse natural and man-made processes, ranging from the diffusion of charge carriers in conductors, semiconductors, ion channels in biological systems, movement of the dust particles or microorganisms in media and data transport in communication networks. Normal diffusion is characterized by linear scaling of the mean square displacement (MSD) with respect to time and can be modelled using Brownian motion. Anomalous diffusion refers to deviation from this linear scaling law to follow MSD ~ t^{α}, with scaling exponent α used to classify the transport dynamics, namely sub-diffusion when $0 < \alpha < 1$ and super-diffusion when $1 < \alpha < 2$. This study examined the transport behavior of microalgae Chlorella *vulgaris* as particles through a microfluidic channel under different flow rate. The flow is controlled through a pressure driven system and the motion of the microalgae is observed using high-speed CCD video camera with suitable optical magnification. The particle trajectories were reconstructed from the recorded sequential images and the basic statistics and the MSDs were calculated. A numerical simulation of the particles transport in a microfluidic channel was carried using COMSOL Multiphysics software. For simplicity, the microalgae particles were treated as spherical naturally buoyant. In both microfluidic experiment and numerical simulation, scaling behavior of MSD, probability density function (PDF), and velocity autocorrelation (VCAF) of the particle were analyzed by resolving the displacement in the streamwise (flow) and perpendicular (wall-normal) directions. Regional variations of the flow characteristics at the near-walls and center regions of the channel were also investigated. The scaled Brownian motion (SBM) model with power-law MSD scaling and time-dependent diffusion coefficient was used to describe the MSD scaling behaviors. The results showed the presence of anisotropic anomalous transport in all the three flow regions with mixed sub-diffusive, normal and super-diffusive behavior in both longitudinal and transverse directions. Both experimental and numerical finding agreed on the transient scaling behaviors in the MSDs, but with different scaling exponent MSD. These findings are considered useful for optimizing the mixing process, the dispersion of the microalgae, and the flow implementation in the photobioreactor.

Keywords: Brownian motion, anomalous transport, scaled Brownian motion, microfluidic, *Chlorella vulgaris*

GERAKAN ANOMALI MIKRO-ALGA *Chlorella vulgaris* DALAM SALURAN MIKRO-BENDALIR

ABSTRAK

Fenomena angkutan berlaku di dalam pelbagai sistem semulajadi dan buatan manusia. Sebagai contoh, penyerapan dan lonjatan pembawa zarah di dalam konduktor dan semi-konduktor, serangan virus dalam sel, dan pergerakan organisma bersaiz mikro dan angkutan data dalam sistem komunikasi. Resapan normal boleh dicirikan berdasarkan sifat pengskalaan sesaran purata kuasa dua (SPKD) yang boleh dimodel mengunakan gerakan Brown. Resapan anomali ialah penyimpangan daripada sifat penskalaan linear di mana SPKD $\sim t^{\alpha}$, dengan eksponen pengskalaan α digunakan untuk mengkelaskan dinamik angkutan, yakni sub-resapan apabila $0 < \alpha < 1$ dan super-resapan apabila $1 < \alpha < 2$. Kajian ini melibatkan pengamatan kelakuan gerakan mikro-alga *Chlorella vulgaris* sebagai zarah melalui saluran mikro-bendalir pada kadar aliran yang berbeza. Aliran bendalir dikawal oleh sistem pemacu tekanan. Gerakan mikro-alga diperhatikan menggunakan kamera video CCD dengan pembesaran optik yang sesuai. Trajecktori zarah dijana berdasarkan siri imej yang telah direkod dan statistik asas dan SPKD telah dikira. Simulasi berangka gerakan zarah mikro-alga di dalam saluran mikro-bendalir dilakukan dengan perisian COMSOL *Multiphysics*. Zarah mikro-alga diandaikan bersifat sfera terapung. Bagi kedua-dua eksperimen saluran mikro-bendalir dan simulasi berangka, sifat penskalaan SPKD, taburan kebarangkalian, dan fungsi korelasi halaju zarah telah dikaji untuk komponen arah gerakan zarah selari, sejanjang dengan arah aliran. Perubahan dalam ciri-ciri angkutan di kawasan berhampiran dinding dan kawasan tengah saliran juga telah dikaji. Model gerakan Brown berskala dengan ciri SPKD dan pekali resapan bergantung kepada masa telah digunakan untuk menggambarkan kelakuan penskalaan SPKD yang dicerapi. Hasil dapatan menunjukkan kewujudan angkutan anomali yang tidak sekata di ketiga-tiga kawasan aliran dengan campuran ciri sub-resapan, resapan normal dan super-resapan dalam komponen gerakan selari dan sejanjang dengan arah aliran. Selain itu, hasil kajian daripada ekperimen dan simulasi bersetuju dengan kemunculan kelakuan penskalaan transien dalam SPKD, tetapi dengan eksponen resapan yang bebeza. Kajian ini dianggap berguna untuk mengoptimumkan proses campuran, penyebaran mikro-alga, dan operasi aliran dalam fotobioreaktor.

Kata Kunci: gerakan Brown, gerakan anomali, gerakan Brown berskala, mikro-bendalir, *Chlorella vulgaris*.

ACKNOWLEDGEMENTS

First and foremost, I would like to express my sincere gratitude to the One, the Most Near, that He may forgive me in possible errors of failing- which is due to none but myself. For myself, this study has been initiation in my spiritual and intellectual journeys to learn on the meaning of the intellectual humility.

There is course appreciation to my advisors, Prof. Dr. Sithi Muniandy and Assoc. Prof. Dr. Vengadesh for their guidance, support, and encouragement throughout the course. Without their brilliant, motivating and charismatic advices, this work will be nothing but in vain. The educational experience received from them and serious attitude towards work learned from them have undoubtedly contributed to my academic career development. Also, thank you to Prof. Dr. Phang Siew Moi and Dr. Victoria Ng who helped and advised me in biological aspects of these studies.

To my parents, whom constantly worried yet supported me in my decisions to continue my graduate studies, I am greatly indebted to them.

To Lee Say Hoe, who constantly helped me to stating up the experiment setup and managed to help me to overcome my insecurities in my own abilities.

To Prof. Dr. Tariq Ramadhan, whom I never personally met (he also never knew about my existence) through his spiritual and philosophical YouTube lectures that constantly gave me the spiritual energy to overcome some failure occurred during my studies.

This research was made possible by the supports of Science Fund from the Ministry of Higher Education of Malaysia under the Fundamental Research Grant Scheme (Grant No. FRGS: FP057-2014A) and the fund from the University of Malaya Research Grant (Grant No. UMRG: RP020A-14AFR).

Future is sometimes we thought we have it. Life is fragile.

TABLE OF CONTENTS

LIST OF FIGURES

LIST OF TABLES

LIST OF SYMBOLS AND ABBREVIATIONS

α : Scaling exponent

H : Hurst exponent

γ : Friction coefficient

ξ : Gaussian white noise/random force

D : Diffusion coefficient

μ_f : Fluid dynamic viscosity

ρ_f : Fluid density

ρ_p : Particle density

a_p : particle radius

H_{ham} : Hamaker constant

k_{Deb}^{-1} : Inverse of Debye parameter

k_B : Boltzman constant

Ma : March number

Q : Flow rate

T : Temperature

τ : Lag time

t_c : Transition time

Re : Reynold number

r_{eq} : Segré-Silberberg radius

NB_1 : Near wall boundary region 1

NB_2 : Near wall boundary region 2

C : Center region

Ca : Carotenoid content

Chl-a : Chlorophyll-a concentration

fps	:	Frame rate per second
BBM	:	Bold Basal medium
BM	:	Brownian motion
CCD	:	Charge coupled device
CFD	:	Computational fluid dynamic
CTRW	:	Continuous time random walk
EPS	:	Extracellular polymeric substance
FBM	:	Factional Brownian motion
FGN	:	Fractional Gaussian noise
MSD	:	Mean square displacement
NVACF	:	Normalized velocity autocorrelation function
OD	:	Optical density
PDF	:	Probability density function
SBM	:	Scaled Brownian motion
SFD	:	Single File Diffusion
TAMSD	:	Time average mean square displacement
VACF	:	Velocity autocorrelation function

LIST OF APPENDICES

CHAPTER 1: INTRODUCTION

1.1 Introduction

Transport phenomena occurred in variety of systems. From the volatility movement in stock market (Mandelbrot, 2010), the hopping of the electron across semiconductors (Schubert et al., 2013), motion of the protein carrier across complex cytoplasmic skeleton (Fujiwara et al., 2016), diffusion of water in white matter of brain (Novikov et al., 2014), and swimming of microorganisms (Koch & Subramanian, 2011). These examples of phenomena belong to the transport process called diffusion. The irregular motion of the pollen grain in fluid was observed by Robert Brown (1829) where he concluded that this type of motion is also possessed by inorganic matter. Einstein (1905) and von Smoluchowski (1906) independently, suggested the mechanisms behind this random motion or Brownian motion whereby the particles are thought to experience irregular motion due to collisions with surrounding fluid's molecules. Normal diffusion process is characterized by the mean and the variance or known as mean square displacement (MSD) (Mazo, 2002). Normal diffusion exhibits the linear dependence of MSD with time and the positions of the diffusing particles satisfying the Gaussian probability distribution. In fact, the deviation of the MSD from the linear scaling law give rise to the anomalous diffusion, where the particle dispersion can be either faster (super-diffusion or ballistic) or slower (sub-diffusion) than normal diffusion (Burada, et al., 2009).

Microalgae are known to display non-linear dynamic nature such as the swarming algae is able to perform long jumps as it migrates towards nutrient or very small jump as it is trapped by the environment (Kurtuldu et al., 2011). This dynamic motion exhibited by the microalgae (Figure 1.1) provide the exciting platform to probe on how nature adopt efficient survival mechanisms in harsh environments. For instance, the motile algae (swimmer) derived its own intrinsic energy via help of adenosine triphosphate (ATP) conversion or with “swim organ” such as cilia or flagella, which then respond to the stimulus (Ntefidou et al., 2003; Rusconi & Stocker, 2015). Interestingly, even without any “swim organ”, the non-motile (non-swimmer) microalgae take the advantage of their buoyancy to help them navigate across the environment for search of nutrients, sunlight and oxygen (Rusconi & Stocker, 2015; Walsby, 1976).

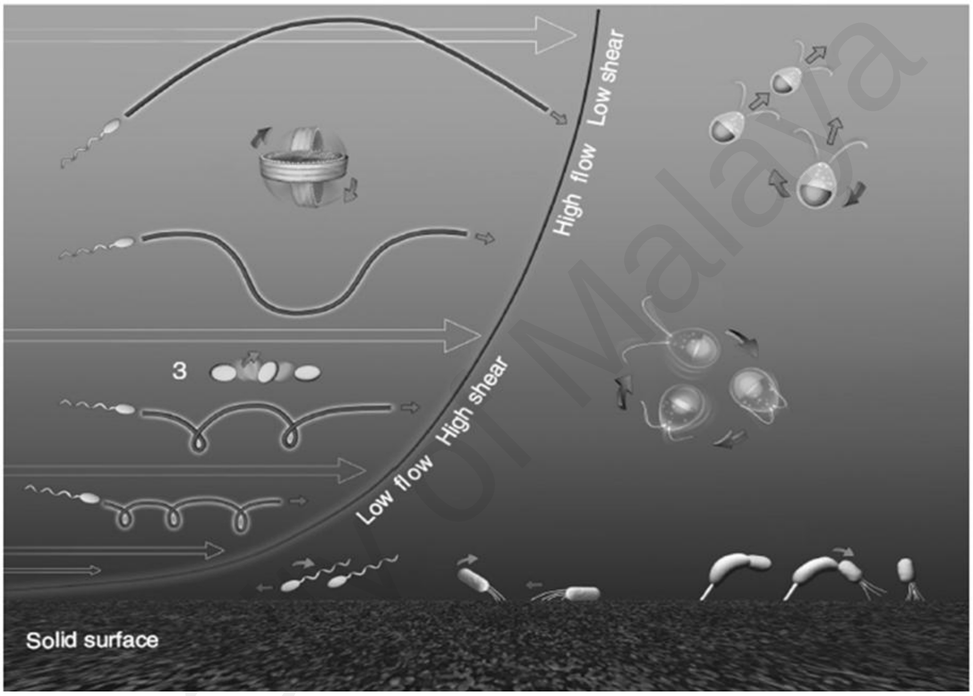

Figure 1.1: The different type of the differential survival mechanism of the microalgae (Rusconi & Stocker, 2015).

The use of microfluidic chip as a lab-on-chip device to study diverse flows and geometry effects on the transport of the particles are becoming increasingly popular (Meijering et al., 2012; Tasadduq et al., 2015; Yukimoto et al., 2013). Microfluidic chip allows the researchers to effectively control the micro-scale environment such as flow behavior (Kleßinger et al., 2013), fluid phases transition (Bardin et al., 2011), flow control (Beebe et al., 2000), mixing process (Lee et al., 2011), particles separation (Sajeesh & Sen, 2014), and particle focusing (Xuan et al., 2010). Combining with the high resolution and frame video microscopy and particle technique gives insight on the understanding of mechanics of microorganism in optimizing their motion. In this case, the microfluidic channel provides the confinement and flow environment to the system.

1.2 Complexity in transport processes

The micro-transport of algae can be further understood in term of “life at low Reynold numbers”, where viscosity of fluid dominated the transport process. High viscous environment can cause the algae to be trapped, causing its motion to be restricted (Bechinger et al., 2016). The presence of wall and surrounding geometry also can enhance the restriction on the algae motion (Yeo & Maxey, 2010). If the external driving force is present in the systems (e.g. moving fluid), the particle may no longer be able to freely diffuse (in open domain) or get trapped (in confined space) as the drift will force the particle to be transported along or against the streamlines (Burada et al., 2009). Since the applied flow is slower that swimmer velocity, the swimmer will manage to swim against the flow and vice versa (Apaza & Sandoval, 2016; Volpe et al., 2014). For the non-swimmer, due to its finite size particle property, it cannot move fixedly according to the streamline as when it gets close to the wall, it will bounce back to the streamlines and the presence of shear gradient forces the particle to balance their position to minimize the shear effect (Rusconi & Stocker, 2015).

1.3 Motivations of study

Inspired by the extensive research on phycology of microalgae at the Institute of Ocean and Earth Sciences (IOES), University of Malaya, there came an opportunity to study some physical aspects of these microorganisms. This led us to focus on a non-motile spherical freshwater unicellular alga, *Chlorella vulgaris* (*C. vulgaris*). Interestingly, they are widely studied for their usage as a source of biomass in biofuels production (Al-lwayzy et al., 2014; Sharma et al., 2012). The algae suspension is a complex fluid composed of water, polymeric substances and dissolved salts, algae cell and insoluble solids (Bolhouse, 2010). The presence of the polymeric substances such as extracellular polymeric substances (EPS) has shown to make algae suspension (Souliès et al., 2013) to behave as non-Newtonian fluid. Moreover, the presence of viscoelastic algae cells and cell debris also leads to non-Newtonian behavior (Leupold et al., 2013). In photobioreactor designs, algae dispersion is assumed to be tracer regardless of their motility (Rubio et al., 2004). The studies have shown that distribution of the cell dispersion will vary based on the response to the flow and nutrient (Bees & Croze, 2014; Croze et al., 2013). Hence, the algae suspension should be considered as active suspension, instead of treating it as the passive tracer. For the non-motile algae *Chlorella,* it can act as active suspension since its collective suspension modified the surrounding flow velocity (Rusconi & Stocker, 2015). Thus, there is a need for detailed understanding on the complexities of bio-particles transport under shear flow, particularly in confined geometries for optimal design, operation and efficiency of algae photobioreactor conversions.

1.4 Objectives

The objectives of this work can be summarized as the following:

i. to investigate the transport behavior of the microalgae in the microfluidic channel based on particle tracking experiment, trajectory analysis, and numerical simulation;

ii. to study the spatial variation of the transport behavior in different parts of the channel;

iii. to study the effects of flow rates on the mean square displacement temporal scaling for different regions of the channel; and

iv. to model the temporal regimes in the mean square displacement plots using generalized diffusion processes.

1.3 Thesis outline

Following a brief introduction to the research topic in Chapter 1, we recall the basic concepts related to normal diffusion and anomalous diffusion and the relevant diffusion models in Chapter 2. Here, we introduce some basics of fluid mechanics of the microfluidic system and emphasize on the algae used in this system. In Chapter 3, we present the methodology involved in this work, namely cell characterization, flow experiments and numerical experiment based on computational fluid dynamics. The image processing techniques and particles tracking/location identification algorithms are described here. Chapter 4 forms the core component of this thesis, where all the results obtained from the wet laboratory as well as numerical experiments are analyzed and discussed. These include the microalgae particle properties, particle trajectories and their mean square displacement characteristics, probability density functions for both the laboratory experiment and computational fluid dynamics. The study is concluded in Chapter 5 with brief remarks on stochastic modelling and anomalous diffusion together with prospects for further investigation.

CHAPTER 2: BACKGROUND AND LITERATURE REVIEWS

In this chapter, we present the basic concepts related to diffusion processes and the generalization to the broader classes of anomalous diffusion processes. There has been growing interest to model complex transport phenomena and we introduce a number of well-known stochastic processes that are capable of explaining the experimentally observed characteristics, which may be attributed to various causes originating from medium and particle properties and also external forces such as drift field. Algae phycology *Chlorella vulgaris* (*C. vulgaris*) is introduced in slight details to assist readers to appreciate this exciting organism. As these particles will be subjected to narrow channel flow experiment, a brief discussion on the relevant fluid dynamics of microfluidic systems is given to set the stage for the following chapter.

2.1 Normal Diffusion

When a drop of dye is added into the glass of water, the dye spreads out such that its concentration slowly decreased until it reached constant concentration everywhere in space. This phenomenon is known as diffusion and its described via Fick's second law given by (Mazo, 2002):

$$\frac{\partial}{\partial t}P(\mathbf{r},t)=D\ \frac{\partial^2}{\partial \mathbf{r}^2}P(\mathbf{r},t), \tag{2.1}$$

which relates the rate of diffusing species to diffuse at time t to the probability of diffusing species exist at space $\mathbf{r}$ at time t, and D is a diffusion constant. Equation (2.1) can be easily solved to give the probability of finding the particles at position $\mathbf{r}$ at time t as:

$$P(\mathbf{r},t)=\frac{1}{\sqrt{4\pi D}}e^{-\frac{\mathbf{r}^2}{4Dt}}. \tag{2.2}$$

This probability density distribution function (PDF) is the standard Gaussian or normal distribution profile as shown in Figure 2.1.

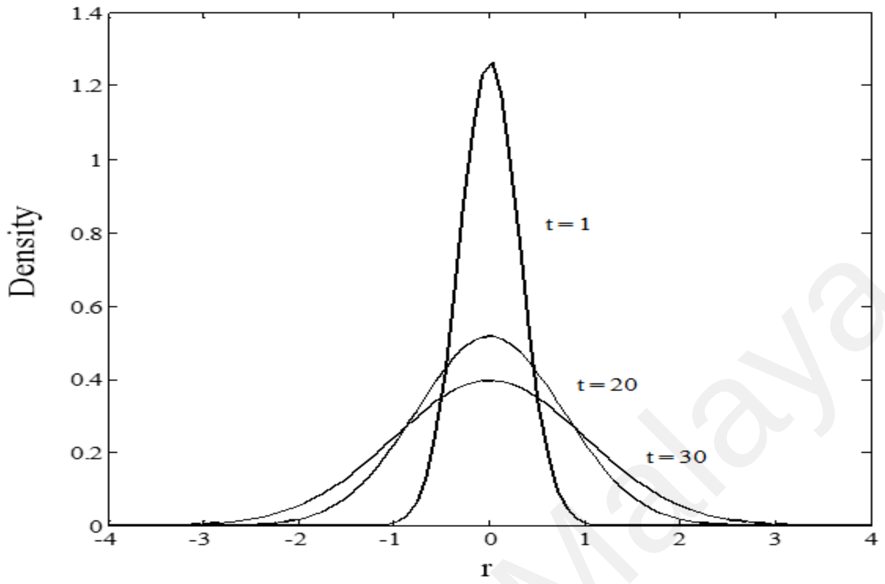

Figure 2.1: The probability of finding the particles at different positions r at dimensionless time *t* = 1, 20, 30.

As particles set in motion at time $t = 0$ with initial position $\mathbf{r} = 0$, the particles will spread across space, which is indicated by the increase of the width of particle's position density function. This spread is also known as the standard deviation of the distribution. The spread of the particle in space is described by the mean square displacement (MSD) which is

$$\langle \mathbf{r}^2(t) \rangle = \int \mathbf{r}^2 P(\mathbf{r},t)\, dt \propto t, \tag{2.3}$$

where $\langle \ldots \rangle$ referred to ensemble average and scales linearly with time t. The MSD is also referred to the variance of the distribution. Additionally, the empirical diffusion coefficient D can be obtained from Einstein diffusion relationship, $D = \lim\limits_{t \to \infty} \mathbf{r}^2\,(t)/4t$. (Mazo, 2002).

A concrete model to describe the diffusion process is random walk model, where each independent diffusing particle undergoes random walk of finite step to produce net displacement, which is a random variable. The particle has the independent increments of position **r** at two consequent intervals. This random path is called Brownian motion and the MSD is defined as:

$$\langle \mathbf{r}^2(\tau) \rangle = \langle [\, \mathbf{r}(t) - \mathbf{r}(t-\tau) \,]^2 \rangle \propto t \tag{2.4}$$

which has the same form as MSD in Equation (2.3).

A dynamical approach to treat the Brownian motion is to consider a stochastic differential equation, known as the Langevin equation, analogous to deterministic Newton's second law of motion but with added random noise term (Mazo, 2002). For the sake of the clarity, we consider the one-dimensional position (x) case only. The particle immersed in the fluid characterized by its position $\mathbf{x}(t)$ and velocity $\mathbf{v}(t)$ undergoes motion due to frictional drag forces $-\gamma \mathbf{v}(t)$ from the fluid and other deterministic forces **F** and affected by the random forces due to thermal noise $\xi(t)$ as shown below:

$$\frac{d\mathbf{x}(t)}{dt} = \mathbf{v}(t), \tag{2.5}$$

$$\frac{d\mathbf{v}(t)}{dt} = \mathbf{F} - \frac{\gamma}{m}\mathbf{v}(t) + \frac{1}{m}\,\xi(t), \tag{2.6}$$

where the friction coefficient $\gamma = 6\pi\eta a$ is given by Stokes law. Equation (2.6) reduces to the Newton's equation under absence of thermal forces. Thermal force $\xi(t)$ is defined as the random forces due to elastic collisions between the suspended particle with the surrounding fluid's particle. Since the impact of this force on the suspended particle varies extremely fast within the observed time, the characteristics of this forces are stochastically represented by standard Gaussian white noise such that the mean $\langle \xi(t) \rangle = 0$ and the delta correlation

$$\langle \xi(t_1)\xi(t_2) \rangle = \delta(t_2 - t_1). \tag{2.7}$$

The delta function is represented by Dirac delta function. It gives the information on the zero correlation between the collision occurring within the short time interval of dt_1 and dt_2. Within this short time interval, numerous collisions cause the memory of the forces to be lost at different time. A random process $X = \{X(t): 0 \leq t \leq \infty\}$ is called Brownian motion if it satisfies the following properties (Mazo, 2002):

(i) $X(t)$ and its increments $\{X(t_1)- X(t_2)\}$ has Gaussian distribution with zero mean;

(ii) correlation function $C(t_1 ,t_2) = <X(t_1).X(t_2)> = ½(|t_1|+|t_2|-|t_1-t_2|)$;and

(iii) variance $\langle (X)^2 \rangle \sim t$.

The white noise $\xi(t)$ is said to be the generalized derivative of the Brownian motion $X(t)$ and these two Gaussian stochastic processes are very important in the field of stochastic processes and the modelling of fluctuation phenomena (Mandelbrot, 2010). The sample paths of Gaussian white noise and Brownian motion are depicted in Figure 2.2. White noise is uncorrelated process, hence often used as model of extremely noisy phenomena without any memory or correlation between two consecutive time. Taking cumulative sum of the white noise would give the irregular path of the Brownian motion (Figure 2.2(b)) but with short-time correlation known as Markovian behavior, where the future is independent of the past given the present. Sample paths of Brownian motion exhibits the non-stationarity with irregularity of the path exists in all scales and differentiable nowhere. In fact, its path is statistically self-similar, namely the statistical distribution or the properties are invariant upon time scaling. This is referred to as fractal curves.

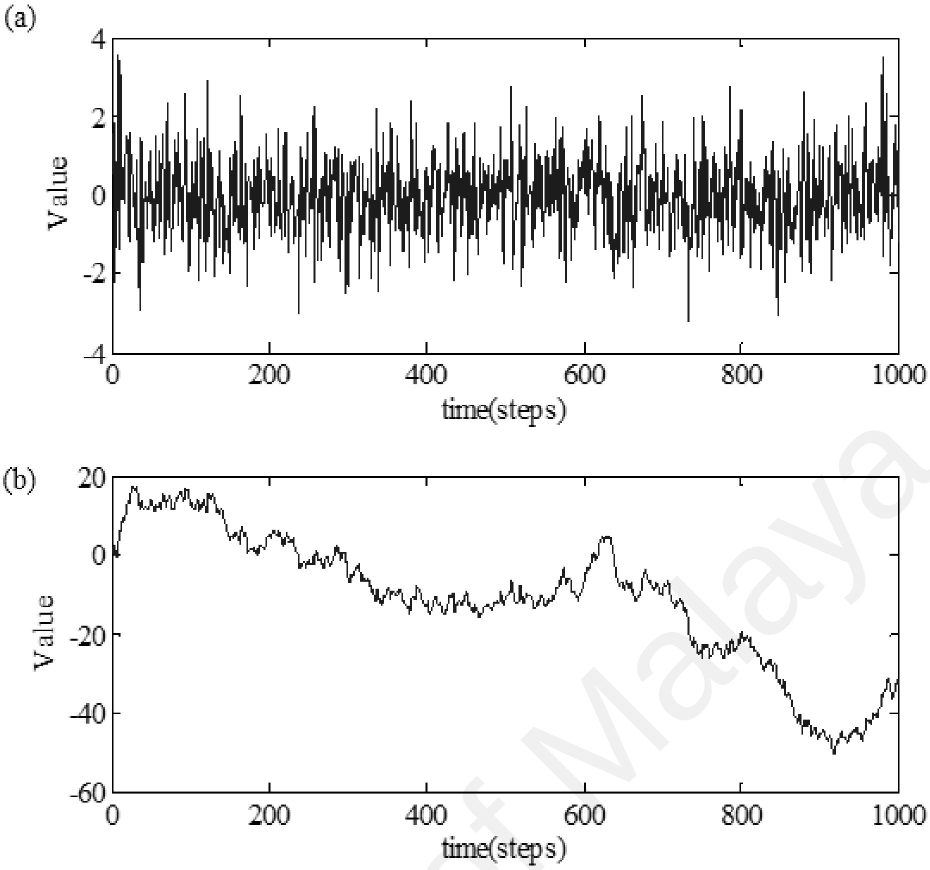

Figure 2.2: Sample path of: (a) white noise and (b) Brownian motion.

2.2 Anomalous diffusion

As mentioned earlier, Brownian motion and normal diffusion process have many properties that are easy to verify, either from theoretical analysis and also from experiment (Mazo, 2002). It is a Gaussian process characterized by the first two moments, namely mean and variance. Moreover, the linear scaling of MSD with time is rather unique and unambiguous. Nevertheless, there are many cases where departure from the normal diffusion behavior are observed. Any deviation from this standard linear behavior is referred to as anomalous diffusion (Metzler et al., 2014; Vlahos et al., 2008). A particular form of non-linear behavior of MSD is written as:

$$\langle \mathbf{r}^2(t) \rangle = \int \mathbf{r}^2 P(\mathbf{r},t)\, d\mathbf{r} = 2K_\alpha\, t^\alpha, \qquad (2.8)$$

such that $P(\mathbf{r}, t)$ is the probability of finding the particle at location $\mathbf{r}$ in time t, and K_α is the generalized diffusion coefficient with physical dimensions $\mathrm{cm}^2\mathrm{s}^{-\alpha}$. Based on this characteristic, it is possible to classify two main classes of processes based on scaling exponent α (Burada et al., 2009). For $0 < \alpha < 1$, the process is called sub-diffusion and $1 < \alpha < 2$ refers to super-diffusive behavior. Normal diffusion corresponds to $\alpha = 1$. When $\alpha = 2$, the transport is said to be ballistic as a signature of deterministic Newtonian dynamic. Moreover, when $\alpha > 2$, the process exhibits hyper-diffusive behavior (Siegle et al., 2010). Additionally, there exist other classes of the anomalous diffusion known as transient anomalous diffusion, where the system exhibits different scaling behavior depending on the transition time (Alves et al., 2016; Spiechowicz, et al., 2016):

$$\langle (\Delta \mathbf{r})^2 \rangle = \begin{cases} t^\alpha, & \text{for } t \ll t_{cr} \\ t, & \text{for } t \gg t_{cr} \end{cases}. \tag{2.9}$$

The notable phenomena that demonstrate the multi-scaling behavior depending on the transition time is single file diffusion (SFD) which will be discussed in next Section 2.4.4.

2.3 Stochastic models for anomalous diffusion

In this section, we introduce a number of stochastic models that can be used to describe anomalous diffusion. Before applying the model to the random process, one must perform the inspection on the distribution of the process to justify the suitable mathematical model that will fit the mechanisms of the process. One of the simple tests is the evaluation of the PDF by the system. Based on the PDF, one can then decide to use Gaussian anomalous diffusion models or non-Gaussian anomalous diffusion models as shown in Figure 2.3.

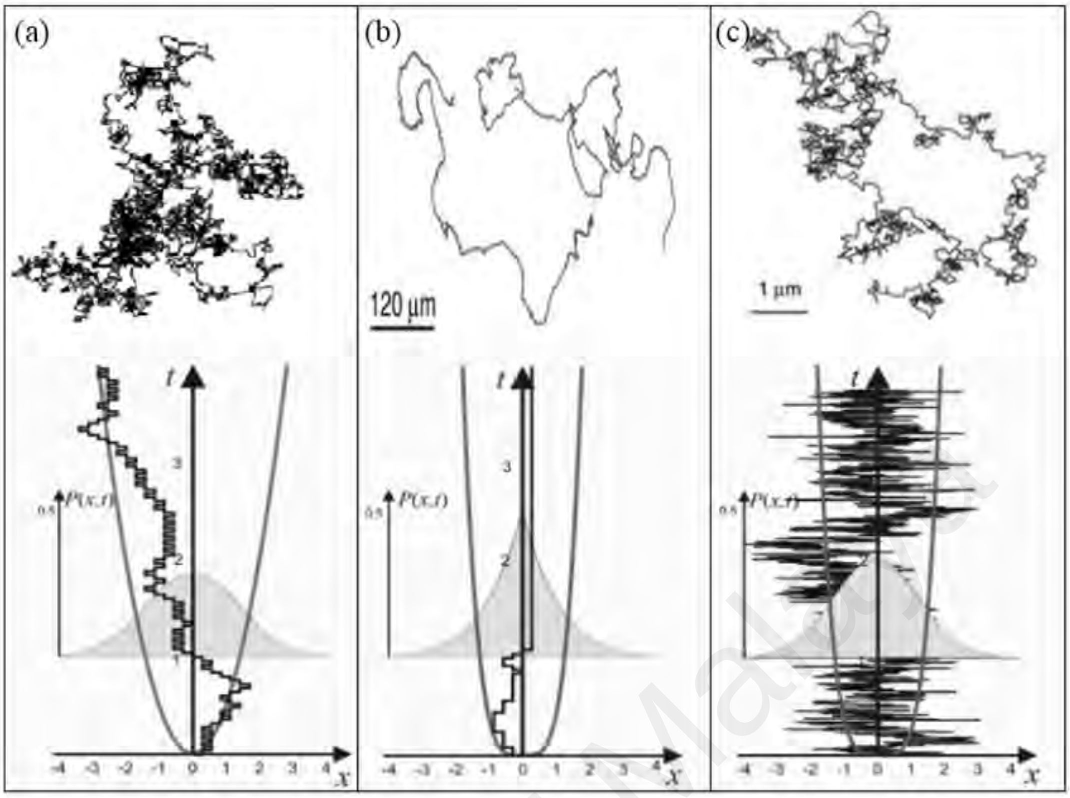

Figure 2.3: Trajectories of phenomena of (a) Gaussian normal diffusion modelled by random walk, (b) swarming bacteria migrate modelled by anomalous diffusion non-Gaussian model Levy's flight (Ariel et al., 2015), and (c) diffusion of single DNA molecule modelled by anomalous diffusion Gaussian model of Fractional Brownian motion (Serag et al., 2014).

2.3.1 Gaussian models for anomalous diffusion

In Gaussian anomalous diffusion, the random process exhibits the anomalous behavior in the MSD, yet retains the Gaussian property of its PDF. As such one can use the widely popular fractional Brownian motion (FBM) (Mandelbrot, 2010; Qian, 2003) or the scaled Brownian motion (SBM) (Bodrova et al., 2016; Bodrova et al., 2015; Jeon et al., 2014), which is not widely known beyond the community of stochastic processes researchers until recent. The application of the latter for this study would be considered as a significant contribution in the modeling of anomalous transport.

2.3.1.1 Fractional Brownian Motion (FBM)

Fractional Brownian Motion (FBM) is one of the Gaussian functions with strong interdependence between distant samples path. Because of these properties, FBM is used to model the cycles in economic time series (Bender et al., 2011; Mandelbrot, 2010), the fluctuations of $1/f$ noises in solids (Kaulakys & Alaburda, 2009), cumulated water flows in hydrology (Molz et al., 1997), and data transfer in network traffic (Willinger et al., 1995). In addition, FBM is commonly used to model the motion of the particle in the viscoelastic environment (Jeon et al., 2014; Reverey et al., 2015). The widely accepted stochastic representation of the FBM was introduced by Mandelbrot and van Ness (Mandelbrot & van Ness, 1968) as given by

$$B_H(t) := \frac{1}{\Gamma\left(H+\frac{1}{2}\right)}\left(\int_{-\infty}^{0}[(t\text{-}s)^{H\text{-}1/2}\,\text{-}(\text{-}s)^{H\text{-}\frac{1}{2}}]dB(s)+\int_{0}^{t}(t\text{-}s)^{H\text{-}\frac{1}{2}}dB(s)\right) \tag{2.10}$$

where Γ is the gamma function i.e. $\Gamma(\alpha) := \int_0^\infty x^{\alpha\text{-}1}\exp(\text{-}x)\,dx$ and $0 < H < 1$ is called Hurst parameter. Hurst parameter is the measure of self-similarity. The normalized fractional Brownian motion $B_H = \{B_H(t) : 0 \leq t \leq \infty\}$ is characterized by the following properties:

(i) $B_H(t)$ has stationary increments;

(ii) $B_H(0) = 0$ and $E[B_H(t)] = 0$ for $t \geq 0$;

(iii) $E[B^2{}_H(t)] = t^{2H}$ for $t \geq 0$; and

(iv) $B_H(t)$ has Gaussian distribution for $t \geq 0$.

In addition, fractional Brownian motion is the only Gaussian process with stationary increments that is self-similar. FBM is also a non-stationary process. For the continuous sample path, the covariance function of the FBM is given by:

$$C(s,t) = E[B_H(s)B_H(t)] = \frac{1}{2}\{t^{2H}+s^{2H} - (t\text{-}s)^{2H}\}. \tag{2.11}$$

For $0 < s \leq t$ the incremental process $W_H = \{W_{H_k} : k = 0,1, \dots .\}$ of FBM is given by

$$W_H = B_H(k+1) - B_H(k), \tag{2.12}$$

and it is called as Fractional Gaussian Noise (FGN) corresponding to the white noise counterpart of Brownian motion. The differentiation the FBM produces the corresponding FGN, while the integration of FGN gives rise the corresponding FGN. It should be noted FGN is the stationary process. The FGN correlation function is given by (Qian, 2003):

$$C(s,t) = \frac{1}{2}[(t-s-1)^{2H} - 2(t-s)^{2H} + (t-s+1)^{2H}]. \tag{2.13}$$

Via the stationary property of FGN, the correlation at lag time τ reduces to:

$$C(\tau) = \frac{1}{2}[(\tau+1)^{2H} - 2(\tau)^{2H} + (\tau-1)^{2H}], \tag{2.14}$$

and for the large τ, Equation (2.14) can be approximated as:

$$C(\tau) = H[(2H-1)\tau^{2H-2}]. \tag{2.15}$$

Similar with FBM, FGN is a fractal stationary process characterized by the Hurt Exponent *H*. While FBM contains the information on displacement of diffusing particles, FGN can be used to model the velocity or derivative process using the correlation properties. In this case, *H* value determines the memory or the long-range dependency of the FGN process (Koutsoyiannis, 2002; Riley et al., 2012; Shevchenko, 2015). If $0 < H < 0.5$, the process has the short time memory (anti-persistent) with negative correlation as the positive increment is followed by negative increment. For $0.5 < H < 1$, the process has long time memory (persistent) with positive correlation where the positive increment is often followed by positive increment. As $H = 0.5$, the process reduces to white noise with zero correlation (uncorrelated).

2.3.1.2 Scaled Brownian motion (SBM)

Scaled Brownian motion (SBM) occurred in variety of the systems, for example the diffusion of water in the brain (Novikov et al., 2014), and the motion of particle across porous environment (Sen, 2004). It is a Gaussian stochastic process and is derived by rescaling Brownian motion $B(t)$ via the non-liner time transformation (Lim & Muniandy, 2002):

$$t \rightarrow t_* = t^{\alpha}, \quad 0 < \alpha < 2 \tag{2.16}$$

Then, the SBM $B_s(t) \equiv B(t_*)$ is Gaussian process with zero mean. The correlation function is given by:

$$\langle B(t_*) B(s_*) \rangle = t_* \wedge s_* = t^{\alpha} \wedge s^{\alpha} = \langle B_s(t) B_s(s) \rangle, \tag{2.17}$$

where $\wedge$ denotes the minimum. The SBM can then be represented in Langevin equation form with the time dependent diffusion coefficient $D(t)$ as (Jeon et al., 2014):

$$\frac{dB_s}{dt} = \sqrt{2D(t)}\, \xi(\tau), \tag{2.18}$$

where $D(t)$ takes the general form of

$$D(t) = D_0 + (1 + \frac{1}{\tau_0})^{\alpha\text{-}1}, \tag{2.19}$$

with $D_0 = D(0)$, the initial diffusion coefficient with physical dimension of $\mathrm{cm}^2\mathrm{s}^{-\alpha}$. This general form avoids the singularity at $t = 0$ and τ_0 represents a characteristic time for the mobility variation. In SBM, scaling exponent α of the MSD takes the range of $0 < \alpha < 2$ so that the process describes sub-diffusion with $0 < \alpha < 1$, Brownian motion with $\alpha = 1$, super-diffusion with $1 < \alpha < 2$, and ballistic with $\alpha = 2$. SBM retains the basic properties of the Brownian motion such as it has Gaussian Markov process for $t > 0$, thus should be favourable for modeling Gaussian fractal signals.

2.4 Non-Gaussian anomalous diffusion

The central assumption of the Brownian motion lies in the implication of Central Limit Theorem (CLT) on the distribution of the particle's displacement (Mazo, 2002; Metzler et al., 2014). From the probability theory, if the steps taken by the particle when it undergoes the random walk are independent, then the distribution of particle's displacements follow the Gaussian distribution at sufficiently long time. In other words, CLT guarantees the strong convergence of any identically and independent distributed random variable (iid) into Gaussian distribution, regardless of the initial distribution of those iid. The direct consequence of the CLT is shown in ensembles averaged over a set of initial states (ergodic behavior) in the definition of the MSD (Metzler et al., 2014). This leads to the ergodic breaking phenomena (Jeon et al., 2014; Metzler et al., 2014). The violation of the CLT leads to another class of anomalous diffusion called non-Gaussian anomalous diffusion.

Two examples of non-Gaussian anomalous diffusion models are continuous-time random walk (CTRW) and Levy's flight.

2.4.1 Continuous-Time Random Walk Model

As the result of the violation of CLT, the particle in CTWR no longer has constant jump length. CTRW model has been successfully used to describe the motion of charge carrier in amorphous semiconductor (Scher & Lax, 1973), the trajectories of insulin's granule across a potassium channel (Tabei et al., 2013), and the motion of carrier proteins in plasma membrane of a live cell (Campagnola et al., 2015). These phenomena reflect the particles or walkers encounter traps or obstacles as they walk along their path which cause the walkers to "wait" for a waiting period before they are free to move or jump (Berry & Soula, 2014). This successive jump does not take place at equal time step and the random process is a non-stationary process with dependent increment. The particle is assumed to have the power-law waiting time distribution described by (Metzler et al., 2014):

$$P(\tau) \sim \frac{\tau_0^x}{\tau^{1+x}}, \qquad (2.20)$$

before it can jump such that the typical waiting time τ diverges as limit $\tau \to \infty$ and $0 < \alpha < 1$. The fundamental time scale of the random process is expressed as scaling factor τ_0. Due to extreme waiting time of the individual particle, this leads to disparity between the MSD and time averaged MSD(TAMSD) $\delta^2(\tau)$ (Sokolov, 2012) namely

$$\langle x^2(\tau) \rangle \neq \lim_{t \to \infty} \overline{\delta^2(\tau)}, \qquad (2.21)$$

which implies weak ergodicity breaking as mentioned previously in Section 2.3.

2.4.2 Levy Flight

In Levy flight, the particle undergoes the independent increment of path taking a jump with length l_j at the j-th step, such that the jump length is derived from the power law probability density function

$$P(l) \sim l^{-\mu}, \qquad (2.22)$$

with $1 < \mu \ll 3$ (Viswanathan et al., 2008). When $\mu = 1$, the path exhibits the ballistic (deterministic) behavior and $\mu = 3$ leads to the Brownian motion. When $\mu < 3$, the path follows the anomalous diffusive behavior where its second moment diverges ($\langle l^2(t) \rangle \to \infty$). For $\mu < 2$, the first moment is divergent ($\langle x(t) \rangle \to \infty$). These divergences of moments are due to heavy tail characteristics of the distributions where the particle may experience extremely long jumps. The summation of the iid with divergence variance lead to generalized central limit theorem, where the limit of this distribution is characterized by α-stable Levy distribution (Viswanathan et al., 2008). In fact, the particle undergoing Levy's walk leads to super-diffusive behavior of the MSD defined as:

$$\langle x^2 \rangle \sim t^{2H}, \tag{2.23}$$

which scales super-linearly with time. The foraging hypothesis on the Levy's flight states that the biological organism's movement will adapt to the Levy's flight to optimize their random search translation for the food, nutrients, territory and etc. (Viswanathan et al., 1999).

2.5 Factors affecting the transport processes

Transport phenomena exhibit diverse characteristics depending on the media complexity, type of particle, flow, and geometry of the confinement. The interaction of the particles with all these factors give rise to complex and non-linear dynamics. In the following, we list a few key contributions, but the list is not exhaustive.

2.5.1 Types of media

In open spatial domain, a particle suspended in water is free to explore the space with the MSD of the particle characterized by linear dependence following the Einstein's diffusion law (Mazo, 2002). However, if the water is replaced with complex media for example polymer, the motion of the particle will be restricted. For instance, the viscoelastic media such as polymer produces anomalous diffusion such that tracers are trapped due to the polymer entanglement (Godec et al., 2014; Mutch et al., 2013). In addition, the liquid-glass transition mechanism (Gimel & Nicolai, 2011) can induce the anomalous behavior, where the existence of the transient anomalous regime at a short time is followed by the normal diffusion at the long time (Godec et al., 2014). Complex media such as cytoplasm (Guigas et al., 2007; Reverey et al., 2015; Weiss et al., 2004) cause the passive tracers to exhibit anomalous diffusion. The complex cytoskeletal elements such as microtubule and actin filaments that make-up cytoplasm provide the obstructions on the diffusing particle (Sokolov, 2012). The degree of the obstruction can alter the translational diffusion region for instance, the particle exhibits a short time sub-diffusive motion and transit to the normal diffusion at the longer time (Havlin & Ben-Avraham 1987; Weiss et al., 2004). Another example is the existence of the transient anomalous sub-diffusive motion of tracers in the living motile *Amoeba* at short time interval due to caging of viscoelastic thermal bath before transition to the super-diffusive behavior at later time because of advective flow of the moving cell (Rogers et al., 2008). Heterogeneity in the fluid can affect the transport of the particle. For example, differences of fluid's constituent particles (Figure 2.4) can lead to restriction of the particles motion due to the molecular crowding effect (Banks & Fradin, 2005; Weiss et al., 2004).

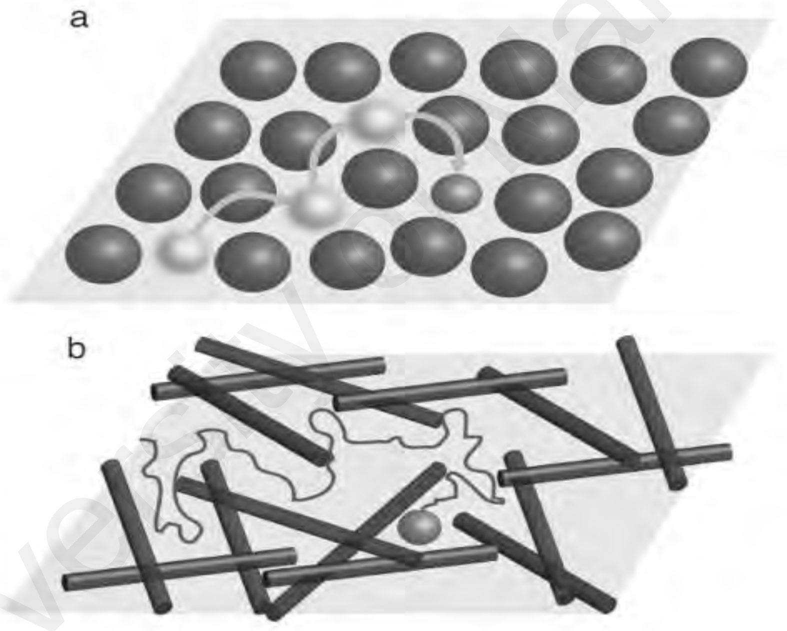

Figure 2.4: (a) Disordered medium, (b) crowded environment (Condamin et al., 2008).

2.5.2 Types of particles

Micro-spherical hard particles immersed in the fluid undergoes random motion and its MSD often found to scale linearly with time (Mazo, 2002). Unlike the hard-particle, the soft particle tends to show deviation from linear scaling law of the MSD, mainly due to complex interaction of particle elasticity, shape factor, and surface interaction, fluid hydrodynamic forces (Lin et al., 2009), and the confinement geometries (Chebbi, 2015; Chen, 2014; Ghosh et al., 2015; Nutku & Aydıner, 2015). This complex interaction induces rich non-linear dynamics on the system. The soft particle such as a single mesenchymal-like cell is able to change its shape due to sub-cellular activities. During the cell locomotion, the relative motion of the cell with respect to its nucleus displayed different anomalous regimes, depending on the cell's protrusion and detachment activities. The mixture of detachment and protrusion activities caused the cell to display the diffusive behavior while the nucleus dispersed sub-diffusively (Lan et al., 2016). Another example is the shear thinning behavior of blood flow through the micro veins where the decrease of blood viscosity with respect to increasing shear rate depends on the diameter of blood vessel relative to cell size and shear rate (Chen, 2014).

The soft-core nature of the particle opens up possibilities of the inelastic collisions, particles deformation, and non-uniform mass distribution subjected to external forces i.e. shear force (Tam & Hyman, 1973). A deformable particle produces asymmetric hydrodynamic field and unbalanced fluid stress at the particle's surface causing the net migration of the particles to be away from the wall (Chen, 2014). Besides, the difference of the particle's surface velocity with the flow's velocity induces cross stream lateral migration, where the particle can migrate in the perpendicular direction of the streamlines (Ho & Leal, 1974). Additionally, the particle can undergoes deformation due to fluid's shear and hydrodynamic perturbation (Chen, 2014; Hur et al., 2011).

Without any influences of any external forces, motion of the passive micro-particle is driven by the thermal fluctuation of the medium (Mazo, 2002). In contrast, active particle is able to propel by acquiring the energy from the environment and help it to move in certain swimming direction (Ao et al., 2014). Active particle is also known as self-propelled particle or micro-swimmer or nano-swimmer, and they are plenty in nature and artificial systems. An example of artificial swimmer is Janus particle, where its motion is triggered by the surrounding chemical reaction (Bechinger et al., 2016). An experimental together with simulation study by Zheng et al. (2013) reveals the non-Gaussian anomalous diffusion exhibited by Pt-silica Janus particles. They found that the particles showed Brownian motion dynamics at early time, switched on to super-diffusion at the intermediate time and then recovered the diffusive dynamics at longer time.

For the natural swimmer such as motile microalgae performed the directed motion based on its stimulus reaction on the environment such as gravitaxis (bias towards gravity) and phototaxis (bias towards the light). Gravitaxis is bias experienced by the motile organisms due to the gravitational field (Hagen et al., 2014). Negative gravitaxis is motion experienced by the motile organisms to opposed the gravitational field, which are observed in *Paramecium* (Roberts, 2010) and *Chlamydomonas* (Roberts, 2006), which used the swimming organ such as flagella or cilia to navigate in the flow to avoid the sedimentation. Another example is the *Euglena gracilis* which used the combination of the phototaxis (respond to light) and gravitaxis to retain the vertical alignment in water, enabling them to adjust their position to optimize the surface for sunlight irradiation (Ntefidou et al., 2003). This system has been shown to exhibit non-Gaussian anomalous diffusion (Leptos et al., 2009) with the diffusive behavior in the horizontal direction while ballistic behavior in the vertical direction (Schuech & Menden-Deuer, 2014). It should be noted that the gravitaxis also occurred in non-motile organism where the inhomogeneous mass density within organisms (bottom heaviness) cause the organisms to align with sea buoyancy (Roberts, 2006, 2010).

2.5.3 Types of flow

Classical problem of transport of tracer under influence of the Poiseuille velocity flow profile was done by Taylors (1953). The study observed that the particles distribution approached symmetrical Gaussian distribution at the limit of large time and the particle diffused axially with larger effective diffusion coefficient than normal diffusion. Non-Gaussian particle distribution at the short time regime was also noticed in this work. Taylor's results were improved by Aris (1956) where he approximated the value of effective diffusion coefficient as $D_{eff} = 1/(192D)+D$. Early observation of the anomalous diffusion in fluid dynamic problems was noted by Lighthill (1966), who observed that particles spread dispersively before the Taylor regime. Latini and Bernoff (2001) revisited the problem with the conclusion that the tracer dispersion exhibited transient anomalous diffusion with the diffusive regime at short time, the anomalous super-diffusive regime at the intermediate time, and Taylor's regime at a long time. In addition, they suggested that the transient anomalous diffusion at the time before Taylor's regime is a feature of the shear dispersion in laminar flow (Latini & Bernoff, 2001).

Shear flow also affects the dynamics of the transport process. For instance, the formation of the structural inhomogeneity or ordering at higher shear rate can cause the anisotropy in diffusion coefficient that creates the out-of-equilibrium structure (Cheng et al., 2012; Zausch et al., 2008). For instance, Cheng et.al (2012) reported the concentrated hard sphere particles suspension in simple shear flow arranged themselves in a string-like structure in vorticity direction as result of the anisotropic particle diffusion. Under the shear flow, the MSD of passive Brownian spherical particles along the streamwise direction exhibit anomalous scaling proportional to the cubic power of time (Katayama & Terauti, 1996; van de Ven, 1977). Recent numerical study on the behavior of Brownian self-driven particles at low Reynolds number in Poiseuille flow showed that the MSD along the flow direction in short time follows quartic time scaling behavior, whereas at longer time, it is always quadratic in time (Apaza & Sandoval, 2016).

2.5.4 Geometrical confinement

Particles are free to explore the bigger spatial space in open geometry. Particles' random motion in such cases shows MSD that scales linearly with time. When geometric spatial confinement is introduced in the form of a narrow channel as shown in Figure 2.5, then the transport process exhibits rich non-linear dynamics. For example, the presence of confining wall causes the MSD of the particles to become smaller because the particles transported near to the wall experience particle-wall interaction. A study on the non-colloidal suspensions under shear flow and bounded by two parallel walls using microfluidic chip was carried out by Yeo and Maxey (2010). They observed the diffusion of particles in tangential direction in vicinity of the wall behave super-diffusively as the particles undergo intermittent jumps, while the particles located at the center of the channel diffused sub-diffusively due to confinement by the walls. In addition, the surface roughness (Fehr & Lowen, 1995; Scheidler et al., 2000) also affect the local behavior of the particle such that the smooth wall will induce smaller MSD of particles (Eral et al., 2009).

Under very extreme confinement geometry i.e. very narrow channel, the particles undergo strong sub-diffusive dynamics such that the particles are lined-up in sequence, and incapable for mutual passage (Figure 2.5(c)). This phenomenon is called single file diffusion (SFD) and the particle's sequences remain unchanged over time (Burada et al., 2009). By using optical video microscopy imaging and particle tracking technique to track the motion of paramagnetic colloidal spheres inside the micro-trenches, Wei et al., (2000) reported this system exhibited the SFD dynamic in which MSD scales as $t^{1/2}$ over the period of two decades and the PDF of the particles displacements is Gaussian.

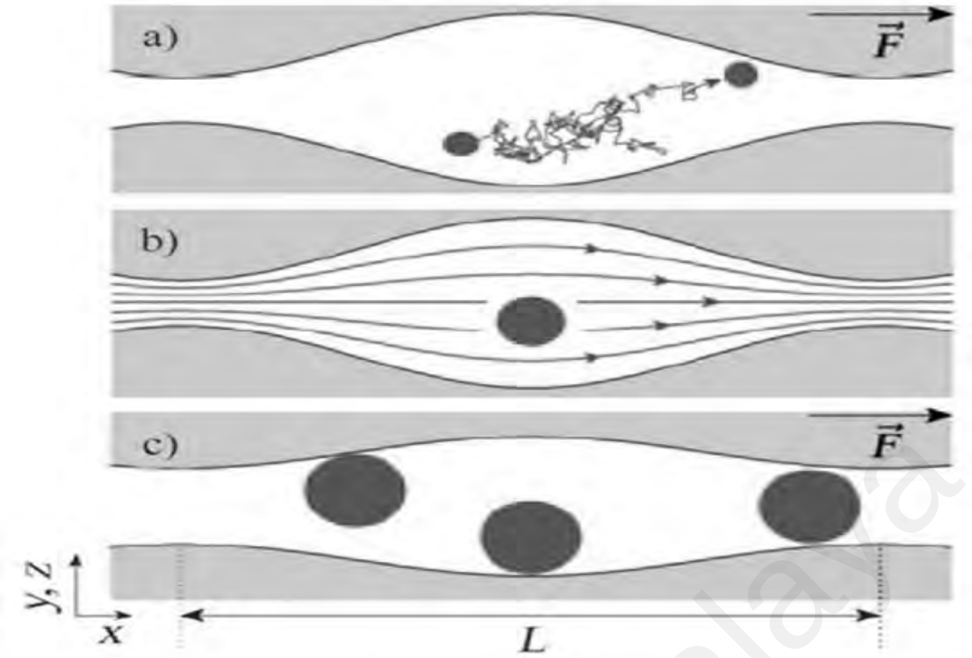

Figure 2.5: Transport of particles in narrow channels under condition of (a) without applied flow, (b) with applied laminar flow, and (c) with extreme confinement. Image retrieved from (Burada et al., 2009).

2.6 Algae phycology

C.vulgaris is the unicellular and non-motile (no flagellum) green algae that grows abundantly in the fresh water, brackish water and in terrestrial habitat (Sharma, 2007). It has spherical, ellipsoidal, or granular shape and with an average diameter of 2 µm~ 20µm (Sharma, 2007). The algae's cell wall (Figure 2.6) is made up from cellulose/chitin-like glycan, which gives them a quite rigid membrane structure (Kapaun & Reisser, 1995) and therefore can sustain relatively high hydrodynamic stresses without any cellular damage. *C.vulgaris* is a neutrally buoyant cell where its effective density is similar to the suspending water (Reynolds, 1984). Thus, it freely floats on the water surface by undergoes vertical migration towards the region with abundant of light (Viner & Kemp, 1983).

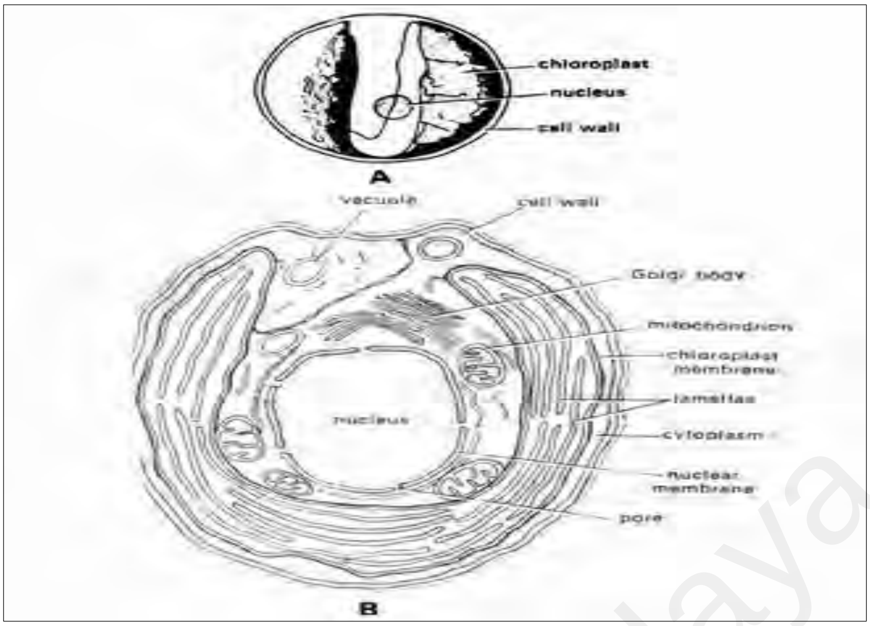

Figure 2.6: Structure of *Chlorella vulgaris* (Sharma, 2007).

Due to its ability to produce high lipid content, *C.vulgaris* is widely studied for its usage as a source of biomass in biofuels production (Al-lwayzy et al., 2014; Sharma et al., 2012). The algae suspension is a complex fluid composed of water, polymeric substances and dissolved salts, algae cell and insoluble solids (Bolhouse, 2010). The presence of the polymeric substances such as extracellular polymeric substances (EPS) has shown to make algae suspension (Souliès et al., 2013) to behave as a non-Newtonian fluid. Moreover, the presence of viscoelastic algae cells and cell debris also leads to non-Newtonian behavior (Leupold et al., 2013).

2.6.1 Algae as complex fluid

Algae suspensions are composed of water, polymeric substances and dissolved salt making it to behave as a complex fluid. Extracellular polymeric substances (EPS) is produced by the microorganisms in the medium as the result of its microbial metabolism (Mayer et al., 1999). EPS is composed of carbohydrates, protein, extracellular DNA, lipid, surfactants, and humid substances. In fact, the EPS also consist of a viscous biofilm matrix (Marvasi et al., 2010; More et al., 2014). The presence of EPS can cause the suspension to exhibit non-Newtonian fluid behaviors (Clementi et al., 1998). In addition, cell debris and viscoelastic algae cell also can contribute non-Newtonian behaviors of the suspensions (Chen et al.,1997).

2.6.2 Viscosity of algae suspension

The effective viscosity of the dilute suspension of the non-interacting hard sphere particle suspended in the Newtonian fluid can be approximated by using Einstein's classical viscosity model (Genovese, 2012; Mendoza et al., 2009):

$$\eta_r = \frac{\eta_s}{\eta_{sw}} = 1 + 2.5\phi, \tag{2.24}$$

where η_r is relative viscosity, η_s is suspension viscosity, η_{sm} is suspending medium viscosity, and ϕ is particle volume fraction. This equation is valid for $\phi < 0.01$, so that flow around the particle does not disturb the velocity field of any particles (Genovese, 2012; Mendoza & Santamaría-Holek, 2009).

At high particles concentration or high-volume fraction, the hydrodynamic interaction between the particles is more significant. The two-particle hydrodynamic interaction is considered in viscosity model developed by Batchelor and given by:

$$\eta_r = 1 + 2.5\phi + 6.2\phi^2, \tag{2.25}$$

valid for $\phi < 0.1$ (Batchelor, 1977). In high particle volume fraction, the concentration of the particles can be related to the viscosity through the empirical formulation by Krieger and Dougherty:

$$\eta_r = \left(1 - \frac{\phi}{\phi_{max}}\right)^{-2.5\phi_{max}}, \tag{2.26}$$

where ϕ_{max} is the maximum packing fraction (Krieger & Dougherty, 1959). This equation will reduce to the Einstein model at low particle volume fraction. In addition, at maximum packing fraction such that $\eta_r \rightarrow \infty$, Quemada (1977) proposed the viscosity model as:

$$\eta_r = \left(1 - \frac{\phi}{\phi_{max}}\right)^{-2}. \tag{2.27}$$

A systematical study on the rheological properties relationship with the volume fraction of the *C. vulgaris* suspensions was done by Souli`es et al. (2013) through the in-situ microscopic flow of suspension under influence of shear. It was found that the viscosity suspension at low volume fractions behaves like a Newtonian fluid, while at higher volume fraction the suspension viscosity is described by Quemada model as in Equation (2.27). They also found that at the intermediate volume fraction, *C. vulgaris* exhibits the shear thinning behavior due to cell aggregation (Souliès et al., 2013).

2.6.3 DLVO theory of the algae suspension

The stability of the algae suspension depends on the interaction between the electrostatic Debye repulsion potential with the van der Waals attraction potential (Mazza, 2016; More et al., 2014; Ndikubwimana et al., 2015). This interaction is approximated using Derjaguin, Landau, Verwey, and Overbeek (DLVO) theory which states two charges particles separated by distance *s* interact with total interaction energy given by summation of repulsive electrostatic Debye repulsion potential energy U_c and attractive van der Waals attraction potential energy U_{vdW} as (Mazza, 2016):

$$\mathrm{U_{DLVO}(s)=U_{vdW}(s)+U_c(s)}. \tag{2.28}$$

2.7 Governing equation in microfluidics

Inside the microchannel with cross section area *A*, fluid flows with speed v_{avg} at flow rate of:

$$Q_{flow}=Av_{avg.} \tag{2.29}$$

The flow of fluid is characterized by the usage of the dimensionless hydrodynamic number such as Reynolds number and Mach number. Reynold number (*Re*) is defined as the ratio of the inertia forces to viscous forces:

$$Re=\frac{\rho u_{avg}L}{\eta}, \tag{2.30}$$

where the ρ is the fluid density, L is the hydrodynamic length and u_{avg} is the average fluid velocity. For low Reynold number $Re < 1$, the viscous forces will dominate the flow, producing laminar flow. While for high Reynold number $Re > 4000$ (Bruus, 2015), the flow becomes turbulent due to the fluid's inertia. In the case of very viscous flow with very small *Re*, the creeping flow or extreme laminar flow will develop. Additionally, Mach (*Ma*) number is defined as the ratio of fluid velocity U to the speed of sound in the fluid:

$$Ma=\frac{U}{c}, \tag{2.31}$$

which is used to measure the flow compressibility. When the flow is compressible, the density of the fluid changes during the flow.

When the fluid is pumped inside the microchannel, the continuity equation or conservation of mass equation of the fluid flow holds and is given by (Bruus, 2015):

$$\frac{\partial\rho}{\partial t}+\nabla.(\rho\mathbf{u})=0. \tag{2.32}$$

In incompressible flow, the fluid flow across the channel will maintain their volume and density over time. Hence the velocity **u** reduces to:

$$\nabla.(\rho\mathbf{u}) = 0. \tag{2.33}$$

The momentum of the fluid flow is expressed by Navier-Stokes equation:

$$\left(\frac{\partial\mathbf{u}}{\partial t}+\mathbf{u}.\nabla\mathbf{u}\right) = -\nabla p+ \nabla.(\mu\nabla\mathbf{u}+(\nabla\mathbf{u})^{T})-\frac{2}{3}\mu(\nabla.\mathbf{u})\mathbf{I}+\mathbf{F}. \tag{2.34}$$

The left-hand side term of Equation (2.34) represents the mass and acceleration of the fluid when it moves along the flow in form of inertial forces. While at the right-hand side of this equation represents all the possible forces that act on the fluid such as pressure forces, viscous forces, and external forces. Under incompressible laminar flow, Equation (2.34) reduces to more simplified version:

$$0 = -\nabla p+\nabla.(\mu(\nabla\mathbf{u})+(\nabla\mathbf{u})^{T}. \tag{2.35}$$

Solving Equation (2.35) required the imposition of the boundaries conditions. The common boundary condition used is the imposition of the zero-flow velocity at stationary boundaries known as non-slip boundary conditions which give solution of the Poiseuille velocity flow profile (Bruus, 2015).

The behavior of the fluid can be classified into (a) Newtonian fluid, and (b) Non-Newtonian fluid. These fluid behaviors can be explained in term of the rheology properties of fluid i.e. how fluid react on the applied force or changes in fluid characteristics due to the applied forces. In a Newtonian fluid, the viscosity coefficient is constant thus fluid responses on the applied forces is predictable. For example, the Newtonian fluid has constant viscosity when applied forces act on it i.e. the viscosity remains constant as the velocity gradient changes. On the other hand, for the non-Newtonian fluid the viscosity coefficient is not constant as it produced unexpected response on the applied forces. For instance, the viscosity of non-Newtonian fluid decreased with increasing velocity gradient as observed in high volume fraction of the *C.vulgaris* suspension (Souliès et al., 2013). On the contrary, the flow of red blood cell shows the increase of viscosity as velocity gradient increased as a result of shear thickening effect (Schmid-schonbein et al., 1969).

The flow of fluid across the channel is analogous to the Ohm's law in electrical circuit design (Bruus, 2015; Stone, 2007). The volumetric flow rate Q is analogous to the current density, the pressure drops across channel length L acts as the potential drop in circuit and hydrodynamic resistance R_H acts to dissipate the fluid's energy similarly as electrical circuit's resistance. The Ohm's Law version of the fluid circuit is called Darcy's Law. The hydrodynamic resistance R_H in the circular shape channel can be approximated as:

$$R_H = \frac{\Delta p}{Q}, \tag{2.36}$$

which relates the pressure drop to the volumetric flow rate in other similar form:

$$R_H = \frac{c\mu L}{a^4}, \tag{2.37}$$

where $c = \frac{8}{\pi}$ (Stone, 2007). This dependence of R_H on the fourth power of radius means 10 % change in radius produces approximately a 40 % change in flow for a given pressure drop. In rectangular shape channels of width w and height h, with $h < w$, R_H can be approximated as:

$$R_H = \frac{c_r \mu L}{h^3 w}, \tag{2.38}$$

where $c_r = 12$.In laminar pipe flows, the average flow velocity is given by:

$$u_{avg} = \frac{a^2 \Delta p}{\mu L}. \tag{2.39}$$

Then the volumetric flow rate can be approximated by:

$$Q \approx u_{avg} a^2 \approx \frac{a^4 \Delta p}{\mu L}. \tag{2.40}$$

Clearly, the volumetric flow rate has fourth power dependence on the radius of the channel. In rectangular shape, a microfluidic channel with $h \ll w$ under the steady pressure-driven laminar flow, the velocity profile developed in the channel is parabolic (Stone, 2007) :

$$u(y) = \frac{\Delta p}{2\mu L}\left[\left(\frac{h}{2}\right)^2 - y^2\right]. \tag{2.41}$$

The volumetric flow rate of fluid across the channel with width w can be approximated as:

$$Q = w \int_{0}^{h} u\,(y)dy = \frac{wh^3 \Delta p}{12\mu L}, \tag{2.42}$$

with an average velocity v_{avg} of:

$$u_{avg} = \frac{h^2 \Delta p}{2\mu L}. \tag{2.43}$$

CHAPTER 3: METHODOLOGY

In this chapter, the basic properties and characteristics of the *C. vulgaris* and its growth media are described. The techniques used to study the particle dynamics in open and closed domains will be given followed by descriptions of the key transport properties to be estimated from the experimental and numerical simulation.

3.1 Cell characterization

A series of experiments and measurements are conducted to study the basic properties and characteristics of the particle and its growth medium. The Bold's basal medium (BBM) is prepared by diluting the minerals and salts with distilled water until it reached pH of 6.5. Then, the microalgae *C. vulgaris* culture is grown in the BBM and maintained under controlled-environment incubator at temperature of 28 °C as shown in Figure 3.1. The cool white fluorescent lamps (Philips, TLD 18W/ 54-765) is used to illuminate the culture by providing it 42 $\mu\text{molm}^{-2}\text{s}^{-2}$ PAR on a 12-hour light: 12-hour dark cycle. All the characterization and experimental measurements are then carried-out at a temperature of 25 ℃ unless it is mentioned otherwise.

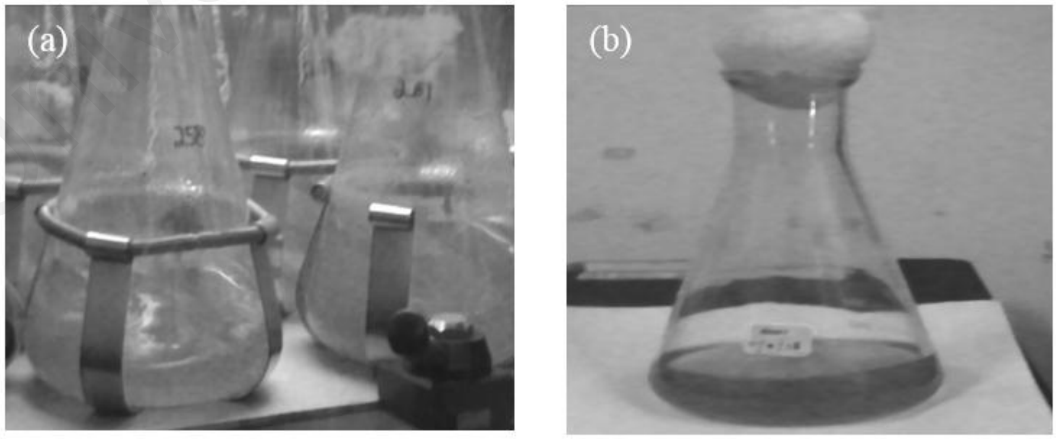

Figure 3.1: (a) Algae cultures grown in incubator, and (b) *C. vulgaris* culture with stain 001.

3.1.1 Cell count

Number of cell or algae will be counted using the hemocytometer. Hemocytometer is a type of microscopic slide with counting grids located at the middle of the slide. Since the average diameter of *C. vulgaris* is 10 µm, in this study the number of cells are counted using the center square counting region.

A hemocytometer is cleaned by wiping it with ethanol soaked tissue to remove dust contaminant. It is left exposed to dry any excess ethanol on its surface. The cell samples are prepared by diluting the 1 mL of original culture with 9 mL of BBM media. The cover slide is first placed in the middle of the hemocytometer before 10 mL of the cell sample is injected to both side of the haemocytometer by using a pipette. Then, the haemocytometer is fixed on the microscope stage where 40 times magnification is used to observed and to manually count the cell in the counting grid. It is important to ensure the suspension is suffeciently dilute to avoid cell overlapping and to achieve uniform distribution of cell in the grid. To avoid counting the cell twice, only the cells on the lines of the large squares are counted.

From the obtained cell count data, the cell density n_c is calculated from $n_c = (C_{pss} \times D_f) / V_{ss}$ where C_{pss} is average cell per small square, D_f is dilution factor, and V_{ss} is the volume of the small square (mL). Each hemocytometer has a specific value of $V_{ss} \sim 0.0001$ mL. The dilution factor is obtained from $D_f = (V_s + V_l) / V_s$ where V_l is the volume of diluting liquid and V_s is the volume of sample which gives the D_f of 1. Finally, total number of cell N_c is calculated using $N_c = n_c \times V$.

3.1.2 Chlorophyll content

Chlorophyll-a (Chl-a) concentration is measured via spectrophotometric method (Strickland & Parson, 1968). To start, a 20 mL of algal culture is collected on a glass-fiber filter paper (Whatman GF/C, 0.45 µm). The filter is folded and is mashed into tiny pieces by using tiny glass rod. The sample is soaked with 10 mL of analytical grade 100 % acetone as shown in Figure 3.2(a). The test tubes with sample are then covered with aluminum (Al) foil (Figure 3.2(b))) and stored in the refrigerator (4 ℃) with dark condition for storage time of 24 hours. Finally, the samples are centrifuged (3000 rpm, 10 minutes, 4 ℃) as depicted in Figure 3.2(c,d) and absorption of the supernatant is measured at 630 nm (OD_{630nm}), 645 nm (OD_{645nm}) and 665 nm(OD_{665nm}). The Chl-a concentration is calculated from Chl-a $= (C_a \times V_a)/V_c$ where Ca $=11.6\,OD_{665nm} - 1.31OD_{645nm} - 0.14\,OD_{630nm}$, V_a is volume of acetone used for extraction and V_c is volume of culture.

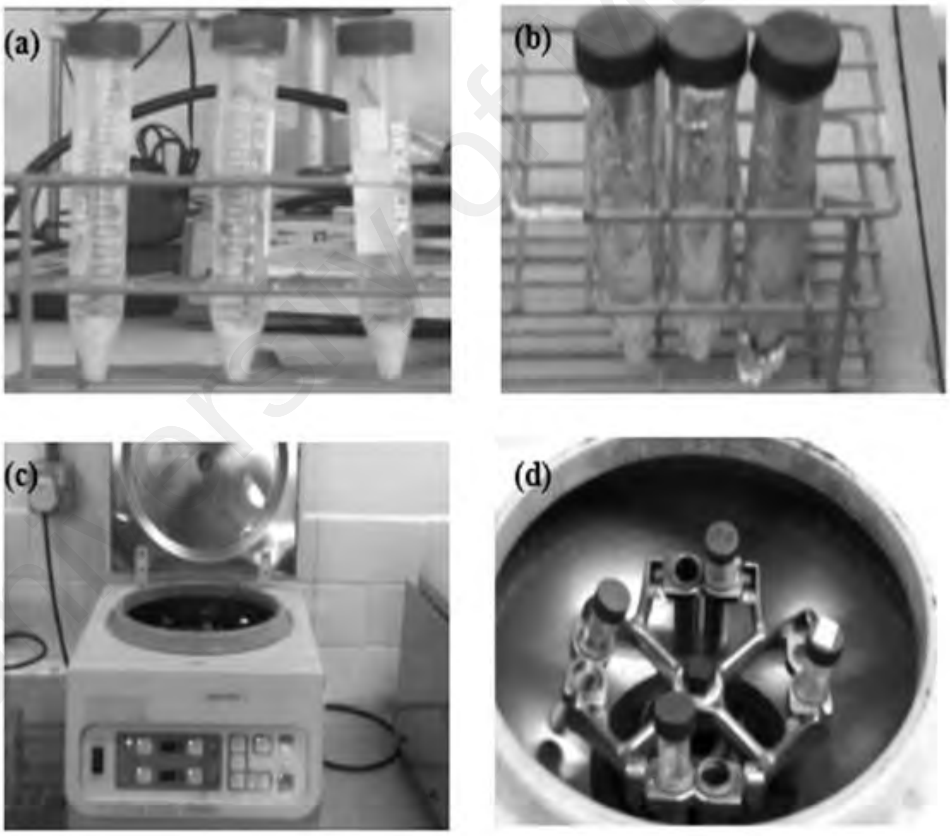

Figure 3.2: Step of the sample preparation for the Chlorophyll and Carotenoid measurements: (a) Algae culture collected by the glass-fiber filter paper and suspended into acetone, (b) freezing the sample, (c) and (d) centrifuged the cell.

3.1.3 Carotenoid content

Carotenoid content of microalgae is measured with the similar method applied for the measurement of Chl-a, but with different supernatant absorption wavelength at 452 nm (IO452 nm). The absorbance of the pigment is extracted by employing colorimetric method from Vonshak and Borowitzka (1991). Then, Carotenoid content is calculated as Ca $= OD_{645nm}\, 3.86 V_a / V_b C$ where OD_{645nm} is absorbance at 452 nm, V_a is volume of acetone used for extraction and V_b is volume of algal culture filtered (mL). Both supernatant absorption on Chl-a concentration and Ca content are measured using Shimadzu UV-vis spectrometer.

3.1.4 Viscosity measurement

The force **F** required for moving two parallel fluid layers with area *A* separated by distance $d\mathbf{x}$ with velocity $d\mathbf{v}$ is:

$$\mathbf{F} = \frac{d\mathbf{x}}{A d\mathbf{v}} \tag{3.1}$$

This force is defined in term of dynamic viscosity η by rewriting Equation (3.1) as:

$$\eta = \frac{\mathbf{F}}{A \frac{d\mathbf{v}}{d\mathbf{x}}} \tag{3.2}$$

By Stokes law definition, a sphere suspended in the fluid will experiences force with a magnitude given by the product of constant velocity ***v***, dynamic viscosity η, radius of the sphere *a* and some constant:

$$\mathbf{F}_{stokes} = 6\pi\eta a\mathbf{v} \tag{3.3}$$

For a sphere falling under the influence of gravitational field, the force acting on the particle is equal to the product of the effective mass *m*' and gravity constant *g*. In this case, the effective mass can be expressed in term of the difference in density of the particle ρ_1 and fluid density ρ_2 as:

$$\mathbf{F}_g = m'g = \frac{4}{3}\pi g(\rho_1 - \rho_2) \tag{3.4}$$

In the limit law of expanded media, the term of particle's radius with respect to the radius of gravity tube can be neglected. Thus, the relationship of the dynamic viscosity is established by solving and approximating Equation (3.3) and Equation (3.4) by corrections (Ladenberg Correction) such that (Hensley & Papavassiliou, 2014):

$$\eta = \frac{2a^2(\rho_1 - \rho_2)}{v}. \tag{3.5}$$

In the case of commercial falling ball viscometer with calibrated sphere, the constant in Equation (3.5) takes a form of spherical constant *K*. Then the dynamic viscosity is approximated as:

$$\eta = Kt\,(\rho_1 - \rho_2) \tag{3.6}$$

where t is the time taken for the sphere to fall for a measured distance s = 100 mm. Then, the density of the fluid ρ_2 at temperature T can be measured using pycnometer via relationship of:

$$\rho_2 = \frac{m}{V} \tag{3.7}$$

where m is the fluid/liquid's mass and V is the pycnometer volume.

Viscosity of the BBM is measured by conducting falling ball viscometer (Figure 3.3) at room temperature 25 °C with five repetitions. The ball/sphere used is made up from borosilicate glass. The viscometer is connected to the pump connection unit of the thermostat where the bath is filled with water until it covered fraction three quarters above the sensor. The gravity tube is filled up with BBM solution and a ball is placed inside it. The viscometer is allowed to achieve a room temperature before determining falling times (5 repetitions). Then, arithmetic mean is taken. Finally, the viscosity of the BBM is obtained by inserting value of arithmetic mean of the ball into Equation (3.6) with spherical constant K = 0.00893.

Figure 3.3: Falling ball viscometer setup. At the left-hand side is the unit pump connected to the thermostat and at the right-hand sight is gravitational tube filled with BBM.

The density of BBM is measured using pycnometer and is calculated using relationship $\rho_2 = m/V$, where m is mass of the liquid, and V is the volume of pycnometer. First the mass of dry and clean pycnometer is measured, and then the BBM is filled in and allowed to equilibrate in thermostatic water bath for 15 minutes before the measurement is taken again. Then, the mass of the liquid is simply the absolute difference of the mass of empty and dried pycnometer and mass of filled pycnometer.

3.1.5 Size distribution

A set of images of microalgae comprising of 29734 cells are obtained by using video camera mounted on an optical microscope with 10 times magnification. This set of images are pre-processed and analyzed by image processing software Image J (Schneider et al., 2012). Due to uneven illumination on some portion of the images, the area of analysis is restricted only to the area of images that has even illumination. Evenly illuminated images are necessary to reduce the complication in thresholding the images (See Appendix A for details procedures).

3.1.6 Zeta potential measurement

The stability of the colloidal system i.e. whether the cells will aggregate or disaggregate depend on the magnitude of Zeta potential (Cieśla et al.,2011). Zeta potential is the measure of surface charges of the cell where high potential corresponding to strong electrical repulsion between the algal cells can lead to highly stable suspension. Meanwhile, lower Zeta potential means the particles will attract each other due to the van der Waals forces and flocculate (Vandamme et al., 2013). Zeta potential of cells is measured via a zeta analyzer (Malvern Instruments Ltd) with water as a dispersant and fresh algae medium solution, BBM at pH 6 is used as the background fluid.

3.2 Open domain tracking

In this section, we describe how the motion of the *C. vulgaris* cells are tracked without applied flow rate and in the open domain. Due to the large size of the *C. vulgaris*, one may classify it as a non-Brownian suspension (Souliès et al., 2013). It is interesting to study the transport of the *C. vulgaris* in the absence of applied pressure and confinement to obtain initial insight on the dynamic of the freely moving particles.

A drop of *C. vulgaris* suspension is suspended between the glass slides. The glass slides are then placed onto the microscope stage where the observation is made using 10 times objective lens. The motion of the algae is recorded via the video camera mounted on the microscope stage with a frame rate of 15 fps for the duration of one minute as shown in Figure 3.4. The video is saved in .avi format.

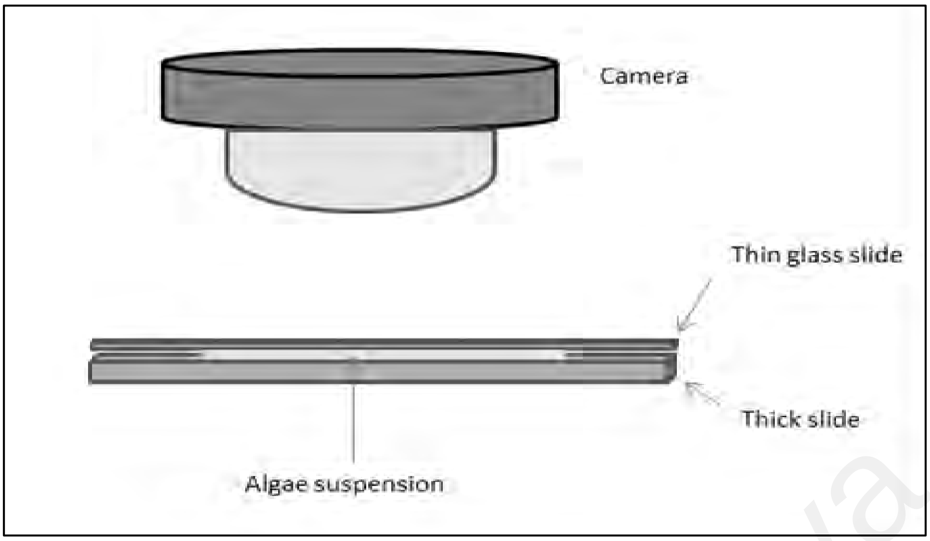

Figure 3.4: Simplified illustration of simple particle tracking experiment. The sample is covered with cover slide and the observation of the cell dynamics is recorded by video camera mounted on the top of microscope.

3.3 Flow experiments in microfluidics

3.3.1 Microfluidic set-up

The experiment set-up is shown in Figure 3.5 which consists of a pressure controller, a reservoir, a flow sensor, a Y-junction microfluidic chip, a high-speed CCD camera and a zoom lens. The pressure-driven system is applied to drive fluid into the microchannel to achieve stable and pulseless flow. First, the input pressure generated from the air compressor is stabilized and regulated by pressure controller. Then, the coupling between the pressure controller with the flow sensor produces the feedback loop, which is finally used to control the flow rate of the fluid entering the inlet. All the feedback from the variation of the pressure and flow rate is monitored on a computer with aids of ESI Microfluidic Software (ElveFlow). To avoid contamination within algae suspension algae due to its respirational waste product, the tracking of the particle is done in the periods of 24 hours.

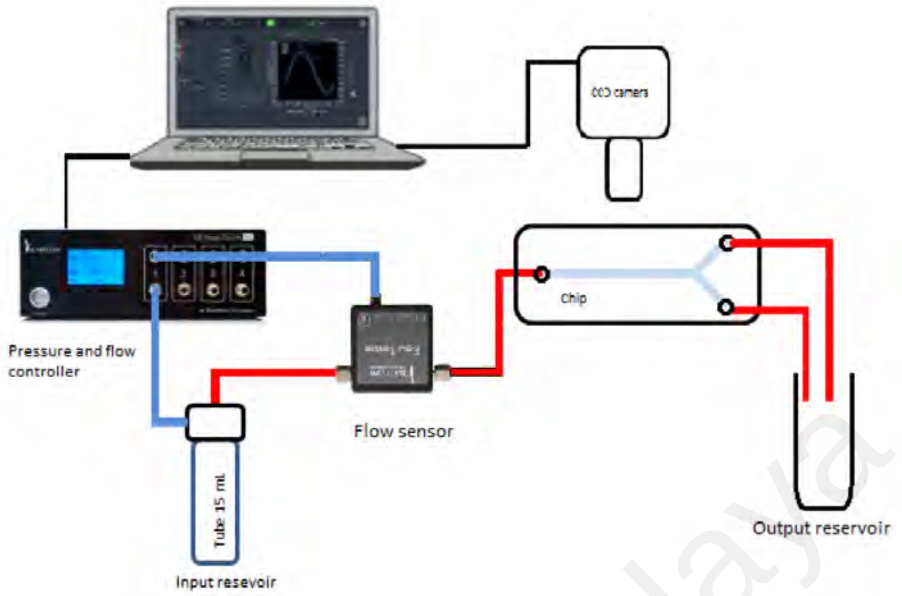

Figure 3.5: Schematic setup of the microfluidic flow experiment.

3.3.2 Observation setup

The particle tracking is carried out using bright field microscopy technique. The light source is reflected by the mirror placed underneath of the microfluidic stage as shown in Figure 3.6. Transmitted light is collected by the objective and coupled to the CCD camera. Thus, the specimen image appeared dark against the light background.

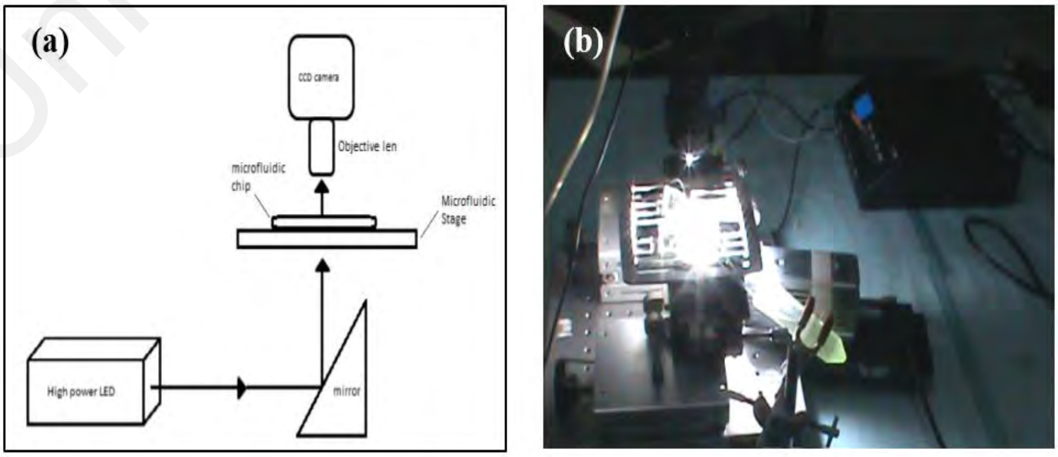

Figure 3.6: Observation set up.

3.3.3 Experiments

First, the channel is initially filled with deionized water, and then the BBM solution at a high flow rate of 3000 μL/min to wash away the dirt and unwanted suspensions. Then, particle suspension dispersed in BBM is pressurized inside the reservoir before it is released into the microfluidic chip by controlling the pressure between inlet and outlets via pressure controller (OB1 Elvesflow) to initiate the intended flow rates. In these experiments, the choices of flow rates are 0.2 μL/min and 0.3 μL/min due to the stabilities of flow produced. The flow is then allowed to stabilize for 10 minutes. The motion of the particles is captured at a distance of L = 2.1 cm away from the entrance of the channel using a Mikrotron CCD camera. Images are captured at frame rates of 2000 to 3000 fps depending on the applied flow rates assisted by illumination by a high-power LED light source. The light is focused using the mirror located under the microfluidic stage. In order to capture the motion of fast particles with high frame rate, one need bright light source; otherwise the quality of the images will be impaired due to less photon hitting the sensor. On the other hand, the smaller frame rate may miss out details of particles motion. Hence, an optimal frame rate is chosen by compensating the speed of the flow and light illumination available in the laboratory, which is in the range of 2000~3000 fps.

3.3.3.1 Particle tracking

In this pressure-driven microflow, we assumed the uniform Poiseuille flow profile is fully developed inside the microchannel. Then, the velocity of the flow is minimal near the wall region and maximum flow velocity occurs near the center of the channel as illustrated in Figure 3.7. The particle flow in this system will inherit the velocity from the flow profile, and thus the particle is transported at the different rates according to the flow regions.

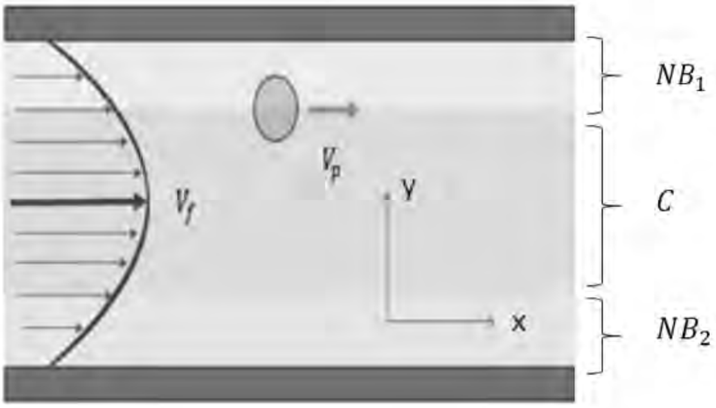

Figure 3.7: Schematic of studied problems. The lighter shaded areas refer to near wall boundaries *NB₁* and *NB₂* respectively. The darker shaded region represents the center region *C*.

Therefore, the particles trajectories are grouped with respect to the region of flow profile, namely near wall boundary NB_1, near wall boundary NB_2 and center *C*. In order to roughly estimate the flow regions, the expected equilibrium position for the particle's migration termed as Segré-Silberberg radius (Chen, 2014; Gupta et al., 2009; Loisel, et al.,2015), which is 60 % from the center plane as is used as the reference. For the symmetrical rectangular channel of 250 μm × 200 μm (width × height), the equilibrium position r_{eq} is 75 μm with respect to the hydraulic radius of the channel *R*. Based on the r_{eq}, the estimate length of near wall boundaries regions are given as $50\ \mu m < r_{eq_{b1}} <$ 0 μm and $175\ \mu m < r_{eq_{b2}} < 250\ \mu m$ respectively, whilst the center of channel region as 50 μm $< r_c <$ 175 μm. Here *x*-direction corresponds to the longitudinal (streamwise) direction and *y* is the transverse (perpendicular) direction to *x*.

Trajectories of individual particles are found using FIJI plugin algorithm (Schindelin et al., 2012; Tinevez et al., 2017) that link a particle in one field to the most probable closest particle in the next field with distance travelled less than inter particles spacing. The relevant particles trajectories are chosen based on imposed criteria on the mean velocity, duration of the track, displacement and number of spots to avoid tracking "fake" particles. In addition, due to the presence of the upper wall in *z*-direction, some of the particles might get stuck and become immobile. These immobile particles are excluded from the final analysis.

3.3.3.2 Time averaged mean square displacement

In order to obtain large samples of particles and improve the accuracy of tracked particles, the stack video images are resampled into five smaller sample stacks. The first 1000 frames are ignored during the analysis. A quarter of overall data points are used to calculate the MSD. The algorithm for the MSD calculation is written in MATLAB (Appendix C) and the flow algorithm is listed in the flow chart as depicted in Figure 3.8.

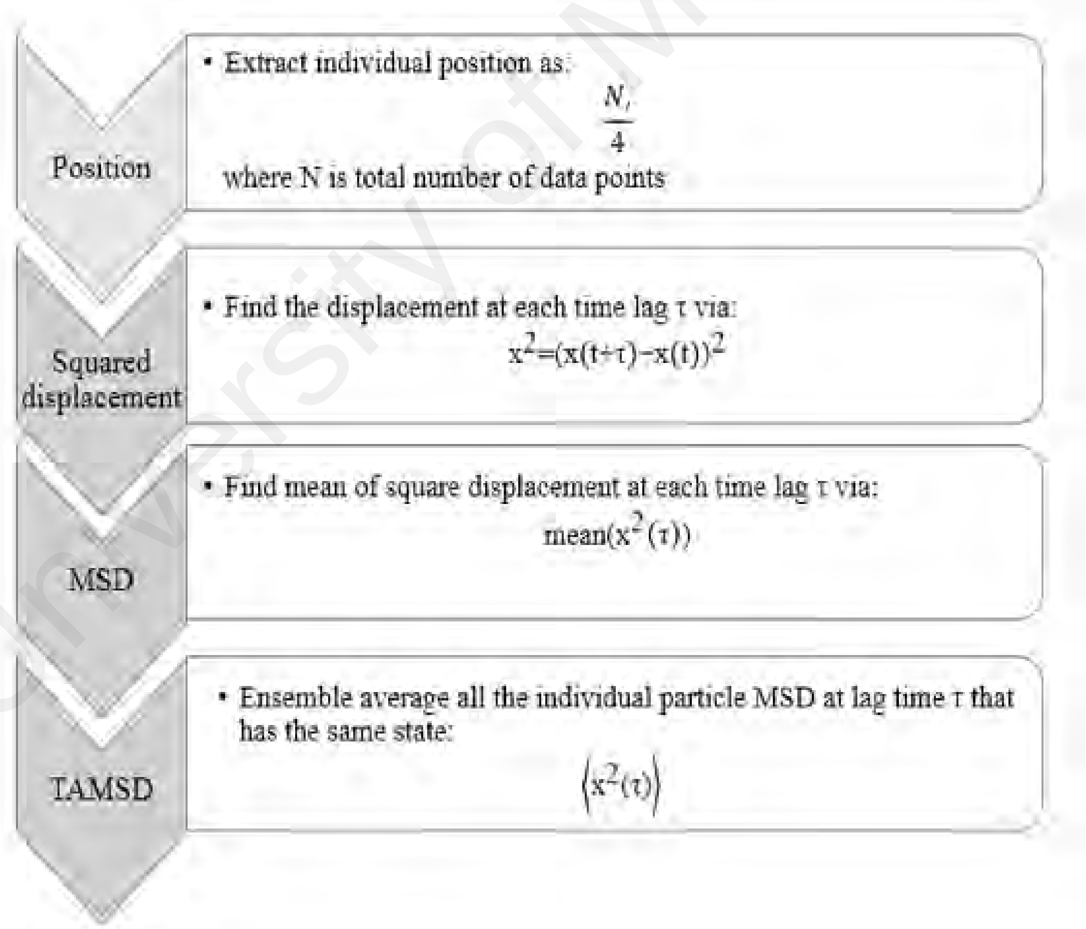

Figure 3.8: Flow chart of the MSD calculation algorithm.

The time averaged MSD (TAMSD) at lag time τ over a trajectory ***r(t)*** of length *M* is used to characterise the particle dynamics:

$$\langle\overline{\delta^2(\tau)}\rangle = \frac{1}{t-\tau}\int_0^{M-\tau}[r(t+\tau)-r(t)]^2 dt. \tag{3.9}$$

Particles trajectories data points are trimmed to a minimum of 100 points for 0.2 μL/min, and 50 points for 0.3 μL/min. The minimum number of the data points extracted are chosen to avoid the inclusion of the "fake" particles (see Section 3.3.3.1) in the analysis. Then, the TAMSD of the individual particle at time *t* is obtained by averaging MSD at each lag time τ. Thus, the scaling exponent can be extracted by applying the linear least squares regression on the bi-logarithmic TAMSD curve. The slope of the curve represents the scaling exponent.

3.3.3.3 Velocity autocorrelation function

The average velocity ***V*** for individual particle at particular lag time τ is defined as:

$$\boldsymbol{V}(\tau) = \frac{\boldsymbol{r}(t+\tau) - \boldsymbol{r}(t)}{\tau}. \tag{3.10}$$

The velocity autocorrelation function (VACF) is obtained in a similar manner as TAMSD by taking ensemble average of the individual particles velocity tracks such as:

$$C_v(\tau) = \frac{1}{t-\tau}\int_0^{M-\tau}[\boldsymbol{V}(t+\tau) - \boldsymbol{V}(t)]dt = \langle \boldsymbol{V}(t+\tau).\boldsymbol{V}(t)\rangle. \tag{3.11}$$

3.3.3.4 Image processing

Raw images obtained from the microfluidic experiment are hardly visible as shown in Figure 3.9(a). Therefore, using image processing technique, the better contrast of particles from the background is achieved (Figure 3.9(c)). The images pre-processing is carried-out using FIJI image-processing software. Steps of pre-processing consist of background subtraction, image enhancement and pseudo-fluoresce transformation as shown in Figure 3.9(d).

Dirt on the camera lens is common types of artifact in a digital imaging system as spotted in the image shown in Figure 3.9(a). To remove this artifact, the second image from the stack images is chosen as the “flat-field” reference. The correction is done by applying division arithmetic operation on the images i.e. img1 = img1/img2 producing an image as shown in Figure 3.9(b). The white spots are the artifacts left from the particles, which appeared in the second images, whereas the black spots are the particles of interest. Next, the enhancement of particles spots is achieved using a non-linear filter such as a minimum filter to dilate the spots and also to remove the artifacts left from previous image corrections. These spots are enhanced by dilating the spots to the size of two pixels.

After this, the image’s brightness and contrast are adjusted to create dark objects against the bright background (Figure 3.9(c)). Then, the logical XOR operation is applied onto the image to transform transmitted light contrast images into pseudo-fluorescence images, enabling them to be suitable for processing by tracking tools design for fluorescence microscopy as shown in Figure 3.9(d). Finally, the particles are tracked based on their threshold minimum radius, maximum linking distance and the maximum gap between images (Figure 3.9(e)). Maximum linking distance is chosen by measuring the average minimum distance of the particles between the frames, which is 15 µm.

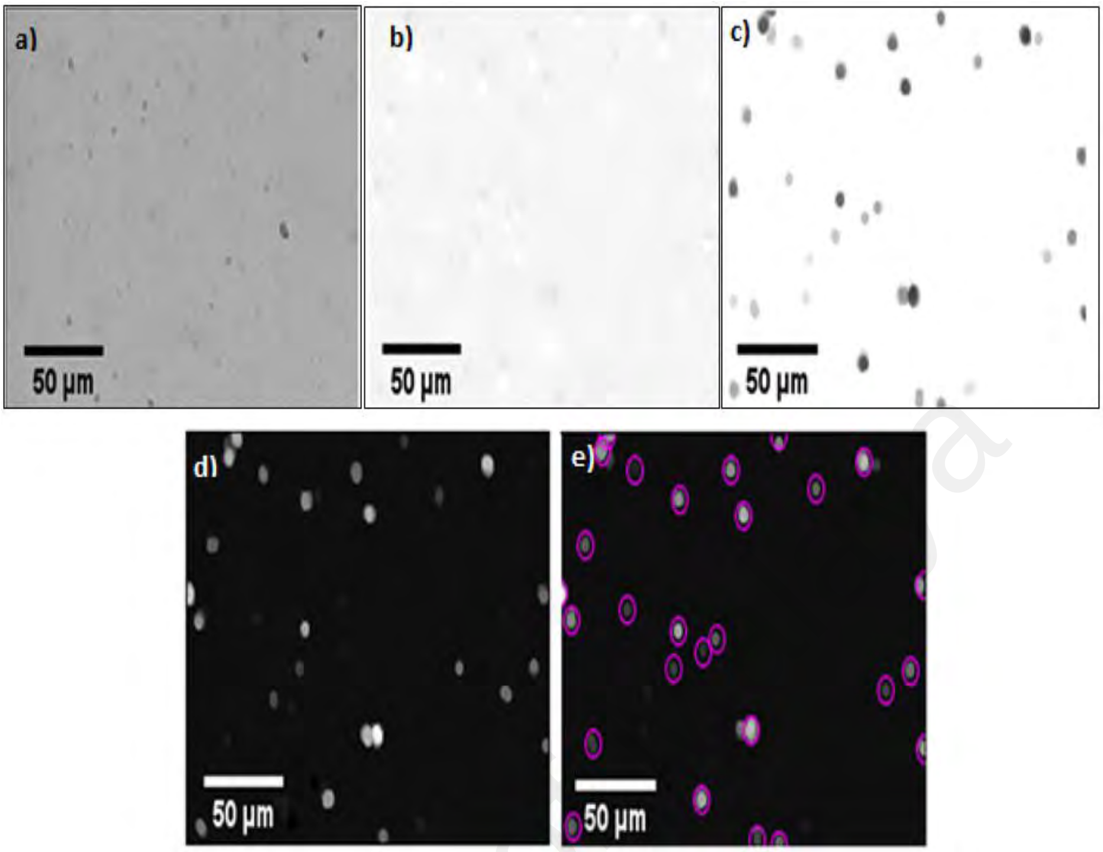

Figure 3.9: Visualization of images preprocessing: (a) Raw input image, (b) far field correction, (c) image enhancement, (d) pseudo-fluorescence image, (e)Particle's detection.

3.3.4 Computational fluid dynamics

In this section, the usage of computational fluid dynamics CFD via COMSOL Multiphysics 4.4a (COMSOL Inc., Palo Alto, USA) software is described which is based on the finite element (FEM) method. Two modules are used in the simulations including laminar flow, and particle tracing for the fluid flow. The one-way coupling approach is used where the continuous phase of the stationary velocity field of fluid is firstly solved using the stationary study before the trajectories of dispersed particle in the time-dependent study is computed.

3.3.4.1 Flow fields simulation

Boundary condition on the wall is applied when the particle interacts with the wall as a bounce wall condition. The particles reflect from the wall such that the momentum of the particle is conserved. The motion of the incompressible fluid flow in the narrow channel under laminar flow with Re < 1, characterized by Naiver-Stokes equation (Stone, 2007):

$$\left(\frac{\partial \mathbf{u}}{\partial t}+\mathbf{u}.\nabla\mathbf{u}\right)=-\nabla p+\nabla.(\mu\nabla\mathbf{u}+(\nabla\mathbf{u})^{T})-\frac{2}{3}\mu(\nabla.\mathbf{u})\mathbf{I}+\mathbf{F}, \tag{3.12}$$

and continuity equation:

$$\frac{\partial \rho}{\partial t}+\nabla.(\rho\mathbf{u})=0, \tag{3.13}$$

which reduces to the more simplified equations:

$$\begin{gathered} 0=-\nabla \mathrm{p}+\nabla.\left(\mu(\nabla\mathbf{u}+(\nabla\mathbf{u})^{T})\right), \\ \nabla.\mathbf{u}=0. \end{gathered} \tag{3.14}$$

The computational domain consists of the main entrance region with a channel width of 250 μm and length of 4.2 cm, and Y-junction region with each of junction of length of 1.2 cm. We divide the region of computational domain into two regions namely: (a) entrance region, and (b) Y-junction region. Noted that in this study our interest is the flow of the particles in long and narrow channel, thus the Y-junction region can be completely neglected. However, to ensure we properly capture the dynamics of the flow in real life experiment we carried out the flow simulation in both regions to evaluate the uniformity of the flow and velocity field across the microfluidic channel. Some of the assumptions made to simulate the flow are:

(i) the fluid is a Newtonian fluid,

(ii) the non-slip boundary conditions are applied at the wall of the channel, and

(iii) the flow is incompressible flow with low Mach number.

In the experiment, our observation region is taken as far away from the both inlet and outlets which is located at the middle long channel of Y-junction geometry (Figure 3.10(a)). Thus, the computational region is further reduced into single narrow channel geometry as depicted in Figure 3.10(b). This step reduces computational power and time.

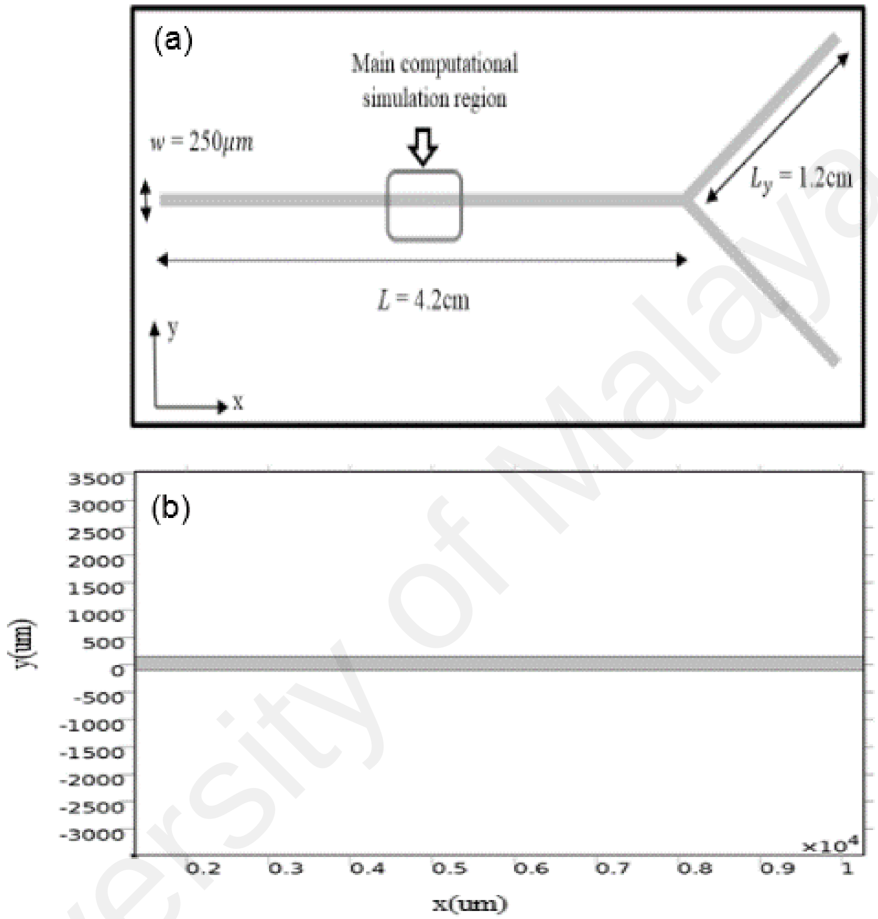

Figure 3.10: Computational simulation domain: (a) Y-junction and (b) single junction.

The two-dimensional computational domain of the microfluidic channel is build using the COMSOL geometry build in interface. The finer meshing was applied on the domain of element size of 10 μm to achieve high accuracy in both flow and particles trajectories results. The simulation of flow of BBM fluid inside the channel is performed by solving the steady state Navier-Stokes equation in Equation 3.14. The average velocity v_{avg} of the flow is approximated using the value of flow rate used in the laboratory experiment through the relationship of:

$$v_{avg}=\frac{Q}{A}, \tag{3.15}$$

where Q is applied flow rate in µL/min used in the experiment and A is area of the channel, $A = D_h L$. For the rectangular shape channel fully wetted with fluid, the hydraulic diameter D_h is given by $D_h = \frac{2hw}{h+w}$. Imputing the channel's parameters w = 250 µm , h = 200 µm and Q = 0.2 µL/min and 0.3 µL/min respectively into Equation (3.15) yields the v_{avg} of $8.33 \times 10^{-5}\mathrm{ms}^{-1}$ and $1.25 \times 10^{-4}\,\mathrm{ms}^{-1}$. These values are used as input flow velocity in the flow simulations.

3.3.4.2 Particles trajectories

The simulations on the dynamics population of the 25 particles are carried out by taking consideration of the properties of microalgae, *C. vulgaris* and the growth medium Basal Bolds Medium (BBM) measured in the previous section. The initial configuration of the particle is initialized such that the velocity field obtained from previous solving of Navier-Stokes equation is used to define the initial velocity of the particles. The forces exerted on a particle travelling in moving fluid are given by the classical Newtonian law (Silbert et al., 1997):

$$\sum_i \mathbf{F}_i=\frac{d}{dt}\left(m_p\mathbf{v}\right)= \mathbf{F}_{Stokes}+\mathbf{F}_{VdW}+\mathbf{F}_{EDL}+\mathbf{F}_{B}. \tag{3.16}$$

The force required to move an algal particle through the viscous fluid at specific velocity **u** is given by Stokes drag force,

$$\mathbf{F}_{Stokes}=\left(\frac{1}{\tau_p}\right) m_p(\mathbf{u}\text{-}\mathbf{v}). \tag{3.17}$$

The particles suspension viscosity is chosen to exhibit effective viscosity based on the Batchelor viscosity model (see Chapter 2; Section 2.5.2) with the volume fraction of 0.08

to take account of relatively high particle's volume fraction, yet the flow still remained as Newtonian flow. The constants appeared on forces equations are listed in Table 3.1. The particle will interact with other particles via attractive van der Walls force (Equation (3.18)) and repulsive Electric Debye layer (Equation (3.19)) force based on DLVO theory. As the two algae particles approach each other, the electrical repulsion increases due to the interaction of the electrical double layer between the algae, while the attractive van der Walls force increased as the distance **r** between algae becomes smaller. The van der Walls force is due to the generation of dipole moments from temporary asymmetry distribution of the electron cloud around the atom's nucleus. Electrical Debye layer force is the result of charge accumulation at the surface of the algae due to the ions present in the growth medium. The balance between these interaction leads to the stability of the algae suspension.

$$\mathbf{F}_{VdW} = -\frac{H_{ham}a_p}{12\mathbf{r}} \tag{3.18}$$

$$\mathbf{F}_{EDL} = 2\pi\kappa a_p \varepsilon {\psi_{part}}^2 \left(\frac{e^{-\kappa\mathbf{r}}}{1-e^{-2\kappa\,\mathbf{r}}} - \frac{e^{-2\kappa\,\mathbf{r}}}{1-e^{-2\kappa\,\mathbf{r}}}\right) \tag{3.19}$$

The implementation of Brownian force shown in Equation (3.20) depends on the time step for the software to solve the problem and it requires the generation of random numbers from a Gaussian distribution with zero mean and unit variance. The Brownian force is simulated with tolerance of 10^{-4}.

$$\mathbf{F}_{Brownian} = \xi\left(\frac{12\pi k_B \mu T a_p}{\Delta t}\right) \tag{3.20}$$

Equation (3.20) is solved for each particle by the time dependent solver and the time step is chosen by the software in this formulation. The time step chosen must be greater than particle momentum relaxation time, $\tau_r \approx {}^{m_p}/_{12\pi\mu a}$. The simulation performed in COMSOL for the whole computation without refining the domain required only single time step, thus we need to use very small step for the solution to converge to the real value. This constraint thus only allowed us to simulate limited number of particles as the computational time increased tremendously as time step gets smaller. The simulation is carried out until the system reaches a stationary state. All the results are obtained after the particles reaches the stationary state. The parameters and constants used in this simulation are listed in Table 3.1:

Table 3.1: Constants and parameters used in the simulations.

Parameter/constant	**Symbol**	**Values**
BBM density	ρ_f	1.00 *g/ml*
Microalgae density	ρ_p	1050 kg/m^3
Dynamic viscosity of BBS	μ_f	1.11 *mPas*
Inverse of Debye parameter	k^{-1}	$3.2 \times 10^8 m^{-1}$
Hamaker constant	H_{ham}	$1.51 \times 10^{-20} J$
Microalgae radius	a_p	$5 \mu m$
Boltzmann constant	k_B	$1.38065 \times 10^{-23} J K^{-1}$
Absolute temperature	T	298 °K
Microalgae zeta potential	ψ_{part}	-20.1mV

CHAPTER 4: RESULTS

Following the methodology described in Chapter 3, we present the results of the microalgae *C. vulgaris* cell characterization, microfluidic experiment and also the numerical simulation based on computational fluid dynamics modelling. First, the particles are characterized via particle count, size distribution, Zeta potential measurement, carotenoid, and chlorophyll content. The viscosity of the medium BBM is measured through the falling ball experiment. Particle tracking of the cell in both open space (without applied flow) and inside microfluidic channel (with applied flow) are presented. The numerical simulation of the particle in microchannel served as the test-platform, even though the particles here are treated in a rather simplistic way.

4.1 Cell characterization

From the cell counting, we estimated the cell density to be around 770,000 cells/mL which corresponds to 6,930,000 cells in the sample volume of 9 mL. The cells are of roughly spherical in shape (Figure 4.1(a)) with a mean radius of r = 3.91 µm and a standard deviation of r_{std}= 0.491 µm. Cell size distribution (radii) can be modelled by a log-normal distribution (the full line in Figure 4.1(b)) as reported in (Pottier 2005) for *Chlormadinones Reinhardtian* species, which was found almost similar in shape. We stressed that the rather large cell size makes *C. vulgaris* suspensions to fall into the class of non-Brownian suspensions.

The chlorophyll and carotenoid content of the *C. vulgaris* algae are tabulated in Table 4.1 which is in agreeable value for the green algae species (Schagerl & Künzl, 2007). The cells suspension has negative surface charge of -20.1 mV as indicated by the maximum peak of the distribution (Figure. 4.2(b)). The measurement of Zeta potential value shows the reliable results with small standard deviation from the mean value as tabulated in Table 4.2.

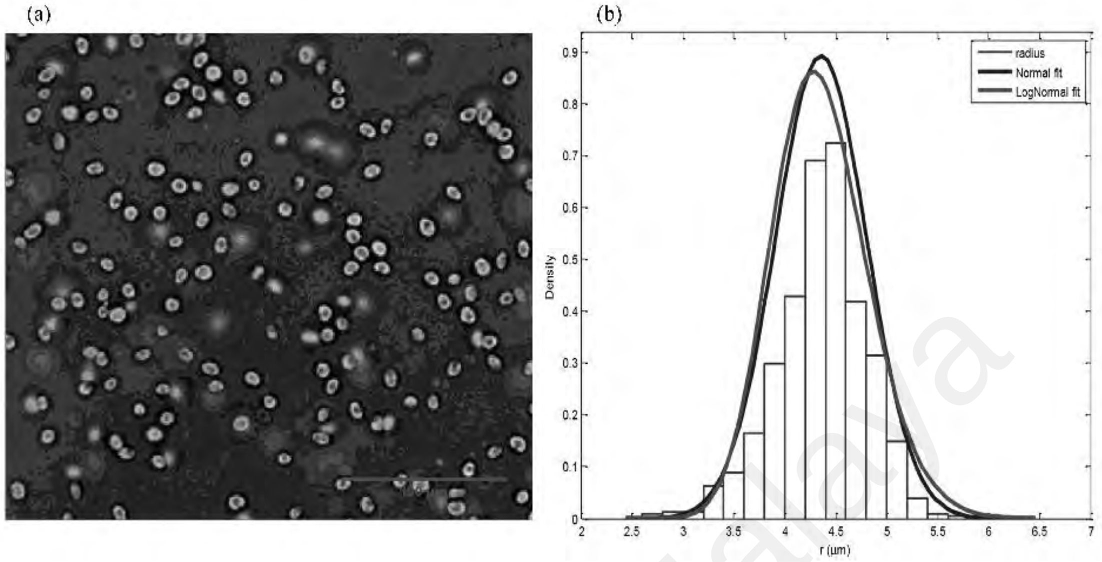

Figure 4.1: (a) Pseudo-fluorescence images of the *C. vulgaris* (b) Probability distribution function PDF of *C. vulgaris* radius.

Table 4.1: Result of algae chlorophyll and carotenoid measurement.

Parameter	**Value (±0.0001 mg/L)**
Chlorophyll content (*Chl-a*)	0.0013
Carotenoid content (*Ca*)	0.2850

Table 4.2 : Result of algae zeta potential measurement.

		Mean(mV)	**Area (%)**	**Standard Deviation (mV)**
Zeta Potential(mV)	-20.1	Peak 1: -20.1	100.0	5.79
Zeta Deviation(mV)	5.79	Peak 2: 0.00	0.0	0.00

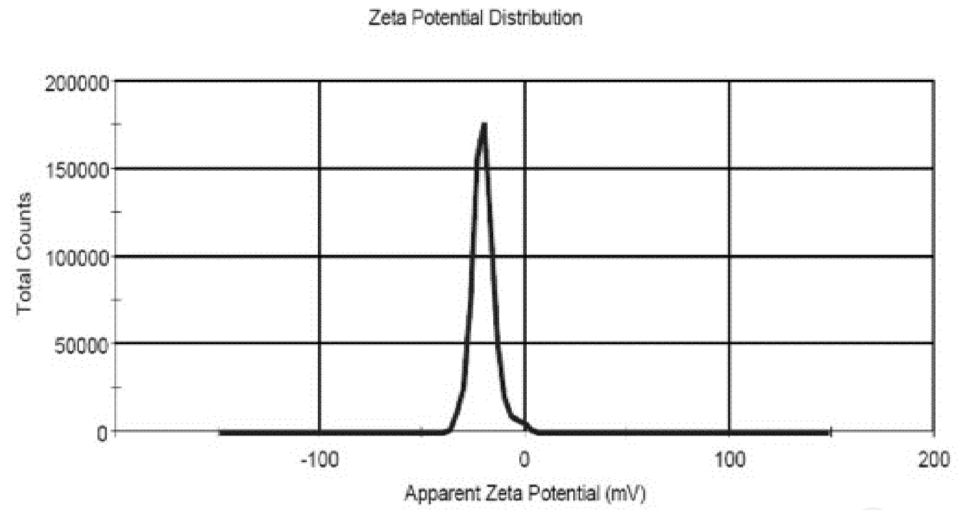

Figure 4.2: Zeta potential of algae result.

The estimate value of the BBM viscosity as shown in Table 4.4 is compared to that reported in existing literature (Santos -Medrano et al., 2001) of η= 1.18, and is to be in agreement within the uncertainty value.

Table 4.3: Results of the falling ball experiments.

Mass of empty Pycnometer (m_0 ± 0.01) g	**Mass of BBM filled pycnometer (m_1 ± 0.01) g**	**Mass of BBM ($m_{BBM} = m_1 - m_0$)**	**Average time taken, *t* (s)**
25.45	50.78	25.33	9.294
25.46	50.76	25.30	9.430
25.47	50.77	25.30	9.232
25.49	50.76	25.27	9.266
25.47	50.75	25.28	9.340

Table 4.4: Characterization parameters results.

Parameters	**Values**
Average mass of BBM m_{bbm}	25.30 ± 0.02 g
Volume pycnometer V	25.43 ml
Density of BBM ρ_{BBM}	1.10 ± 0.02 g/mL
Spherical constant K	0.09772

Table 4.4, continued.

Parameters	Values
Mass of sphere	4.414 m
Density of sphere	2.218 g/cm^3
Viscosity η	1.11 ± 0.07mPa/s

4.2 Particle tracking in open space

The trajectories of particles are extracted using the image pre-processing and particle tracking method that was described in Chapter 3. The trajectories are shown in Figure 4.3.

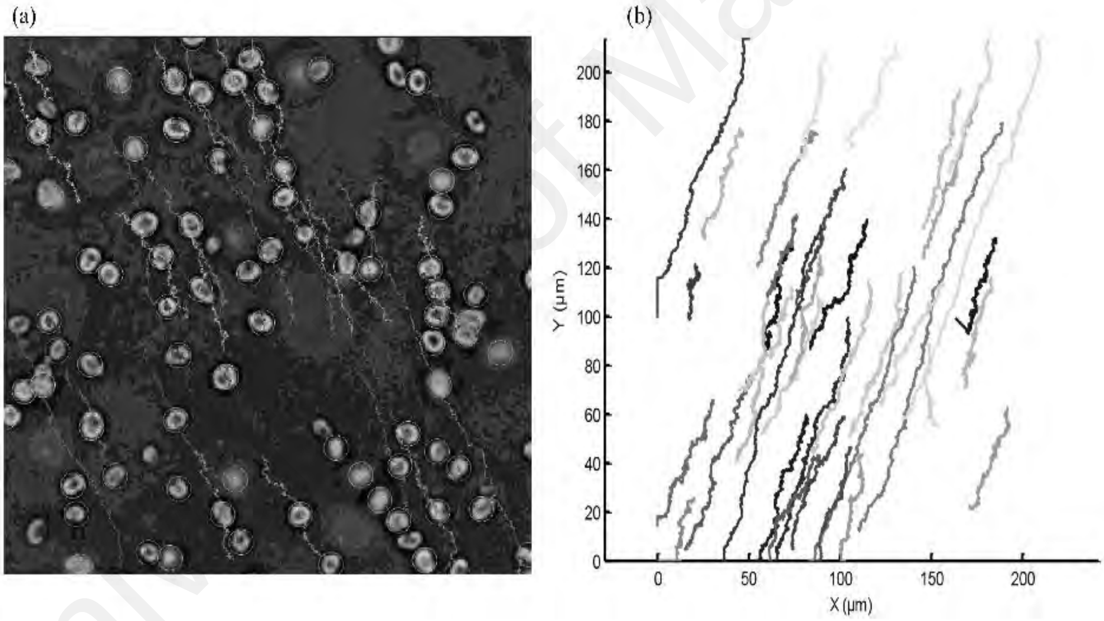

Figure 4.3: (a) Binary trajectories of microalgae in image, (b) re-plotted trajectories of microalgae.

As shown in above Figure 4.3, the algae have directional motion due to directional drift from the motion of glass slide. This trend is removed through the de-trend analysis before each individual particle spatial trajectories are standardized as shown in Figure 4.4.

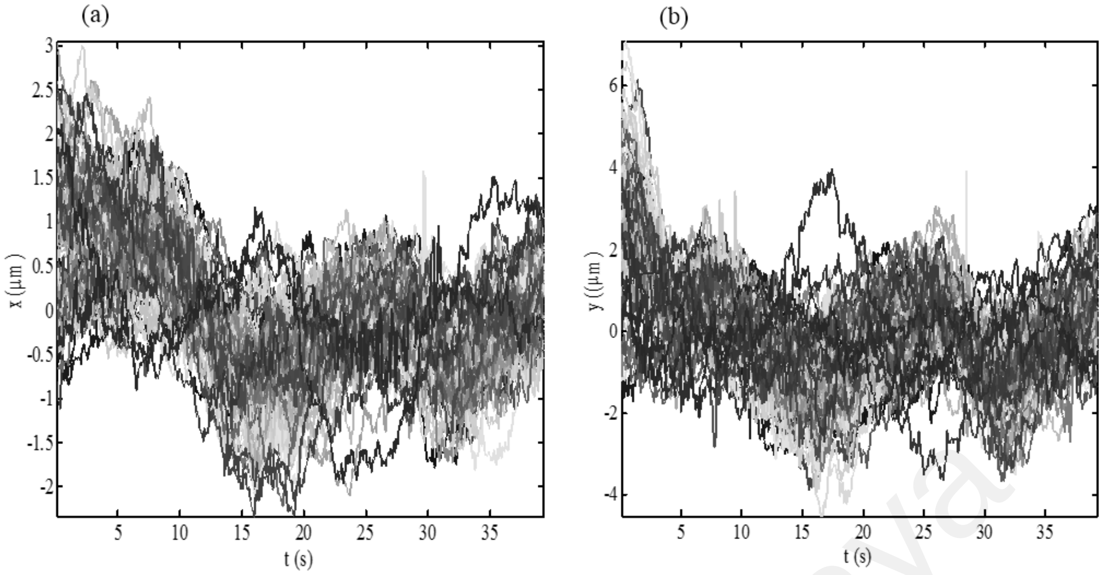

Figure 4.4: Standardized spatial particles positions in: (a) *x*-direction and (b) *y*-direction.

By using the detrended positions of the sample of 92 particles, the individual TAMSD of the particle in *x*, *y*, and resultant direction are calculated as shown in Figure 4.5. The grey lines represent the individual TAMSD, while the black thick line represents the averaged TAMSD.

The averaged TAMSD at the *x*, *y*, and resultant directions are plotted in Figure 4.6. The slope from the linear regression on the log-log plot reveals the *C. vulgaris* exhibit mixture of transport behavior in all directions and is summarized in Table. 4.5. In spatial *x*-direction, the particles showed MSD ~ $t^{0.99}$ (Brownian motion) and MSD ~ $t^{0.94}$ (weak sub-diffusion) at short and long-time scales, respectively. The same transition scale is also observed in case of spatial *y*-direction where the MSD~ $t^{0.93}$ at short time scale (weak sub-diffusive) and MSD ~ $t^{1.15}$ (super-diffusive) at longer time. However, the resultant MSD shows the mono-scaling behavior with MSD~$t^{0.98}$ (Brownian motion).

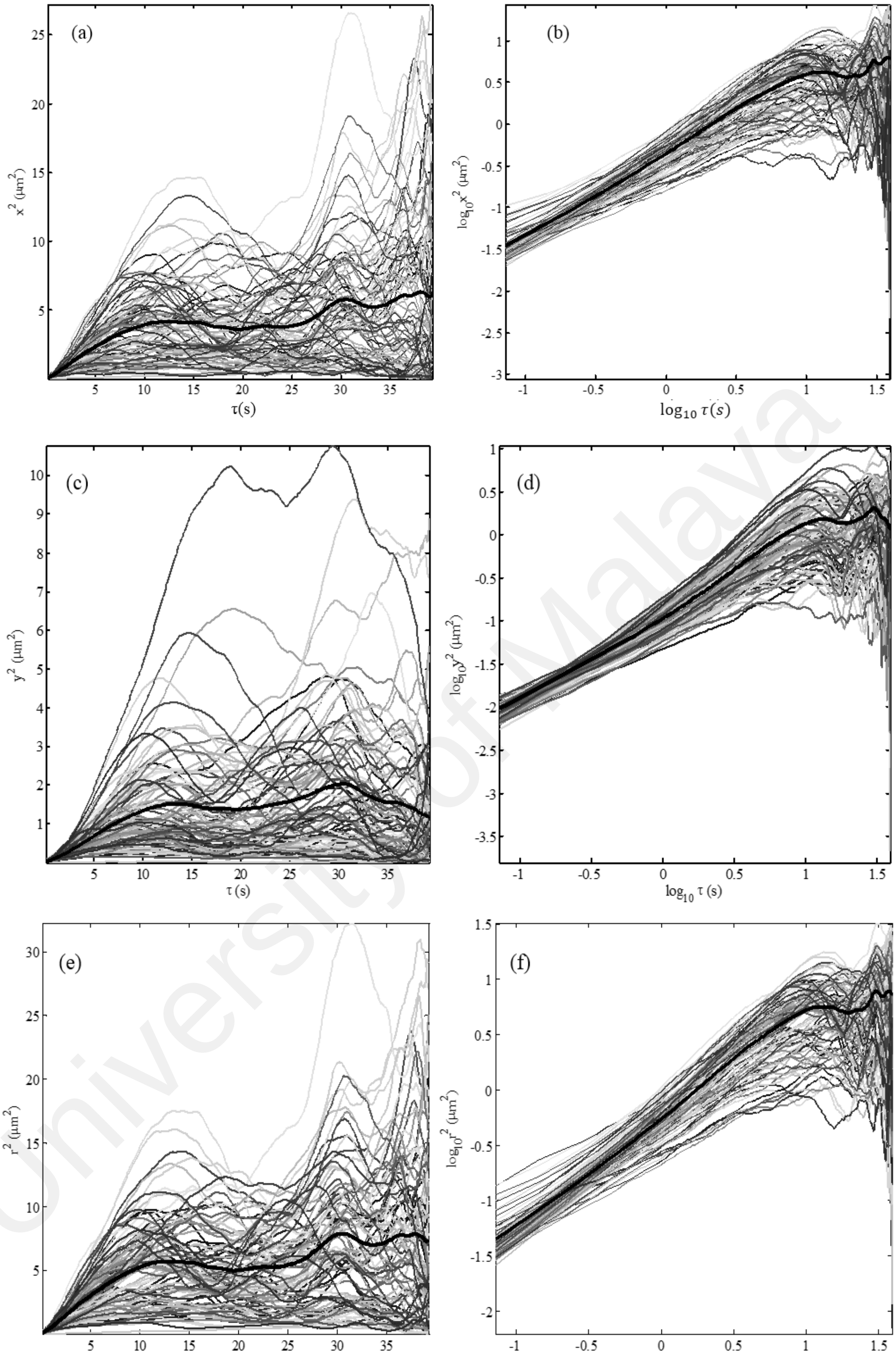

Figure 4.5: At the left-hand side are the MSD plot against lag time of the particles at: (a) *x*-direction, (c) *y*-direction, and (e) resultant direction. At the right-hand side are the bi-logarithmic MSD plot of the particles at: (b) *x*-direction, (d) *y*-direction, and (e) resultant direction.

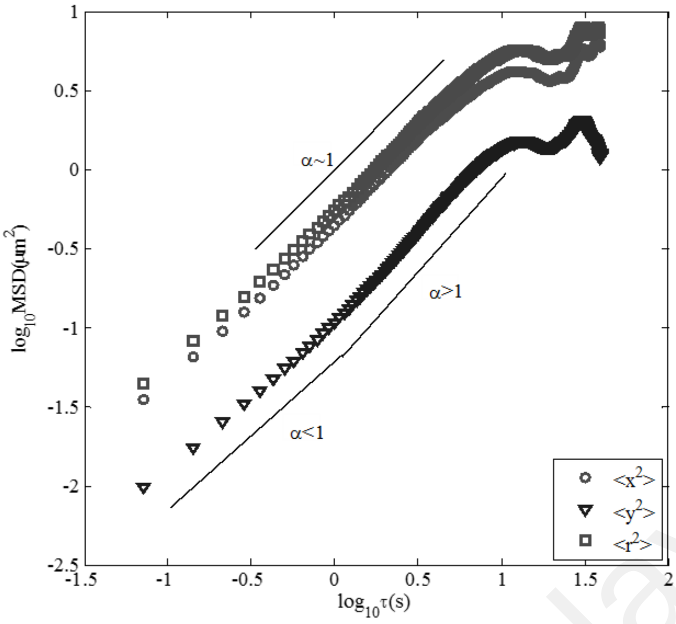

Figure 4.6: Averaged TAMSD in direction of *x* (circle), *y* (triangle), and resultant direction *r* (rectangle).

Table 4.5: MSDs results.

MSD	α_1	α_2	t_c (ms)
<x^2>	0.99± 0.01	0. 94± 0.02	3.00
<y^2>	0.93 ± 0.01	1.15 ± 0.01	3.00
<r^2>	none	0.98 ± 0.02	none

4.3 Particle tracking in microfluidics

4.3.1 Particle trajectories

In particle tracking analysis, the raw videos consist of 27927 and 62061 stack images for 2000 Hz and 3000 Hz respectively. The tracking duration and frame rate usage are vary based on the dynamics of the flow. Faster flow required high frame rate and small tracking duration since the particle is easily lost in the frame of observation. For illustration purpose, particles trajectories at different flow are plotted in Figure 4.7.

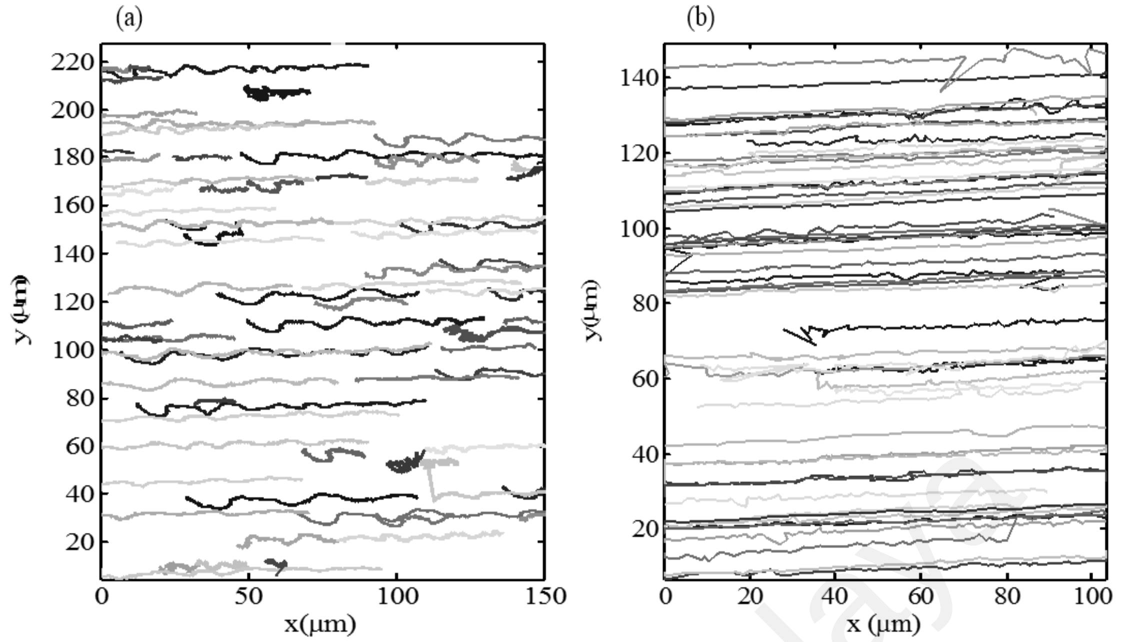

Figure 4.7: The representative sample of particles trajectories under flow rate of: (a) 0.2 μL/min, and (b) 0.3 μL/min.

The particles under both slow and fast flow move according to the streamline pathway, and some of the particles appeared to be "trapped" by the flow or upper wall. To differentiate between the trapped particle and moving particle, we imposed the condition of duration timewise, where the trapped particles will have slightly slow duration time and also appeared to be "brighter" compared to the rest of the particles.

At 0.2 μL/min some of the particles travel in "oscillatory" pathway with fluctuation, yet still following the streamlines. In 0.3 μL/min, the particles follow the streamlines with less fluctuation. Note that as the imposed flow getting faster, we obtained less point on the particle trajectories and the particle linking algorithm will become less accurate because the particles are likely to disappear from the observation frame. At higher frame rate, the light entering the CCD sensors is getting less, since the constant and unfocused illumination from high power LED is used. Thus, the particles at fast flow have less contrast with respect to the background, which degrades the tracking algorithm efficiency.

At the direction of flow (Figure 4.8(a)), the particles trajectories followed the deterministic trend with small fluctuation due to advective displacement. While in the tangential direction (Figure 4.8(b)), the particles trajectories exhibit stochastic trend with relatively high fluctuations as the dynamic of the particle is influenced by both shear stress and diffusion.

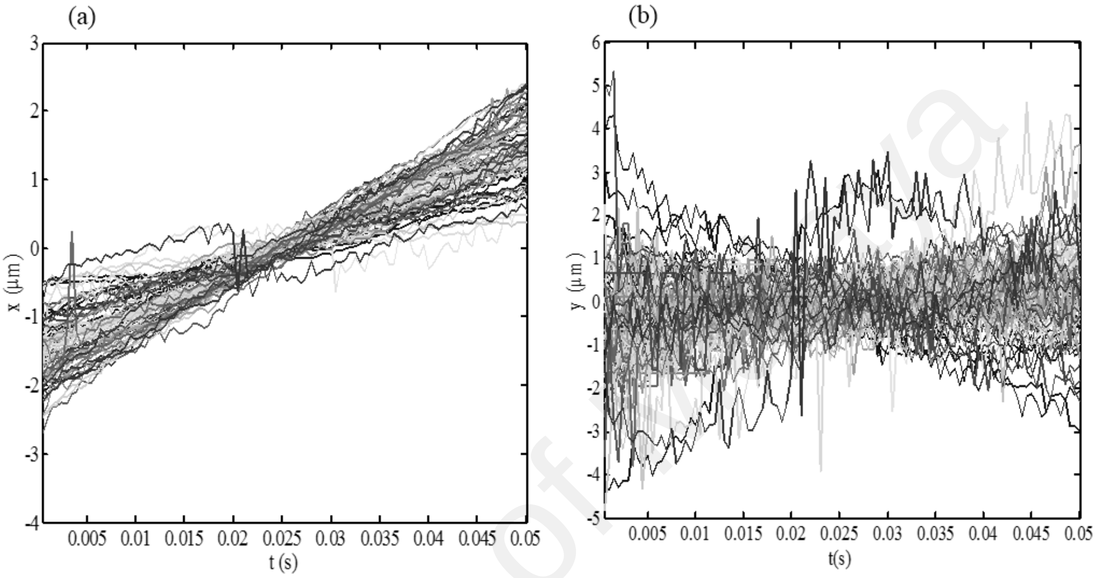

Figure 4.8: The representative sample of particles trajectories under flow rate of: (a) 0.2 µL/min, and (b) 0.3 µL/min.

One of the hallmarks of anomalous diffusion is a non-Gaussian form of the empirical distribution function PDF of the particle's displacement. The positions extracted from the trajectories of samples particle are de-mean (removing the mean value) with the individual particle mean before plotting the empirical distribution. As depicted in Figure 4.9 and Figure 4.10, the time evolution empirical distributions of microalgae displacement in respective flow region of NB_1, NB_2, and C under flow region 0.2 µL/min show remarkable form of anomality with the kurtosis behavior of the curves. At t = 0.5 ms, the particles displacement distributions curve in all respective flow region exhibit the non-Gaussian distribution indicated by high kurtosis value. The kurtosis value decreased with increasing time of the observation. This indicates the non-stationary state of the system. The distribution may converge to normal distribution at the longer time, however is unable to be verified in this study for the limited data points and due to poor statistics at large lag time. This similar behavior of distribution functions is also observed in the case of 0.3 μL/min (see Appendix B).

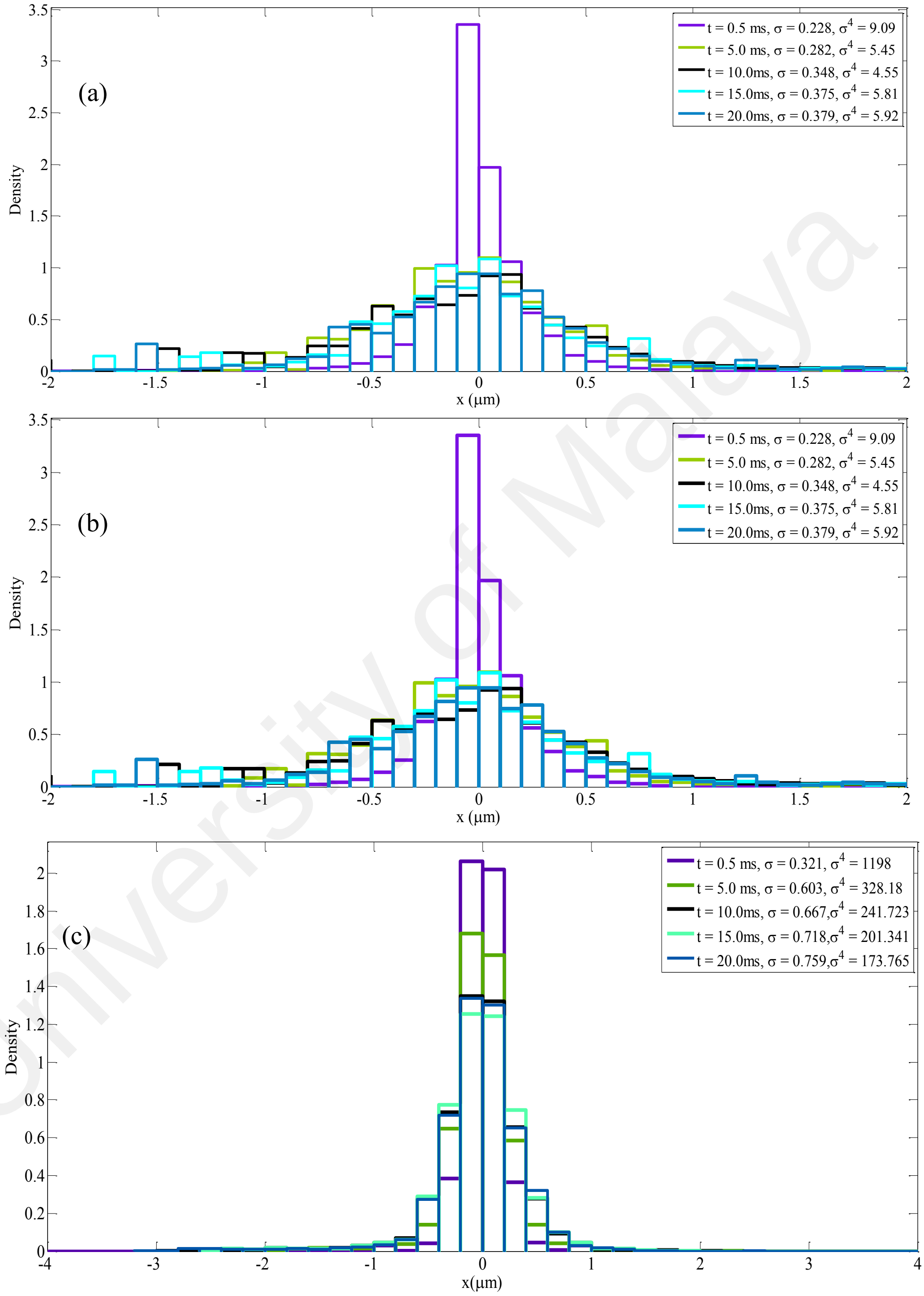

Figure 4.9: Representative empirical probability density function (PDF) of particles displacement at streamwise direction at different lag time of 0.005 s (purple),0.005 s (green), 0.01 s (black), 0.1 s (light-blue), and 0.2 s (blue) at respective flow regions of (a) NB_1, (b) NB_2, and (c) C under flow rate of 0.2 μL/min.

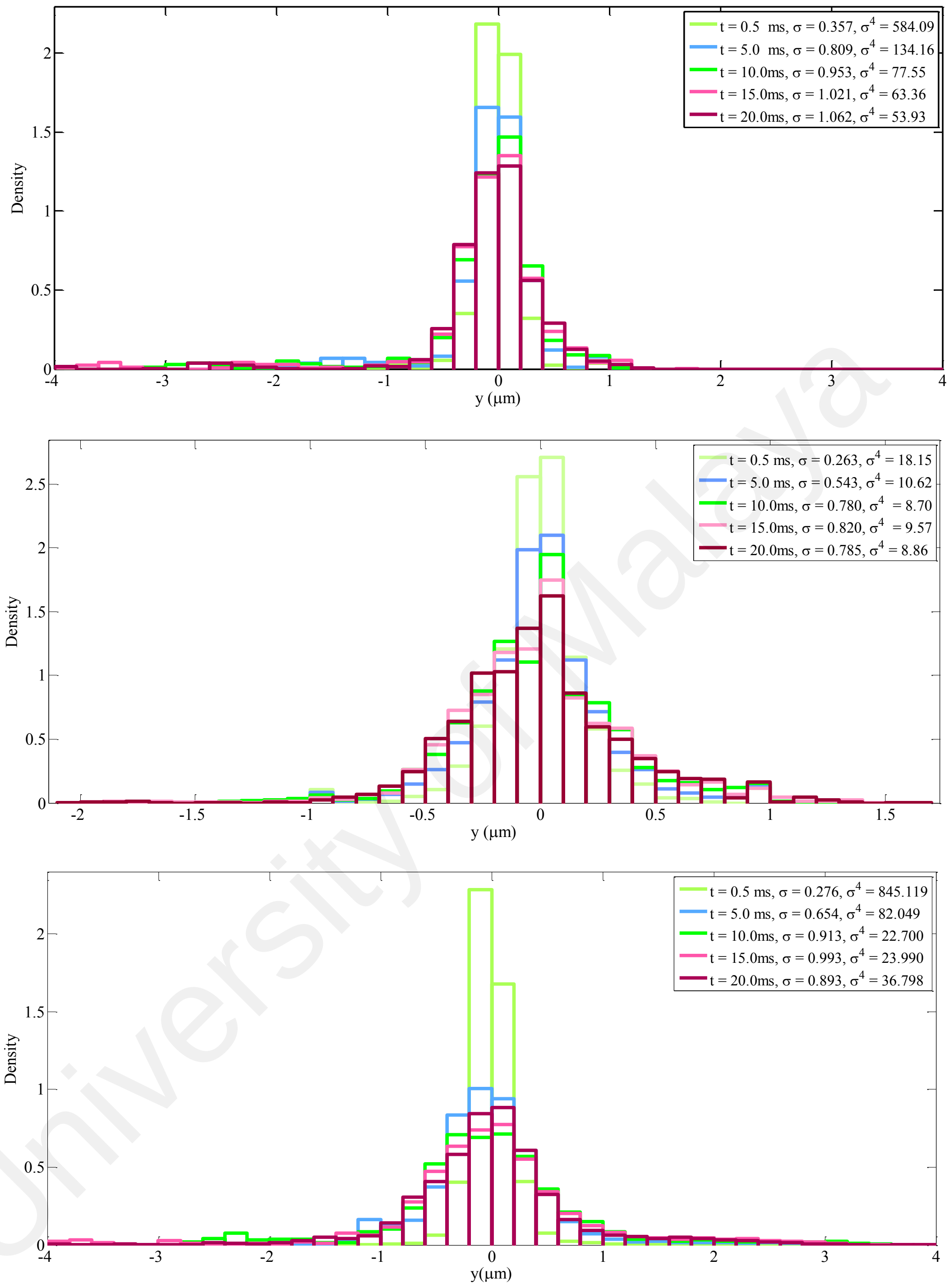

Figure 4.10: Representative empirical probability density function (PDF) of particles displacement at perpendicular direction at different lag time of 0.005 s (light-green),0.005 s (blue), 0.01 s (green), 0.1 s (pink), and 0.2 s (dark-red) at respective flow regions of (a) *NB*1, (b) *NB*2, and (c) *C* under flow rate of 0.2 µL/min.

4.3.2 Mean square displacement

We discussed the MSD in streamwise (x-component), perpendicular (y-component), and resultant direction. We focused mainly on the ensemble time average MSD (TAMSD) obtained by averaging the ensemble of particles that are in similar state. Figure 4.11 shows the representative of ensemble TAMSD in black thick line, while the grey lines represent the individual plot of TAMSD of a sample of 20~102 microalgae at flow region NB_2 under flow rate of 0.2 μL/min. More particles are tracked at relatively low flow rate compared to the highest flow. For more detailed plot of the individual plot of TAMSD in the rest of the flow regions and cases, refer to Appendix D.

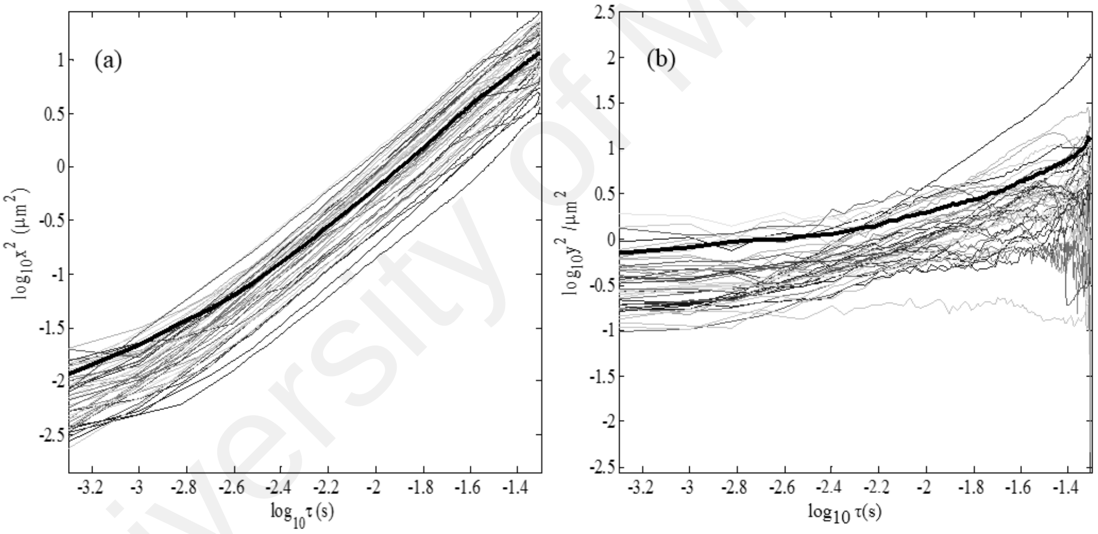

Figure 4.11: Log-log plots of TAMSDs of individual particle trajectories against lag time in (a) the *x*-direction and (b) the *y*-direction.

4.3.2.1 Perpendicular direction

In the perpendicular direction of the flows (Figure. 4.12), the bi-scaling power law regimes are observed at different time scales in all regions for both slow and fast flows. The scaling exponent at the short time interval ($t < 3.00$ ms) or ($t < 2.00$ ms) in respective different flow rates cases indicate the existence of the slow transport, which later ($t > 0.30$ ms) or ($t > 2.00$ ms) switches to the fast transport mode.

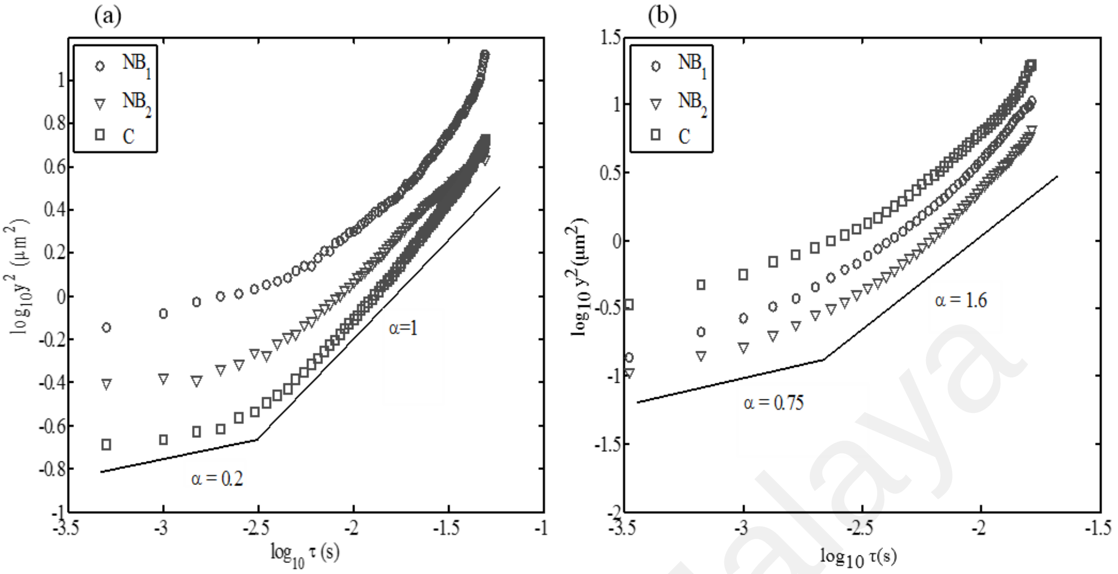

Figure 4.12: Log-log plot of MSD at perpendicular direction versus lag time for three different regions NB_1(circles), NB_2 (triangles), and C (rectangle) under flow rate: (a) 0.2 µL/min, and (b) 0.3 µL/min.

Under slow flow rate 0.2 µL/min and at a shorter time, the particles exhibit the sub-diffusion with MSD scale as $t^{0.23}$, $t^{0.16,}$ and $t^{0.19}$ for NB_1, NB_2, and C, respectively as shown in Figure 4.12(a). Later in a long time, it changes to a faster transport $t^{0.88,}$ $t^{0.85}$, and $t^{1.05.}$ The scaling exponent in both near wall boundary regions NB_1 and NB_2 respectively, indicates the strong sub-diffusion behavior takes place at the shorter time, which then switch to the weak sub-diffusion at longer time. Interesting behavior of the transport at the core of the channel region is observed where the scaling exponents at the shorter time show weak sub-diffusion behavior then shifted to normal diffusion at a longer time interval. This manifest the existence of slow and fast modes.

Under fast flow at 0.3 µL/min, the particles transported in sub-diffusive motion at a shorter time with MSD scale as $t^{0.73}$, $t^{0.61}$, and $t^{0.55}$ for NB_1, NB_2, and C, respectively, as seen in Figure 4.12(b). This reducing trend of scaling exponent value from NB_1, NB_2 to C region also been reported elsewhere (Yeo & Maxey, 2010). In long time, this switch to super-diffusive for faster dynamic with MSD scale as $t^{1.70}$, $t^{1.69}$, and $t^{1.62}$ for NB_1, NB_2, and C respectively, due to the irregular jump and particle entrapment in particle layers. Similar pattern of MSD transition is also observed in case of 0.2 µL/min, however at much shorter time as t_c ~2.00 ms.

The transition between the biscaling power-law behaviors at both slow and fast flows can be modelled using the SBM by introducing different scaling exponents for short time α_1, and long time α_2 as:

$$\langle X^2(t)\rangle = \begin{cases} t^{\alpha_1} & t < t_c \\ t^{\alpha_2} & t > t_c \end{cases} \tag{4.1}$$

where t_c is crossover time. The results are summarized in Table 4.6.

Table 4.6: MSDs scaling in perpendicular direction results.

Flow rate (µL/min)	**Cases**	$\boldsymbol{\alpha_1}$	$\boldsymbol{\alpha_2}$	$\boldsymbol{t_c}$ **(ms)**
0.2	NB_1	0.23 ± 0.01	0.88 ± 0.01	3.00
	NB_2	0.16 ± 0.03	0.85 ± 0.02	3.00
	C	0.19 ± 0.02	1.05 ± 0.01	3.00
0.3	NB_1	0.73 ± 0.03	1.70 ± 0.03	2.00
	NB_2	0.61 ± 0.03	1.69 ± 0.01	2.00
	C	0.55 ± 0.01	1.62 ± 0.03	2.00

The scaling exponents obtained at the symmetrical regions of NB_1 and NB_2 are different as shown in Table 4.6. At the early time, the percentage differences of the scaling exponent α_1 between both regions NB_1 and NB_2 are 36.0 % and 18.0 % in cases of 0.2 µL/min and 0.3 µL/min, respectively. The high percentage differences obtained in both symmetric regions NB_1 and NB_2 reveal that the particles dynamic is not-symmetric. This behavior is inconsistent with the initial assumptions on the symmetrical Poiseuille velocity flow profile. While at longer time, the percentage difference of α_2 are reduced to 3.5 % at 0.2 μL/min, and 0.6 % at of 0.3 μL/min. The behavior of the particles was therefore observed to be almost symmetric.

Next, the comparison of percentage difference of α_1 and α_2 at the region NB_1/NB_2 with respect to the region C is 19.0 % and 17.1 %, respectively in 0.2 μL/min. While in 0.3 μL/min the respective percentages difference on these regions are 28.1 % and 10.3 %. At the latter time, the percentage difference of scaling exponent α_2 are 17.6 % and 21.1 % for 0.2 μL/min and 4.8 % and 4.2 % for 0.3 μL/min at the respective flow regions. The difference of the scaling exponent α_1 are relatively high at early stage while at the latter time, the difference is almost in the same order.

The observation of the scaling exponent of the MSD is further examined in the profile of the normalized velocity autocorrelation function (NVACF). The NVACF of the particles can also be interpreted by using Fractional Gaussian Noise (FGN) correlation (see Chapter 2; Section 2.2.1.1) in terms of memory of the process. The Hurst index H related to the MSD scaling exponent α by $H = 0.5\alpha$. In the case of perpendicular direction, the NVACF profile at both slow and fast flow cases shows the distinct features of negative correlation value at a time interval of $t \sim 0.5$ ms and $t \sim 0.3$ ms. This pattern is shared at all flow regions of NB_1 , NB_2, and C as shown in Figure (4.13). The dip (negative correlation) of NVACF based on the FGN model correspond to the anti-persistent motion of particle, where the particle has short time memory as increment of particle's velocity converge very fast to finite values. In fact, this anti-persistent type motion can be associated with the sub-diffusion motion and is in line with the value H exponent obtained ($H < 0.5$).

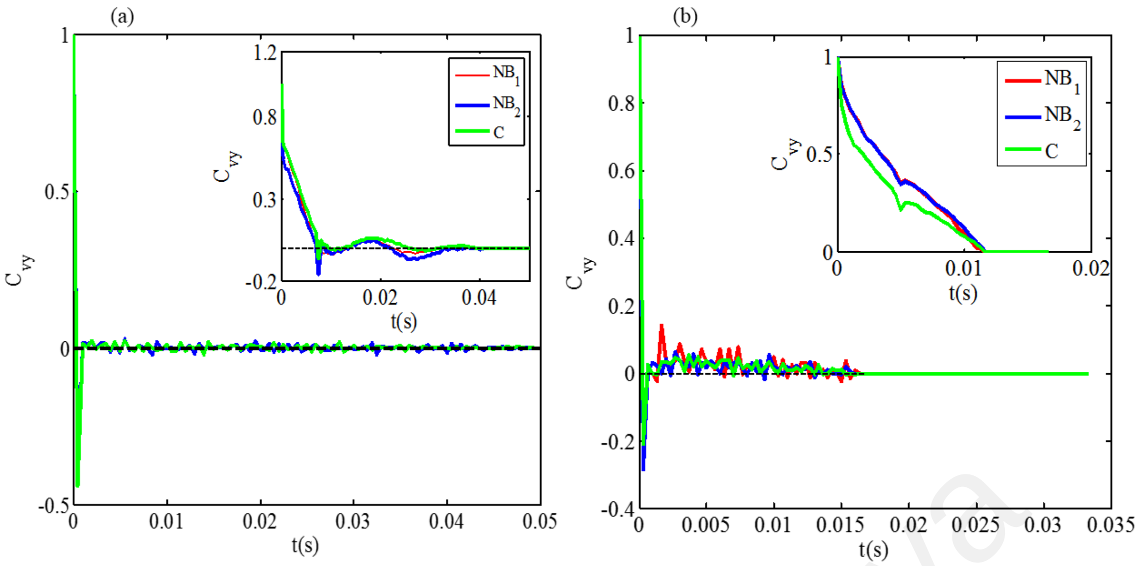

Figure 4.13: NVACF of particles flow in perpendicular direction under flow rate of: (a) 0.2 µL/min, and (b) 0.3 µL/min at for three different regions *NB*1 (red), *NB*2 (blue), and *C* (green).

The autocorrelation function is only valid for the (weakly) stationary process. Stationary process is a random process with the same variance and mean value at all given time. The observation of time-dependent scaling exponent implies that there is an underlying non-stationary behavior. The autocorrelation of the non-stationary process has distinct value at particular lag time τ. As demonstrated by the result, the profile of NVACF at long time regime is not fully captured by simply calculating the autocorrelation function of velocity at initial time t_0. Hence, the velocity correlation is calculated based on the particle's velocity at the various lag time $\tau = 2t_0, \tau = 5t_0$, and $\tau = 10t_0$ (see Appendix E for the plot) (Reverey et al., 2015). The particle retains the sub-diffusive behavior at all choices of lag times. The analysis on the NVACF profile at long time interval taken at $\tau = 5t_0$ corresponding to real time $t{\sim}0.3$ ms seem to be a good choice, since it marked the transition time for particles to transit from slow to fast transport.

The NVACF at the long-time scale for respective flow cases at different flow profile is shown in the inset of Figure 4.13. Clearly, the NVAF plot for particle at 0.2 µL/min (inset Figure 4.13(a)) at the respective flow regions of NB_1, NB_2 , and C has negative correlation value at $t \sim 7.5$ ms before it oscillates around zero value. This is in alignment with H exponent found in these three regions, which stand for the weak sub-diffusive ($H < 0.5$) and Brownian motions ($H = 1$). From the FGN point of view, the sub-diffusive motion is due to anti-persistent motion ($H < 1/2$), as the particle has short time memory. There is no preference direction in increment of the particle velocity. In the case of 0.3 μL/min, the long-time profile NVACF exhibits positive correlation, and the motion is persistent. The particle has long time memory as the increment of the particle's velocity persists in the positive sign. This owing to the super-diffusion nature of particle as indicated by value of H scaling exponent at long time scale ($H > 0.5$).

4.3.2.2 Streamwise direction

Under 0.2 μL/min flow rate in the streamwise direction, the bi-scaling power-law regimes at different time scales are observed as shown in Figure 4.14(a). The particle at all flow regions exhibits the weakly super-diffusive behavior at short time scale with MSD as $t^{1.20}$, $t^{1.14}$, and $t^{1.18}$ for NB_1, NB_2, and C, respectively. Later at the longer time, it switched to a faster dynamic with MSD scale as $t^{1.86}$, $t^{1.78}$, and $t^{1.82}$ and for NB_1, NB_2, and C respectively.

The percentage differences of scaling exponent α_1 between the symmetrical flow region of NB_1 with respect to NB_2 region at a flow rate of 2.0 μL/min is 5.0 % and scaling exponent α_2 is 4.4 %. These small percentage differences indicate the behaviors of the particles are symmetric at these regions as contrast to the perpendicular direction case. This symmetrical nature arises because the particles dynamic in streamwise direction experienced less fluctuation. The presence of the wall restricts the space available for the particle to interact with the local flow and the drag force at the normal-wall direction is higher. Thus, the scaling exponent of the particle is reduced.

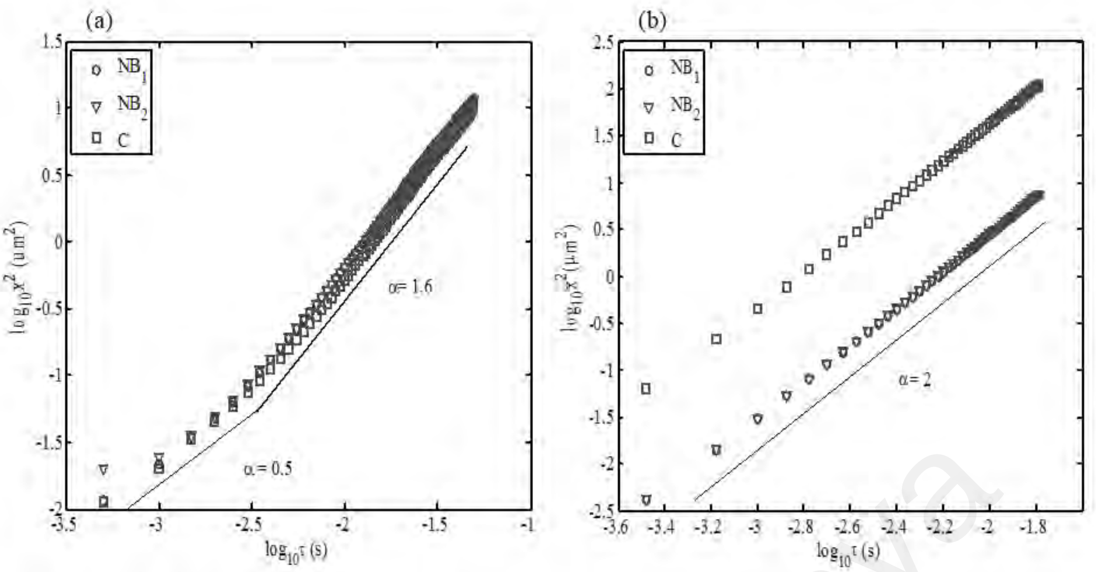

Figure 4.14: Ensemble log -log TAMSD versus lag time of particles flow in streamwise direction under flow rate of: (a) 0.2 µL/min, and (b) 0.3 µL/min at for three different regions *NB*₁ (circle), *NB*₂ (triangle), and *C* (rectangle).

The comparison of the percentage difference of scaling exponents at NB_1 and NB_2 with respect to C yield 1.7 % and 3.5 % respectively for α_1, while for α_2 are both 2.2 %. Again, this result implied the symmetrical nature of the particles at both symmetrical regions. Exceptionally, the reduced scaling exponent values of α_1 and α_2 was found at region C relative to the NB_1 region (see Table 4.7). These reduced scaling exponents in region C can be interpreted by the fact that some of the particles at center region instantly moves to the NB_1 region and slowing down their motion. Hence, breaking down the isotropy of the particle's MSD in the Poiseuille flow.

In the case of faster flow at 0.3 µL/min, the bi-scaling exponent perishes at all the three regions where MSD is scaled as $t^{1.92}$, $t^{1.97}$, and $t^{1.98}$ for NB_1, NB_2, and C, respectively with mono-scaling exponents, as shown in Figure 4.14(b). The percentage differences of scaling exponent at region NB_1 and NB_2 is 2.0 %. The comparison of percentage difference at regions NB_1 and NB_2 relative to C, results in value of 3.1 % and 0.5 %, respectively. The behavior of the particles is symmetric as the particles were transported almost at the same rate. For the particle transported under fast flow, its dynamic is monopolized by the effect of flow advection thus minimizing the wall effect on the particle located at both NB_1 and NB_2 regions.

Table 4.7: MSDs scaling in streamwise direction results.

Flow rate (μL/min)	Cases	α_1	α_2	t_c (ms)
0.2	NB_1	1.20 ± 0.01	1.86 ± 0.01	3.00
	NB_2	1.14 ± 0.02	1.78 ± 0.01	3.00
	C	1.18 ± 0.01	1.82 ± 0.01	3.00
0.3	NB_1	None	1.92 ± 0.01	none
	NB_2	None	1.97 ± 0.01	none
	C	None	1.98 ± 0.01	none

The particle velocity autocorrelation NVACF in the streamwise direction at both slow and fast flow cases are illustrated in Figure 4.15. In the case of 0.2 μL/min, the NVACF has dip value at time t ~ 0.5 ms (Figure 4.15(a)) corresponding to restricted sub-diffusive motion. The visualization of the NVACF at respective flow regions NB_1,NB_2, and C at long time interval taken at $\tau = 5t_0$ (inset Figure 4.15(a)) displays the positive correlation due to persistent motion of the particle. These profiles are consistent with the transition of H scaling exponent ($H > 0.5$) as super-diffusive.

The negative correlation at a short time again can be associated with backscattered of particles displacement before it can overcome its inertia. At the later time as the inertia dominates the local region, the particle has positive correlations in the displacement. For the fast flow 0.3 μL/min, the VACF of the particle exhibit the positive correlation value and has fast decay. This positive correlation of the particle driven under flow rate of 0.3 μL/min manifested the persistent dynamic at both short and long time again is in line with the previous observation of mono-scaling MSD scaling exponent.

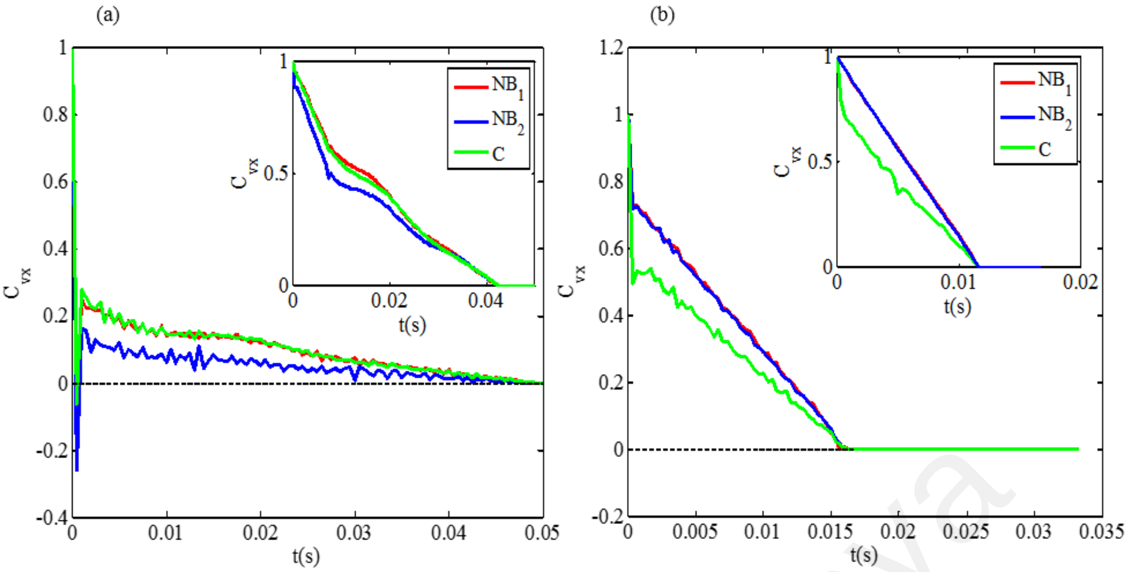

Figure 4.15: VACF of particles flow in streamwise direction under flow rate of: (a) 0.2 µL/min, and (b) 0.3 µL/min at for three different regions *NB₁* (red), *NB₂* (blue), and *C* (green).

4.3.2.3 Resultant MSD

Similarly, with the case of perpendicular direction, the particles flow at each respective flow rate of 0.2 µL/min and 0.3 µL/min in all flow regions show the bi-scaling MSD power-law behavior occurring at a time interval (t ~ 3.00 ms) or (t ~2.00 ms).

The particle transported under flow of 0.2 µL/min exhibits the sub-diffusion behavior at early time in all flow regions of NB_1, NB_2, and C with MSDs scale as $t^{0.78}$, $t^{0.57}$, and $t^{0.73}$, respectively. Later in time, the particle MSD scale as $t^{1.31}$, $t^{1.25}$, and $t^{1.23}$, at the respective flow region, indicating the super-diffusion behavior. The particle at NB_1 region undergoes the fastest transport relative to other flow regions, as it exhibits highest scaling exponent in the case of streamwise direction (Figure 4.16(a)). The identical transition behavior is also noted in the case of particles flow under flow rate of 0.3 µL/min (Figure 4.16(b)). At short time, particles experienced weak sub-diffusive transport with MSD's scaled as $t^{0.86}$, $t^{0.82}$, and $t^{0.95}$ in respective region of NB_1, NB_2, and *C*. At the longer time, the particle shift into faster super-diffusive behavior as the MSD's scaled into $t^{1.81}$, $t^{1.84}$, and $t^{1.86}$ in regions NB_1, NB_2, and *C,* respectively.

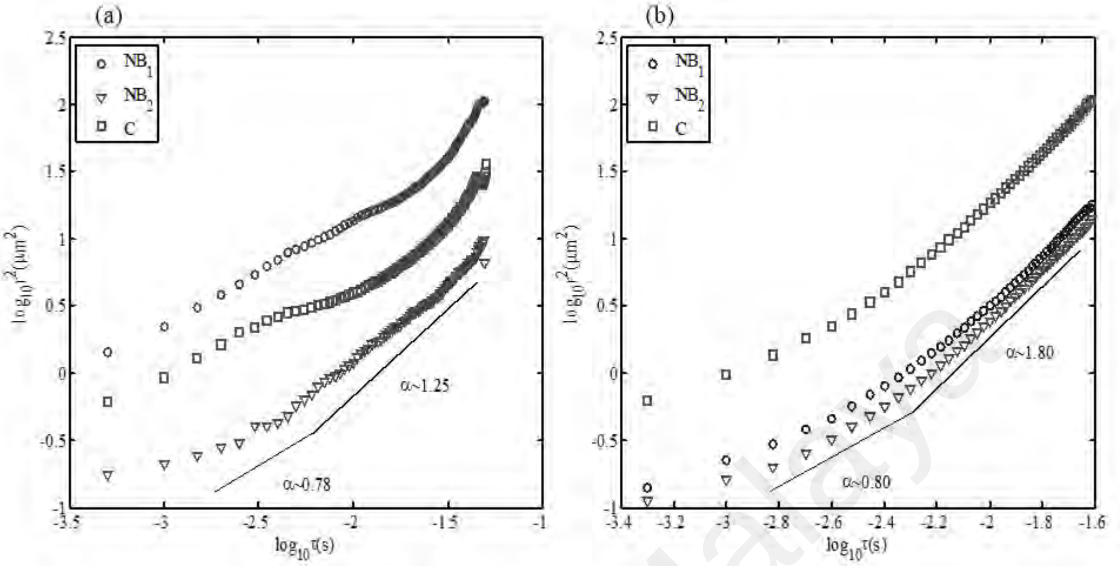

Figure 4.16: Resultant MSD under (a) 0.2 µL/min and (b) 0.3 µL/min for different flow regions NB_1 (circle), NB_2 (triangle), and *C*(rectangle).

Again, the SBM model is applied to simulate this power law transition of MSDs and the scaling exponent at both short and long time is tabulated in Table 4.8. In the cases of 0.2 µL/min and 0.3 µL/min, at the early time, the respective percentage differences of the scaling exponent α_1 at symmetrical regions NB_1 and NB_2 are 31.1 % and 4.76 % respectively. While at the later time, the percentage difference of α_2 are reduced such that 4.7 % at 0.2 µL/min, and 1.6 % at of 0.3 µL/min. The significantly large percentage differences of α_1 suggest the particles dynamic is not-symmetric at the early time of transport, then retain the symmetrical behavior at the later time indicated by the small percentage difference of α_2. These are expected results since the scaling exponent obtained from both streamwise and perpendicular direction also show the relative high percentage difference at early time of flow and it is reduced at the later time.

Table 4.8: Resultant two-dimensional MSD's

Flow rate(μL/min)	Cases	α_1	α_2	t_c (ms)
0.2	NB_1	0.78 ± 0.03	1.31± 0.03	3.00
	NB_2	0.57 ± 0.03	1.25 ± 0.03	3.00
	C	0.73 ± 0.02	1.23 ± 0.06	3.00
0.3	NB_1	1.81 ± 0.02	1.81 ± 0.02	2.00
	NB_2	0.82 ±0.05	1.84 ± 0.01	2.00
	C	0.95 ±0.03	1.86 ± 0.01	2.00

The MSD's scale maximum at the center region C of the channel at both short time and long-time regimes in all flow cases. These behaviors correspond to the smallest shear rate and highest velocity profile at the C region i.e. the particles experience less shear and inherit more velocity in this region. In other hand, the particles flow at the regions of NB_1 and NB_2 encounter high shear rate associated and inherit small velocity from the flow.

Moving on to the profile of NVACF, at slow and fast flow cases, the correlation in all flow regions has the minimum dip at short time interval at $t \sim 0.5$ ms (Figure 4.17(a)) and $t \sim 0.3$ ms (Figure 4.17(b)). The motion is anti-persistent, which corresponds to the sub-diffusive behavior as shown in value H scaling exponent ($H < 0.5$). The particle has short time memory. While at a long time, the NVACF exhibit the positive correlation indicating the persistent type motion, before it de-correlate to zero. This correlated profile of NVCF is shown in insets of Figure 4.17(a) and (b) at lag time $\tau = 5t_0$, where particles retained the sign of increment due to its long-term memory effect. Again, this behavior is properly captured by the scaling exponent retained the sign of increment due to its long-term memory effect. Again, this behavior is properly captured by the scaling exponent of H at long time interval ($H < 0.5$).

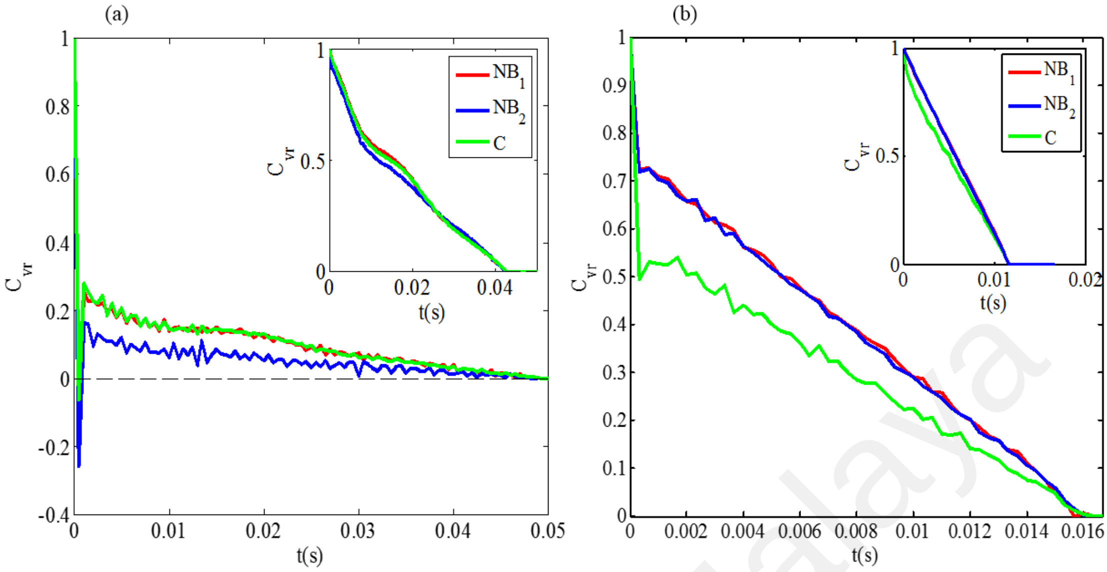

Figure 4.17: Resultant NVACF of particles flow under flow rate of: (a) 0.2 µL/min, and (b) 0.3 µL/min at for three different regions NB_1 (red), NB_2 (blue), and C (green).

4.4 Numerical particle tracing in microfluidic experiment

In this section, the numerical simulation results of the fluid flow field and the particle tracing from the CFD simulation are presented. Particularly, this section provides the comparison of the results from both flow experiments and simulations. Here any result obtained via the laboratory flow experiments is referred as experimental results, while the results derived from the numerical simulation is represented as simulated results, unless if mentioned otherwise. The definition of flow regions was used similarly as in the experimental case.

4.4.1 Flow field

The simulation contour plot of flow profile in the microfluidic channel is illustrated in Figure 4.18. The flow has the highest velocity at the center of the channel, while the lowest velocity at the near wall region.

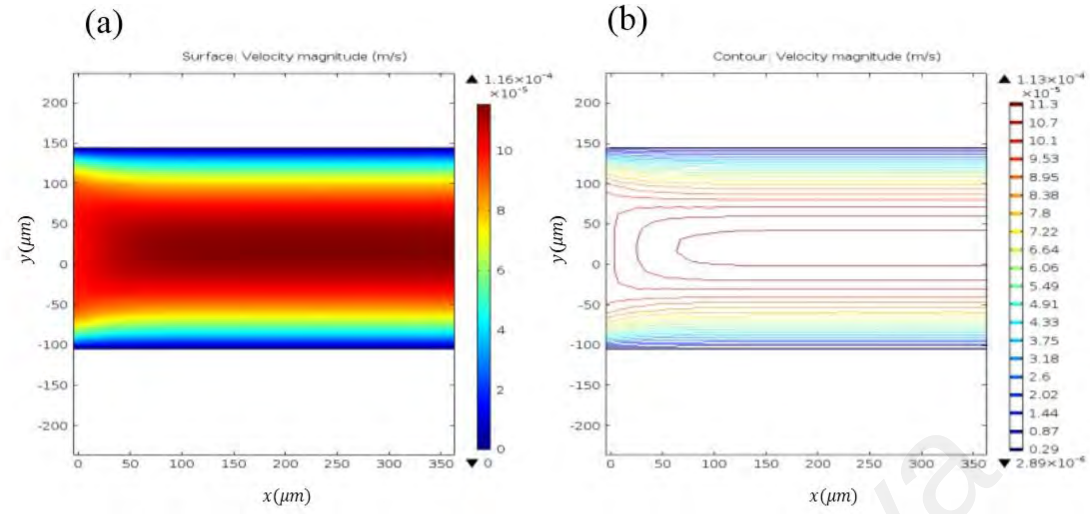

Figure 4.18 : Simulation fluid profile (a, b) contour velocity profile.

The flow across the arc length or width of the channel is shown in Figure 4.19. The velocity in the streamwise direction (x) shows parabolic velocity profile known as Poiseuille flow (Figure 4.19(a)). In the streamwise direction, the fluctuation of the flow velocity is the highest at near wall boundary regions of NB_1 and NB_2, while smallest at the center region C (Figure 4.19(b)). The resultant flow velocity (Figure 4.19(c)) magnitude is dominated by the velocity field in streamwise direction. Due to implication and assumption of the pressure driven flow and incompressible flow, the pressure across the arclength/width of the channel remains constant (Figure 4.19(d)). As the consequences of the non-uniform velocity profile, the shear rate is maximum at both the channel's walls (where the fluid is at rest), while minimum value was at the center of the wall (where the fluid possesses maximum velocity) shown in Figure 4.19(e).

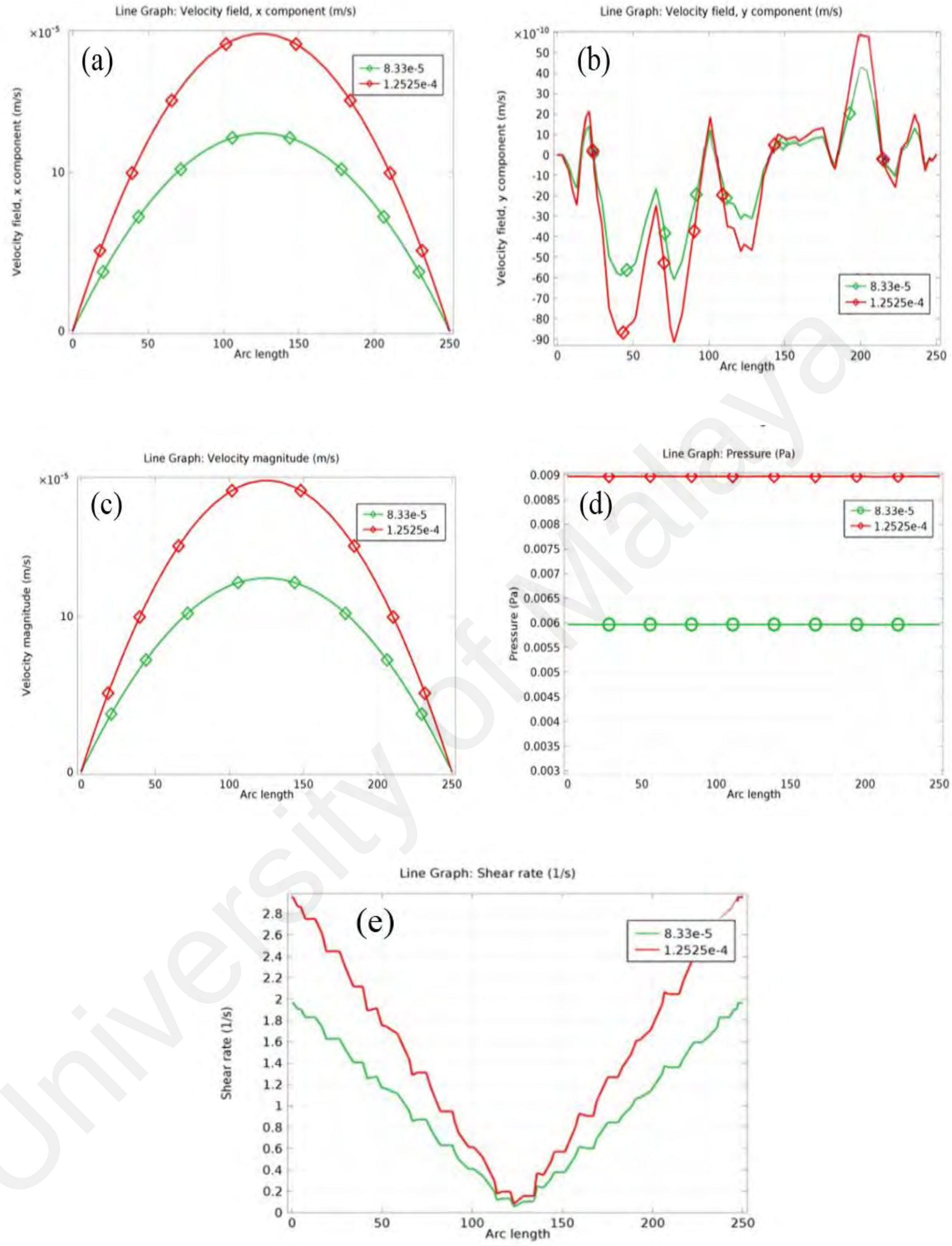

Figure 4.19: Flow profile characteristics across the arclength (of the channel in case of 0.2 µL/min(green), and 0.3 µL/min(red). (a) velocity field profile in *x*-direction, (b) velocity field profile in *y*-direction, (c) overall velocity magnitude, (d) pressure, and (e) shear rate.

4.4.2 Particle trajectories

The five repetitions of simulations were done for system time of 5 s. The coordinates of the particles are saved within time step of 0.001 s. Particle as grouped based on its location with respect to the Segre'–Silberberg radius (see Chapter 3, Section 3.3.3.1) at respective distance of 0 μm < r_{eq}<50 μm (NB_1) and 200 μm < r_{eq}< 250 μm (NB_2) consisting of five sample particles, while at distance of 50 μm < r_{eq}< 200 μm (C) consisting 20 sample particles. Since the observations in real-life flow experiment are taken at the middle length of microfluidic channel, the data points at the early stage of the flow are ignored and the data of particle coordinates were only extracted after the velocity profile was perfectly developed and when the particles have already reached the equilibrium position.

From the obtained coordinates, the standardized particle position in the streamwise and perpendicular direction are plotted as shown in Figure 4.20. The position of the particles in streamwise direction show the fully deterministic trend (Figure 4.20(a)), which is different from the experimental data as the particles experience slight fluctuations. While in perpendicular direction, the particles exhibit the fluctuation in position within the range of $[-3\ \mu\text{m}, 3\ \mu\text{m}\,]$, which is smaller compared to what was observed in experimental particle positions.

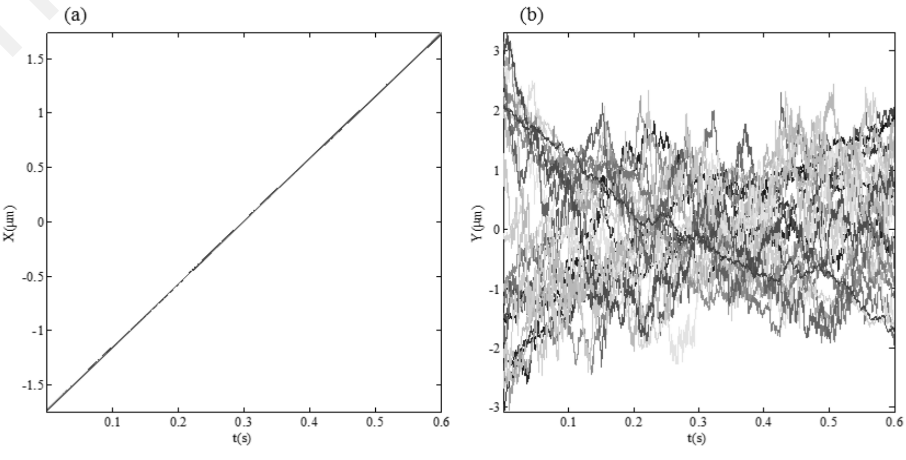

Figure 4.20: Spatial *x* and *y* of 25 particles trajectories. Standardized (a) spatial *x* and (b) *y* particles trajectories.

In order to determine the distribution of the system, the PDF of particles displacement are plotted at different evolution time t = 0.01 ms, 0.10 ms, 0.20 ms, 0.30 ms, and 0.024 ms with the red dot lines represent the Gaussian distribution fitting into the data as shown in Figure 4.21. The system exhibits the Gaussian behavior at both slow and fast flows in all flow regions. The particles dispersed with normal Gaussian distribution since the spread of distribution gets wider with time evolution, which is not observed in the experimental results. The particles distribution of the particles is symmetric at both NB_1 and NB_2 regions and C region.

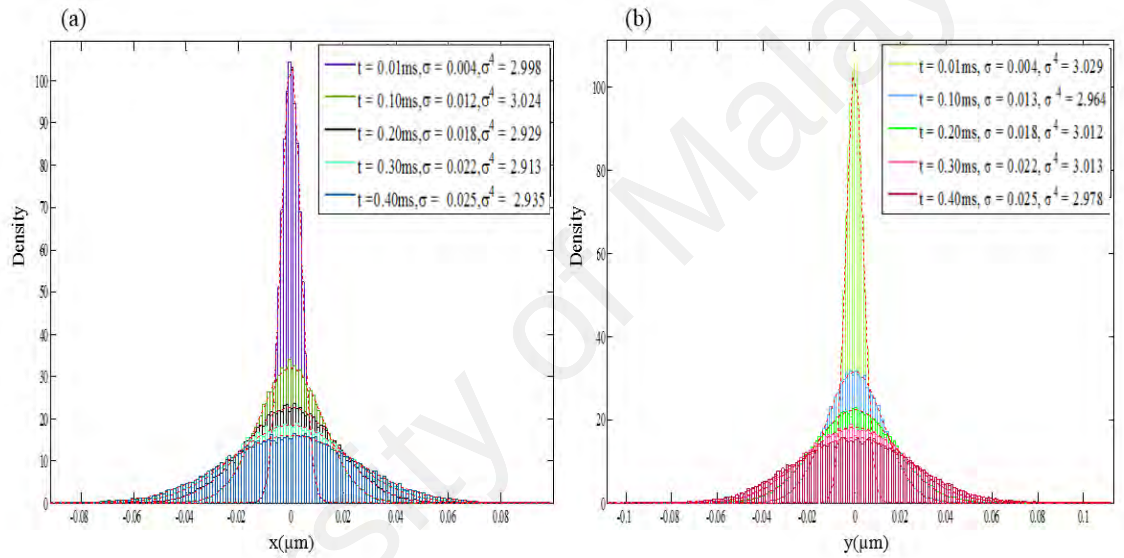

Figure 4.21: Empirical probability density function PDF of the particles displacement at 0.2 μL/min at (a)streamwise direction and (b) perpendicular direction (right). The dash red lines represent the Gaussian distribution fitted to empirical distribution.

4.4.3 Mean square displacement

The results of the MSD extracted from the simulation are presented in the similar manner as the experimental results.

4.4.3.1 Numerical streamwise direction of MSD

For the flow rate of 0.2 μL/min, in the streamwise direction, MSD scale with the mono-scaling with $t^{2.00}$ at all flow regimes are shown in Figure 4.22(a). The behavior of the particles is symmetric in all flow regions of B_1, NB_2, and C as the particles are transported in similar rate of ballistic motion (see Table (4.9)). This behavior is not observed in experimental MSDs as simulated particle trajectories do not show any fluctuation as with the experimental trajectories. The same patterns are also observed in case of 0.3 μL/min simulated flow rate (Figure 4.22(b)), which show similar behavior as the experimental MSD.

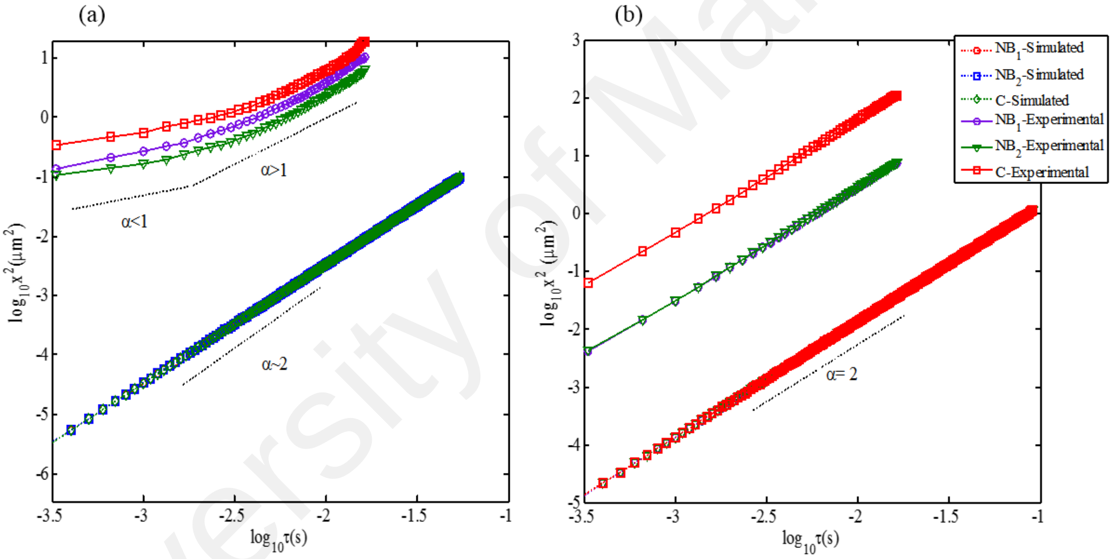

Figure 4.22: Streamwise direction of simulated TAMSDs (dash line) and experimental TAMSDs (full line) under flow rate of (a) 0.2 μL/min, and (b) 0.3 μL/min at for three different regions *NB₁* (blue circle), *NB₂* (green triangle), and *C* (red rectangle).

At 0.2 μL/min, the percentage difference of the scaling exponent α_1 at region NB_1, NB_2, C with respect to the experimental scaling exponent at the same region are 49.5 %, 54.3 %, and 51.6 %, respectively. While the comparison of α_2 yields the percentage difference of 7.3 %, 11.6 % and 9.4 % in respective flow regions. The large percentage difference of scaling exponent at early time shows the disparity between the behaviors of the simulated particle with respect to experimental particle behavior. While, it is noticed the disparity between the obtained results in both cases is reduced at longer time scale. Next, the same comparison of scaling exponent α_2 is done at the case of 0.3 μL/min resulted in 4.1 %, 1.5 % and 1.0 % at respective regions of NB_1, NB_2, and C. This smaller percentage difference shows the results of simulation agreed with the experimental results.

Table 4.9: Numerical MSD's results in streamwise direction

Simulated flow rate (μL/min)	**Cases**	α_1	α_2
0.2	NB_1	1.99± 0.01	2.00 ± 0.01
	NB_2	1.99 ± 0.03	2.00 ± 0.02
	C	2.00 ± 0.02	2.00 ± 0.01
0.3	NB_1	None	2.00 ± 0.01
	NB_2	None	2.00 ± 0.02
	C	None	2.00 ± 0.01

The velocity autocorrelation function NVACF of the particles in streamwise direction of 0.2 μL/min and 0.3 μL/min are shown in Figure 4.23. At 0.2 μL/min and 0.3 μL/min, the NVACF increment in all respective flow regions exhibit the positive correlation value at long time interval (inset Figure 4.23(a) and Figure 4.23(b)), before de-correlated to zero value at maximum lag time. This persistent motion resulted from the long-term memory, due to nature of ballistic nature if particle motion as indicated by the scaling exponent H value ($H > 0.5$).

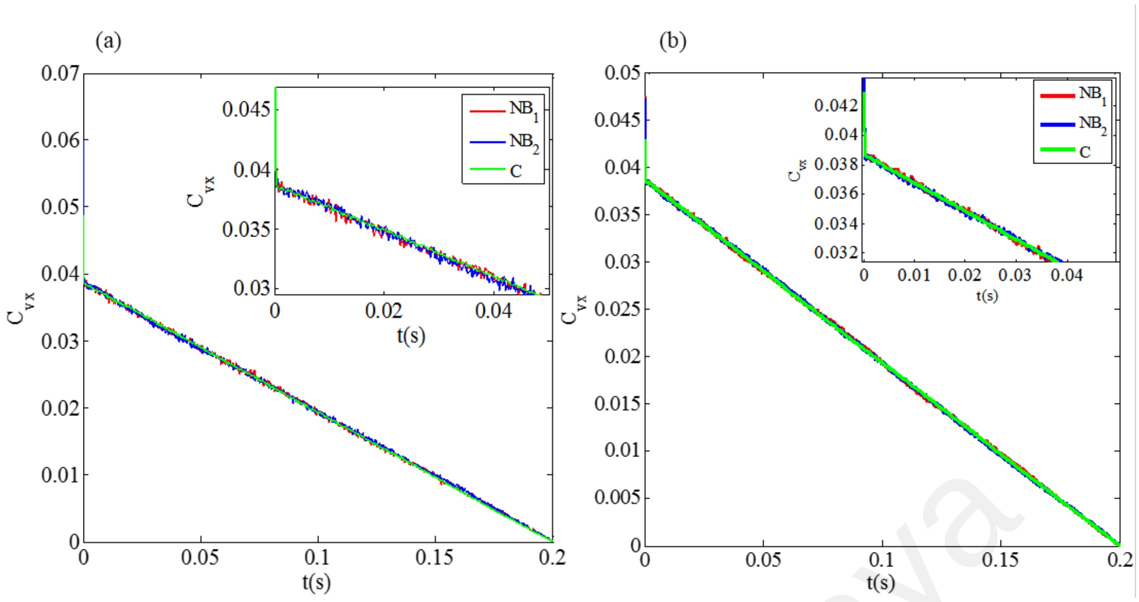

Figure 4.23: Streamwise NVACF in flow region of *NB*1(red), *NB*2(blue), and *C* (green) at: (a) 0.2 µL/min and (b) 0.3 µL/min.

4.4.3.2 Numerical perpendicular direction of MSD

The MSD in the perpendicular direction at both fast and slow flows exhibit the scale power law regime as shown in Figure 4.24. The particle undergoes slow dynamic at short time interval (t <10.00 ms) or (t <3.6 ms) in respective different flow rates later (t >10.00 ms) or (t >3.6 ms) switches to the fast transport mode. This transition dynamics are also observed in the experimental MSD, but with earlier transition time.

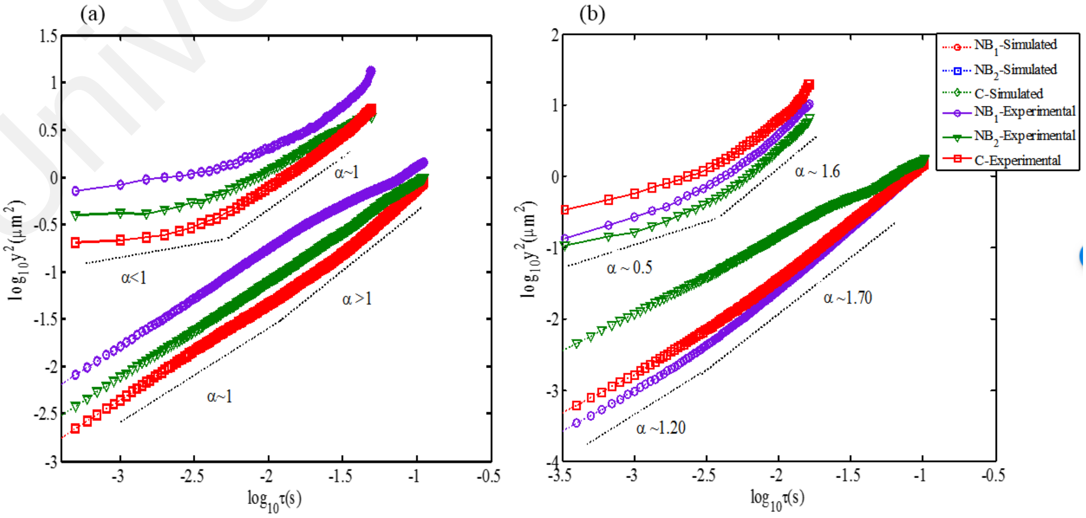

Figure 4.24: Perpendicular direction of simulated TAMSDs (dash line) and experimental TAMSDs (full line) under flow rate of (a) 0.2 µL/min and (b) 0.3 µL/min at for three different regions *NB*1 (circle), *NB*2 (triangle), and *C* (rectangle).

Under slow flow, the MSD scale as $t^{1.03}$,$t^{0.98}$, and $t^{1.00}$ for NB_1, NB_2, and *C*, respectively as seen in Figure (4.24), corresponds to slow transport. In long time, it changes to faster dynamic $t^{1.54}$, $t^{1.58}$, and $t^{1.10}$. The scaling exponent in both near wall boundary regions NB_1, NB_2, and *C*, respectively shows the Brownian motion behavior and weak sub-diffusion behavior before changing to strong super-diffusive at longer time interval.

Under fast flow at 0.3 μL/min, the particle exhibits weak super-diffusive and Brownian motion behaviors at the shorter time with MSD scale as $t^{1.22}$,$t^{1.20}$, and $t^{1.04}$ for NB_1, NB_2, and *C*, respectively as seen in Figure 4.24(b). Later in time, the particle at NB_1 and NB_2 exhibit strong super-diffusive behavior with MSD scale as $t^{1.67}$, $t^{1.69}$, while the particle at the *C* region possess weak super-diffusive mode at MSD scale of $t^{1.14}$. Similarly, particle at the near wall boundary NB_1 and NB_2 transported faster than particle located at the *C* region.

Table 4.10: Numerical MSD's results in perpendicular direction.

Simulated flow rate (μL/min)	**Cases**	$\boldsymbol{\alpha_1}$	$\boldsymbol{\alpha_2}$	$\boldsymbol{t_c}$ **(ms)**
0.2	NB_1	1.03± 0.01	1.54 ± 0.02	10.00
	NB_2	0.98 ± 0.01	1.58 ± 0.02	10.00
	C	1.00 ± 0.01	1.10 ± 0.02	10.00
0.3	NB_1	1.22 ± 0.01	1.67 ± 0.02	3.60
	NB_2	1.20 ± 0.01	1.69 ± 0.02	3.60
	C	1.04 ± 0.01	1.14 ± 0.02	3.70

The percentage difference of scaling exponent at region of NB_1 with respect to NB_2 in case of 0.2 μL/min is 5.0 % for α_1 and 2.6 % for α_2. For case, of 0.3 μL/min is 2.6 %

and 1.2 %, respectively for α_1 and α_2. The low percentage difference of scaling exponent at both short and longer time represents NB_1 and NB_2 regions is symmetric with respect to each other as predicted by the Poiseuille flow profile. Next, the percentage difference of α_1 of the region NB_1/C and NB_2/C resulting in 33.0 % and 35.8 %, respectively for slow flow, while 37.7 % and 38.8 % in case of fast flow. This large percentage difference value suggests the behavior of the particle at the *C* region was different from the region of near wall boundary of NB_1 and NB_2.

The comparison of the percentage difference of α_1 at case of fast flow obtained from both simulation and experimental is 50.3 %, 65.2 %, and 61.6% at region of NB_1, NB_2, and *C*, respectively, while the percentage difference of α_2 is 0.7 %, 0 % and 34.78 %. The reducing pattern of the percentage difference shows the behavior of the simulated particle in early time show the large disparity compared to the experimental particle and this disparity is reduced at long time scale. However, there still exist large percentage difference of the scaling exponent of the particle located at *C* region.

At the perpendicular direction, the NVACF dropped sharply to zero value and continues to oscillate at zero magnitude at long lag time. These behaviors are observed in both slow and fast flow cases as shown in Figure 4.25, which means the particle lost its memory on its previous state as the memory is de-correlated by the effect of the Brownian forces. This is in agreement with the value of *H* scaling exponent obtained at short lag time *H* = 0.5. The NVACF profiles of both cases at long lag time are plotted at $\tau = 10t_0$ (inset of Figure 4.25(a,b)) and show the positive correlation from the persistent motion. In fact, this persistent nature from the long-term memory is in line with the finding of *H* >0.5 at long time.

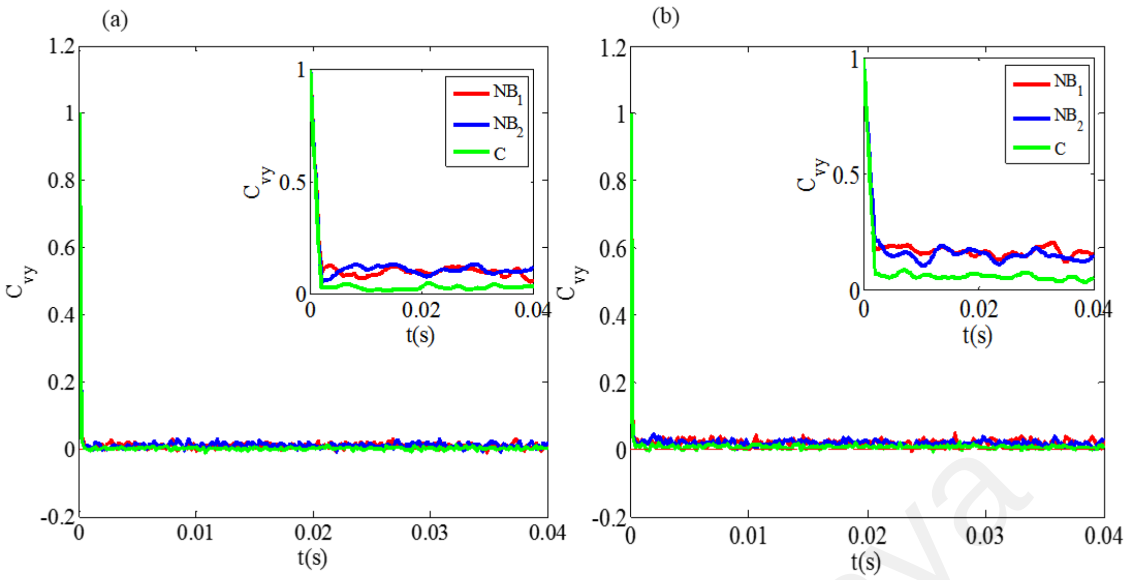

Figure 4.25: Perpendicular NVACF in flow region of *NB*$_1$(red), *NB*$_2$(blue) and *C* (green) at: (a) 0.2 µL/min, and (b) 0.3 µL/min.

4.4.3.3 Numerical resultant MSDs

The resultant MSD from the simulations are shown in Figure 4.26 where the MSDs exhibit the bi-scaling power law regime. The MSDs is scaled lowest at time interval of (t <10.00 ms) or ($t < 3.6$ ms) and scaled highest at time interval (t >10.00 ms) or ($t > 3.6$ ms). This show the transition from slow transport to the fast transport mode.

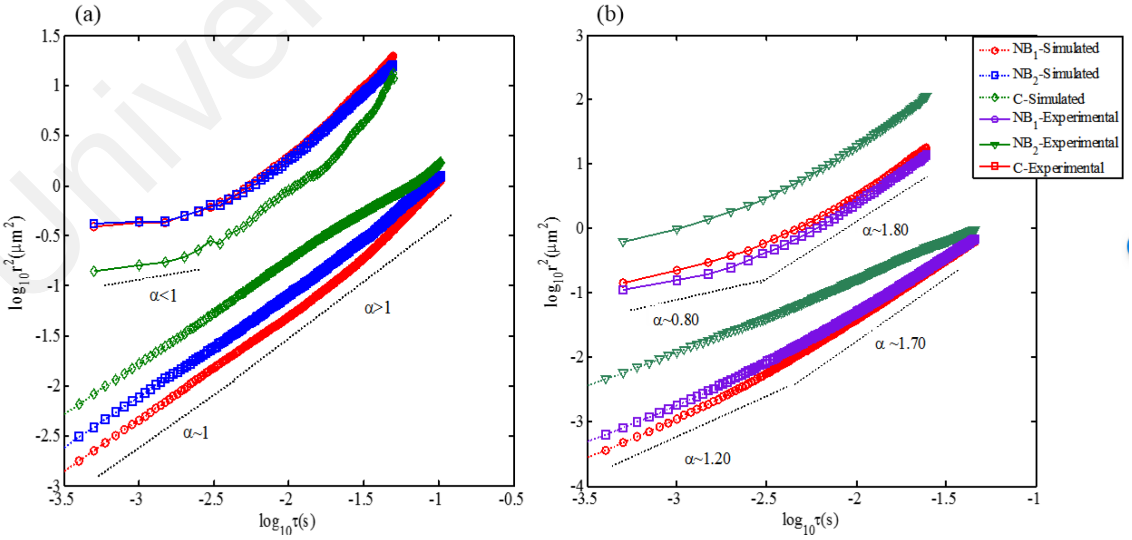

Figure 4.26 : Resultant direction of simulated averaged TAMSDs (dash line) and experimental TAMSDs (full line) under flow rate of (a) 0.2 µL/min, and (b) 0.3 µL/min at for three different regions *NB*$_1$ (circle), *NB*$_2$ (triangle), and *C* (rectangle).

The resultant MSD under flow rate of 0.2 µL/min at $NB_1$and NB_2 regions scale as $t^{1.20}$ and $t^{1.17}$, respectively which corresponds to the super-diffusive mode. While, the MSD at the C region scale as $t^{1.03}$ (Brownian motion). At long time, the MSD particle at respective flow regions of NB_1, NB_2, and C scale as $t^{1.54}$, $t^{1.58}$, and $t^{1.10}$, indicating the super-diffusive behavior. The comparison of the percentage difference at the regions of NB_1 / NB_2 with respect to C resulting in 15.2 % and 12.7 % in case of α_1, while for α_2 are 33.3 % and 35.4 %. Again, the relatively high percentage difference of α_1 and α_2 correspond to the behavior of the particle at the core region deviates from the dynamic of the particles located at near wall boundary, unlike what was observed in experimental MSDs.

Next, under fast flow of 0.3 µL/min, at short time, the particle diffused in weak super-diffusion in all the flow region as the MSD is scaled as $t^{1.33}$, $t^{1.27}$, and $t^{1.10}$. At the long time, the particle undergoes transition to the strong super-diffusion with MSD scale as $t^{1.79}$, $t^{1.81}$, and $t^{1.23}$ at respective flow regions NB_1, NB_2, and C. The percentage difference of the scaling exponent α_1 and α_2 with respect to region of near wall boundary NB_1 and NB_2 is 4.6 % and 1.1 %, respectively. The comparison of the percentage different of region NB_1/NB_2 with respect to C, is found that at short time α_1 is 18.9 % and 14.3 %, respectively, while the percentage difference α_2 at these regions are 37.01 % and 38.2 %, respectively.

The comparison of the percentage difference of scaling exponent of the numerical simulation with experiment in case of 0.2 µL/min at respective regions of NB_1, NB_2, and C give the result of 42.4 %, 70.0 % and 34.1 % for α_1 and 24.2 %, 30.5 %, and 4.2 %, respectively for α_2. The flow of 0.3 µL/min meanwhile gives the percentage difference of α_1 as 42.4 %, 43.1 %, and 14.6 % for the respective flow regions. The percentage difference of α_2 is 1.1 %, 1.64 %, and 40.7 %. The larger percentage difference of α_1

point out the large distinction of simulation particle over the experimental particle at short time. At long time, the small percentage difference of α_2 at both $NB_1$and NB_2 regions hinted the simulation results gives a good agreement with the experimental results. Noted that, there are still significant percentage difference of scaling exponent α_1 and α_2 at region *C*, implying the fallacious behavior of numerical particle behavior relative to experimental particle.

Table 4.11: Numerical MSD's results in resultant direction.

Simulated Flow rate (µL/min)	**Cases**	$\boldsymbol{\alpha_1}$	$\boldsymbol{\alpha_2}$	$\boldsymbol{t_c}$ **(ms)**
0.2	NB_1	1.20± 0.01	1.67±0.01	10.00
	NB_2	1.17 ±0.02	1.70±0.01	10.00
	C	1.03 ±0.01	1.18 ±0.01	10.00
0.3	NB_1	1.33± 0.01	1.79±0.01	3.60
	NB_2	1.27 ±0.02	1.81±0.01	3.60
	C	1.10 ±0.01	1.23 ±0.01	3.70

Clearly, the NVACF of resultant direction at both slow and fast flows manifested the positive correlation value at all time indicated the long-term memory process (Figure 4.27). This manifested in the observations of super-diffusion motion of the particle in Hurst exponents ($H > 0.5$) (refer Table 4.11). The NVACF at all respective flow regions decay at the similar rate, which is shared by both flow cases.

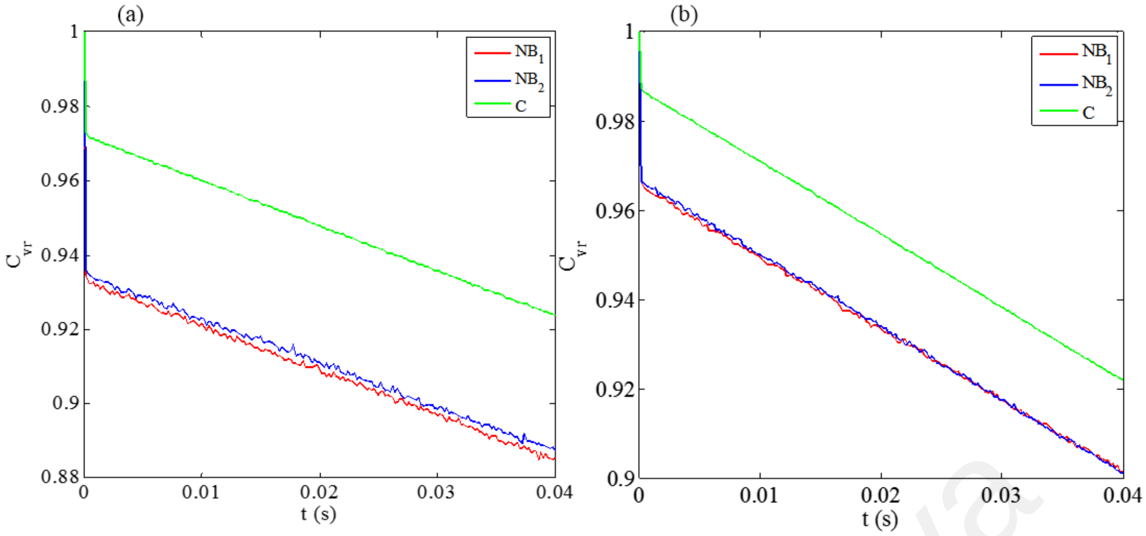

Figure 4.27: Resultant NVACF in flow region of *NB*$_1$(red), *NB*$_2$(blue) and *C* (green) at: (a) 0.2 µL/min, and (b) 0.3 µL/min.

CHAPTER 5: DISCUSSIONS

5.1 Cell characterization

Zeta potential represents the characteristics of charge on the cell surface. The measured Zeta potential of -20.1 mV suggests the presence of anionic groups, such as carboxyl and phosphate, in *C. vulgaris* membranes/cell walls (Ferreira et al., 2011). These negative surface charges also indicate that repulsive forces dominate the suspension, thus the microalgae are not expected to aggregate.

From the dynamic viscosity value, the BBM is treated as a Newtonian fluid. It should be noted, the slightly different magnitude of dynamic viscosity obtained in this study from the existing literature might be due to the different portion of the mineral used in the preparation of the BBM solution. The portion of salt and distilled water used to prepare the BBM is adjusted based on the optimization of algae culture growth.

5.2 Open domain particle tracking

The open domain is regarded as the free diffusion system, where the particles are free to diffuse or be transported without any restriction from the wall or confinement (except in *z*-direction). In this study, the free diffusing particle exhibits both slow and fast transport as shown in bi-scaling power law MSDs transitions at t = 3.0 ms. This transition is absent in the resultant direction of MSDs. The anisotropic transport of freely diffusive particle cannot be explained by the self-locomotion of the cell or the induced drift since the cell itself belongs to the non-motile algae species and any induced drift had been removed by detrending the original dataset. The possible mechanisms that might contribute to this anisotropic behavior are the viscoelastic property of the medium, the crowding environment, and “active” activity of the cell. The viscoelastic property of medium and crowding environment is known to induce the sub-diffusion of the particle by imposing cage at the spatial direction of the particle. Additionally, the “active” behavior of the cell such as repelling surface interactions between its neighbor can displace the particles in a large step, producing super-diffusion.

In open domain, the spatial directions are assigned with the reference based on the image height (y-direction) by width (x-direction). Moreover, the frame rate used in video imaging of open system is smaller than in confinement system. Thus, the necessary comparison of the free diffusing particle with the confined system is only in the resultant direction of MSDs at a long time under slow flow. Clearly, the free diffusive particle transported slower with weak sub-diffusive or nearly Brownian motion compared to super-diffusion of particle in confinement system. This faster transport of the particle in confinement is due to the presence of advection from the applied flow that helps the particle to have larger displacement and overcome the spatial restriction from the geometry of the channel.

5.3 Particle tracking in microfluidic

The fast video-imaging, particle tracking algorithm, and particle-CFD simulation are applied to investigate the dynamic of *C. vulgaris* cells motion with respect to the flow regions of flow, via the evaluation of the PDF, MSD, and NVACF. The assumption on the CFD analysis appeared to be naive and simplistic as opposed to real flow experiments, where a lot of complexities and uncertainties arise from the experiment are not properly captured in the simulation.

5.3.1 Perpendicular direction

The anomalous behavior of particle transported in both slow and fast flows is featured in the empirical distribution function of particle displacement, where the observation of highly non-stationary state at a short time interval from high kurtosis value. For long time scale, the distribution may converge to stationary Gaussian distribution as the kurtosis value decreased with increasing lag time. In this case, the particle displacement is assumed to have the quasi-Gaussian distribution. As the particle displacement distribution curve at early time exhibits the heavy tail, then the particle has higher chance to experience large displacement (super-diffusion) or having small displacement (sub-diffusion). The idea is for the sub-diffusion, the particle remains closed to its original position while in super-diffusion the particle is further away from its original position as compared to normal diffusion. The heavy tail distribution curve is common for the anomalous diffusion process (Klafter & Sokolov, 2005).

In the case of slow flow at 0.2 μL/min the observation of the strong sub-diffusive behavior of the particle at short time and weak sub-diffusion and Brownian motion at the respective flow regions of NB_1, NB_2, and C can be explained by the caging effect and dispersive transport. At small time scale, motion is sub-diffusive corresponding to thermal motion in viscoelastic medium-since the MSDs have exponent less than one. The crossover takes place at $t_c \sim 0.003$ s, which reflects the rheology and speed of the flow. The maximum scaling exponent is observed at region C, where the particle transports in accordance to normal diffusion or Brownian motion.

In the case of fast flow at 0.3 μL/min, at short time regime, the particle in all flow regions exhibit the sub-diffusion behavior and the scaling exponent shows the reducing pattern from NB_1, NB_2 to C region. Sub-diffusion NB_1 and NB_2 is due to the wall effect that restricted perpendicular displacement of particles. At the same time, channel's center sub-diffusion may occur if exist stagnation or recirculating regions in the fluid flow causing the particles to trap. Some of particles at the region C migrate quickly to the NB_1 or NB_2 where they are trapped for instant, while others move back to the C region. This has also been reported elsewhere (Yeo & Maxey, 2010). Yeo and Maxey suggested that the explanation of this behavior was due to the length scale restriction of the size of confinement that leads to the large-collective motion such as formation of hydro-cluster. In long time scale, the particle at all flow regions exhibit the super-diffusion behavior due to the irregular jump and particle entrapment in particle layers.

The introduction of t_c enabled us to characterise the dynamic of the particles at different time interval i.e. transient time. At the early transient time of $t < t_c$, the particle's inertia causes it to perform the slow dynamic. After the latter transient time $t > t_c$, the particle finally arrives at the agreement with the fluid velocity. During this excursion period, the path of the particle has high fluctuation. This dynamic is the result of the mismatch of the particle's velocity to the flow's velocity. Even the small mismatch of these velocity can give rise to the stagnation point in flow (Cartwright et al., 2010). Interestingly the transient time occurring at a different time which are t_c ~3.00 ms and t_c ~ 0.16 ms (refers to Table 4.6) for the case of 0.2 µL/min and 0.3 µL/min, respectively. These difference of t_c suggest that at slow flow, the particle takes a longer time to overcome its inertia while at the fast flow particle takes shorter time to overcome its inertia before it can be transported according to the local flow.

As stated in the previous chapter, this system belongs to the non-stationary process. Yet, the stationary process of FGN model is used to interpret the particle's velocity correlation. From the observation of the crossover MSD in the bi-logarithmic plot, via the interpretation of FBM/FGN, the time series is anti-correlated at short time, later in time it becomes persistently correlated. The anti-persistent correlation (negative correlation) is bounded within given limits value. At this limiting value, the series undergoes fluctuation in reverse direction. This bounding indicates that the velocity of the particle is (in)directly controlled (Liebovitch et al., 1997; Delignières et al., 2011). In this case, the bounded series can be considered as a stationary process (at least in long time scale), yet it cannot be treated as the genuine FGN.

The negative value of VACF increment can be attributed to the observation of sub-diffusion (anti-persistent) motion exhibited by the particle. For instance, the particle under flow of 0.2 μL/min exhibits the strong sub-diffusion and weak sub-diffusion at respective short and long time. This behavior is also manifested by the particle in the fast flow of 0.3 μL/min where it is transported sub-diffusively at short time and switched on the faster super-diffusive motion at a longer time.

The negative correlation of NVACF is associated by the backscattering of the particles due to the formation of "cage" or the collision between particles (Balucani, et al., 1996). First, the temporary cage imposed by neighboring particles may cause the particle to bounce back and forth within the cage. In this region, the particle motion is heavily affected by the cooperative motion of its immediate neighbors, which is often referred to as ``collective relaxation". The surrounding particles must relax the temporary "cage" imposed on a central particle in order for the diffusion process to proceed. This enhanced negative region was partially, responsible for the lower self-diffusion of the particle. Additionally, the "cage" can also develop due to viscoelastic properties of the medium fluid, causing the anti-correlation displacement of the particle (Despósito & Viñales, 2009). Finally, the particle might have backscattered due to the collision between other particles to produce anti-correlation (Balucani et al., 1996). In this case, there is no collision taking place in the system, as the particles only appeared to undergo displacement in accordance to the streamline and passing one another. Thus, the caging effect was most likely to take place in this system compared to the collision between the particles.

5.3.2 Streamwise direction:

In the streamwise direction, the particle located at center region has minimum interaction with the wall. On other hand, for the particle originally located at the distance h from the wall, as the distance between the particle to the wall is reduced $h < R$, the particle will interact with the wall. This particle-wall interaction altered the particle's diffusivity/scaling exponent as the particle has less free space to explore.

In the case of 0.2 μL/min, the small percentage differences of scaling exponents observed at region of NB_1 with respect to NB_2 indicate that the behaviors of the particles are symmetric at these region in contrast to the perpendicular direction case. This symmetrical nature arises because the particles dynamic in streamwise direction experienced less fluctuation. The presence of the wall restricts the space available for the particle to interact with local flow and the drag force at the normal-wall direction is higher. Thus, the scaling exponent of particle is reduced.

The percentage difference of scaling exponents of α_1 and α_2 at NB_1 and NB_2 with respect to C shows the small reduction, showing the symmetrical nature at these both regions. Exceptionally, the small reduction of the scaling exponent values of α_1 and α_2 was found at region C relative to the NB_1 region (see Table 4.7). These reduced scaling exponents in region C can be interpreted by the fact that some of the particles at center region instantly move to the NB_1 region slowing down their motion. Hence, this break downs the isotropy of the particle's MSD in the Poiseuille flow.

In the case of faster flow at 0.3 μL/min, the bi-scaling exponent perishes at all the three regions. The small percentage differences of scaling exponent at region NB_1 and NB_2 and percentage difference at regions NB_1 and NB_2 relative to C shows the behavior of the particles is symmetric as the particle are transported almost at the same rate. For the particle transported under fast flow, its dynamic is monopolized by the effect of flow advection thus minimizing the wall effect on the particle located at the both NB_1 and NB_2.

In the case of 0.2 μL/min, the negative correlation of VACF at a short time again can be associated with backscattering of particles displacement before it can overcome its inertia. At the later time as the inertia dominates the local region, the particle has a positive correlation in the displacement. For the fast flow, the VACF of the particle exhibits the positive correlation value and decorrelate at a later time. This positive correlation as indicated by the particle driven under flow rate of 0.3 μL/min exhibits the super-diffusion at both short and longer time

In both perpendicular and streamwise case, the noticeable changes in scaling behavior only occurred at the slow flow, while fast flow showed the mono-scaling behavior. Based on the SBM model the crossover time appeared at t_c ~3.00 ms which is the same as the case in the perpendicular direction. However, this transition only occurred in the case of 0.2 μL/min. This behavior is explained the *C. vulgaris* as the finite size particles undergo high fluctuations at slow flow (Usabiaga et al., 2014; Loisel et al., 2013). At $t < t_c$ a particle undergoes transient state where it spends the time to overcome its inertia before it can move according to the surrounding flow at $t > t_c$. In the case of fast flow at 0.3 μL/min, the fluctuations diminished as the result of high advective flow. Thus, the particle is able to adapt its motion with local fluid's velocity without undergoing any transient state.

As mentioned previously in Section 5.3.1, the correlation with velocity time series can still be treated via the FGN model. The positive correlation exhibited by the particle in all flow regions of NB_1, NB_2, and C in both flow cases can be explained by the effect of advective shear flow that caused the particle to have long term-memory, which then cause the velocity increment to be persistent in the sign of increment (Reverey et al., 2015).

5.3.3 Resultant MSD

As the cell displaced following the net drift from the flow, then any fluctuation from perpendicular direction must be balanced by the drift from the streamwise direction. The resultant transport behavior at a short time is greatly influenced by the behavior of the particle in the perpendicular direction, while at a long time is mostly affected by the particle dynamic in the streamwise direction. This indicates that the shear flow and confinement effect play a major role in determining the overall particle's MSDs.

In this study, two strategies are carried out to model the transient behavior of MSD via: (i) time varying diffusion coefficient as described in SBM model, and (ii) piecewise FBM. These two strategies provide the different interpretation of the mechanisms that caused the crossover between the MSDs transition. In SBM model, the changing environment as a function of time such that the time dependent viscosity or time dependent temperature can leads to the time dependent diffusion coefficient (Jeon et al., 2014). As contrast in FBM/FGN, the viscoelasticity properties of the environment is responsible for both long and short-range correlation of the system. The system has frequency dependent response to a disturbance in the environment (Jeon et al., 2014). One may ask: which strategy provides the accurate approach on describing the time dependent diffusion coefficient exhibited by *C. vulgaris* system in the confined geometry? Jeon et al. (2014) consider the distinct characteristics of the SBM and the FBM/FGN model is based on behavior of the MSD. Under confinement, the SBM shows the strongly non-stationary characteristics. For instances, the behavior of the MSD at long time interval instead of resting at the plateau value shows the power-law decay or growth resembling a "continuously decreasing or increasing temperature encoded in SBM's time dependent diffusion coefficient" (Jeon et al., 2014, p. 15814). Meanwhile, the FBM/FGN MSD tends to relax at plateau value. As shown in previous Chapter 4, all the MSDs obtained in all flow regions and cases show the increasing power law growth, and never reach the plateau. Therefore, the SBM model is more suitable to be applied in our system.

How come the temperature or viscosity of the environment changes as a function of time, as we fixed the temperature and viscosity in the experiment? We know that the diffusion coefficient D is given as Einstein-Stokes equation $D = k_BT/6\pi\eta a_{hyd}$ where η is the dynamic viscosity and a_{hyd} is the hydrodynamic radius of the particle. From this relationship, the variables that affect the diffusion are temperature, dynamic viscosity η, and hydrodynamic radius a_{hyd}. Since T is fixed at 25 ℃, the only variables left are η and a_{hyd}. The *C. vulgaris* as previously mentioned in Chapter 2 (see Section 2.5.1) released its respiratory waste products as extracellular polymeric substances (EPS) which can cause the η suspension and a_{hyd} to change over time. The EPS also can change the pH value of the environment, by increasing the acidity of the environment over time (Shen et al., 2014). It is also noted that the cell might produce the EPS in form of the biofilm that loosely attaches to cell wall as survival mechanisms in stress environment (Liu et al., 2016). As a result, the a_{hyd} differ over time. Again, as mentioned in Chapter 3; Section 3.3.3.4, we only consider the cell with average diameter of 10 μm, while the rest is eliminated during the pre-processing step. Clearly, we cannot derive a solid conclusion on the mechanism that caused the time dependent diffusion coefficient, as the algae systems itself exhibit more complex dynamic than anticipated.

5.4 Comparison of the experimental particle MSDs over the simulated particle MSDs.

Both simulated particle and experimental particle show the characteristic of transient anomalous diffusion behavior at the perpendicular direction. It is noted that the existence of transient anomalous diffusion is also observed in other studies as mentioned previously in Chapter 2; Section 2.4.3.

The real particle transported slower than the simulated particle. The slow transport of experimental particle can be argued due to: 1) finite size particle, 2) hydrodynamic interaction, 3) obstruction/wall effect, 4) local flow field and 5) cluster formation.

Clearly, massive and inertial particle transported slower compared to the point particle, thus higher fluctuation pathway of the experimental particle in the streamwise direction is observed. As for the simulated particle, due to the naïve assumption of the point particle, it behaves like passive tracers where their mass and inertia are negligible. Thus, the cells will instantaneously inherit the velocity profile from the flow of fluid. However, the *C. vulgaris* is naturally buoyant and finite-sized particle. Finite-sized particles have finite sizes and masses. Due to the particle's inertia, they are not able to instantaneously adapt themselves to the fluid's velocity as described by the Maxey-Riley equation (Maxey & Riley, 1983). It's worth to mention here that the addition of the stochastic term in the Maxey-Riley equation can give rise to the fluctuation on the path taken by the particle (Sapsis et al., 2011).

Particle-hydrodynamic interaction can reduce the particle's diffusivity/scaling exponent. For instance, in experiment of the slow flow of 0.2 µL/min, a small fraction of the microalgae was observed to be immobilized at short time interval (this particle is eliminated from the tracking process. Chapter 3; Section 3.3.3.4), which can reduce the mobility of the remaining microalgae through the hydrodynamic effect. This effect has been shown in numerical study Bussel et al., (1995) on the diffusion of tracer proteins in plasma membrane through combination of hydrodynamic and Brownian motion, where a small portion of the immobile particles can have strong effect on the remaining fraction of particle through the hydrodynamic and drag interaction. For radial separation larger than screening length, the immobile particle exerted drag on the mobile particle causing the velocity disturbance on the mobile particle. However, at the large time scale, the lateral diffusion of the algae cell is reduced due to excluded area effect and also hydrodynamic interaction. It should be noted, the inclusion of the Brownian motion or hydrodynamic interaction alone can reduce particle mobility (Saxon 1990), yet the combination of these interactions can further reduce the value of MSD coefficient. This particle-hydrodynamic interaction becomes less effective at the fast flow and long-time scale. For instance, in the case of fast flow of 0.3 μL/min, more particles are able to overcome its inertia and the cage more easily and less portion of the particles become immobilized. Thus, the particle dynamic at the long-time scale reach agreeable results for both experimental and simulation.

The comparison of scaling exponent at region NB_1/NB_2 with respect to the region C resulting the high percentage difference at early time and same order of difference at later time for both case of the flow. This behavior is explained in term of high fluctuation exist at the early time of particle's flow due to the wall effect and flow instabilities before the fluctuation diminishes at the latter time.

The observation of large percentage difference of scaling exponent at early time at the symmetric region of NB_1 and NB_2 at both flow rates imply that the particle dynamic in these regions is not symmetric. This behavior is contradicted from the assumptions on the symmetrical Poiseuille velocity flow profile. While at later time, the reducing pattern of percentage difference of α_2 indicates the behavior of the particles to be almost symmetrical. The non-symmetrical particles behavior at early time can be explained in terms of the instabilities of the local flow. In the simulation, ones can have the perfect flow symmetry with respect to the region. However, in the real experimental fluid flow, due to contribution of the local variation in the flow, thus theoretical assumption of Poiseuille is broken.

The particle located at the core region transported slowest relative to near wall regions. This behavior is due to formation of the cluster of particles at the center region. As the particles are released from the inlet, the particle located at the NB_1 and NB_2 lagged behind the particle located at the C region due to high shear rate (low velocity) of Poiseuille flow profile. As the result, the particles located at the C region with low shear rate will re-arrange themselves to form the cluster as shown in Figure 5.1, which reduces the free space (in tangential direction) that can be explored by the particle. Hence, the particle located at the C region has the lowest scaling exponent with respect to particle at the boundary region.

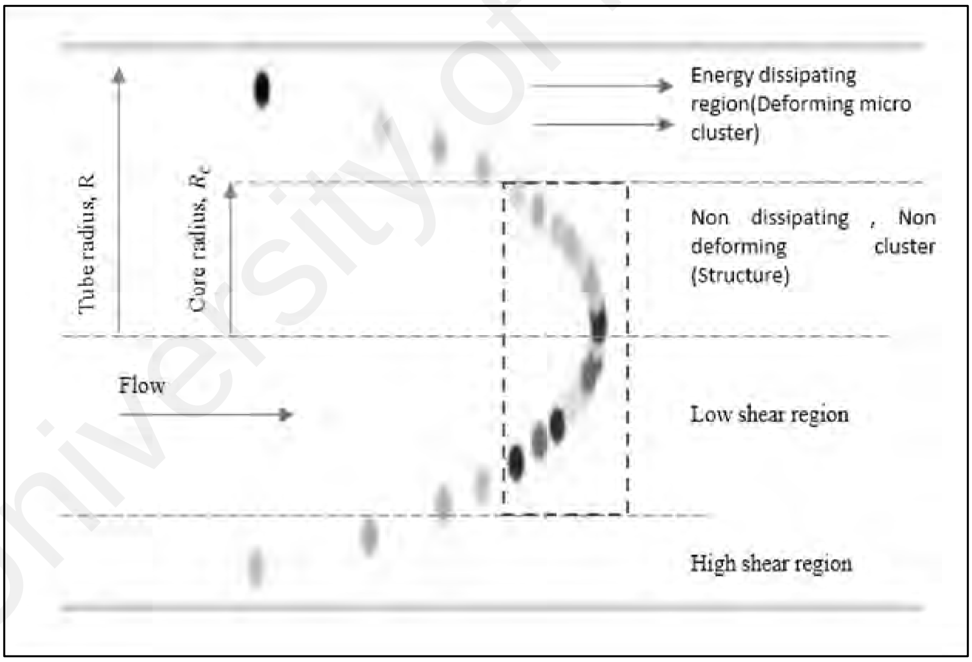

Figure 5.1: Formation of particle cluster under Poiseuille flow. Adapted from (Wetzel & Campbell, 2017).

This cluster behavior of the particles is not observed in laboratory flow experiments. In fact, the experimental particle flow according to streamline path with large distance between the neighborhood particles. It also should be noted that the experimental algae suspension behaves as dilute suspension regime and the volume fraction is assumed to have value of $\phi \sim 0.03$. Again, we argue that the cluster behavior of the particles observed in the numerical simulation belongs to the phenomena of dense particle flow in Poiseuille flow. The formation of cluster particle at the core region of the channel is observed polymer slurries flow (Wetzel & Campbell, 2017) and the red blood cell (Claverı et al., 2016) in Poiseuille flow.

The reducing diffusivity/scaling exponent in simulated particle as the particle moves towards the core regions contradict with the earlier hypothesis on the Poiseuille flow profile and experimental finding. The inverse Fax´en's law exhibited by the simulated particle is due to the fact that the particle at the center formed a cluster at the center of the flow profile. The cluster formation reduced the diffusivity of the particle since the particle is confined by its neighborhood. The dynamic is observed for the flow of concentrated suspension in Poiseuille (Wetzel & Campbell, 2017), which is not observed in the dilute suspension flow in experiment.

The limitations and sources of error of the system used in this study that may affect the accuracy of the MSD values are briefly discussed below. Among the factors that influence the microfluidic chip operation and contribute to experimental errors are the instability of the applied pressure at low flow rate, unpredictable pressure differences, alteration of pH of the suspension from the algae cell activities, and heating of solution due to constant exposure of light from illumination source. Since the flow rate plays key role in microfluidic system operation, the feedback control between the pressure controllers with flow sensor was monitored constantly. Yet, there is possibility that the particle will accumulate in the sensor capillary. Therefore, to ensure that the flow rate feedback is accurate, the device must be cleaned after use to prevent deposition of solids.

In this study, we only considered the spatial two-dimensional analysis (perpendicular and streamwise direction), hence we lost the information on the orthogonal z-direction.

This limitation is due to the restriction in probing inside the volumetric microfluidic chip. As we probed the microfluidic chip held at the stage, our observation plane is reduced. There exists the probability that some of the cells was trapped at the *z*-direction wall. However, by the careful imposition of thresholding parameters such as cell intensity, mean velocity and etc., in the pre-processing step, this type of particles are eliminated.

One critical parameter for high quality fast video-based particle tracking is the number of photons that can be detected by the camera CCD array. Higher frame rate means shorter exposures, which imply higher illumination levels, are needed. Therefore, as the frame rate increases, spatial resolution decreased. For future study, the accuracy of particle tracking experiment at the high flow rate can be improved by using coherent light source to provide high and focused illumination without damaging the cells. In addition, burst of high frame rates are also limited by computer memory, leading to small samples time and added issues in data management. The accuracy of TAMSDs calculation depends on the algorithm used for particle tracking. During the pre-processing stage, there are possibilities to artificially create spurious spots, which may lead to creation of artificial 'particles' and hence trajectories. A careful observation showed that the artificial particles due to noise-induced image artifacts are dim and smaller, while the aggregates of endogenous particles are large and bright. To improve accuracy, we manually examined the observed trajectories by closely following the consecutive frames to ensure proper trajectories were used in the determination time average mean squared displacements.

CHAPTER 6: CONCLUSIONS

In this work, we have performed detailed study on the transport of microalgae *C. vulgaris* in microfluidic channel using real experiments and computational fluid dynamics simulation.

6.1 Summary

The transport behaviors are deduced from the particle trajectories. We have examined the spatial variation of the transport behavior in different parts of the channels. The channel was divided into three different flow regions, namely center region of the channel and two near-wall boundaries and the particles' motion are analyzed at different flow rates. The trajectories of the particles are resolved into its two spatial directions and also its resultant direction. The statistical moments such as mean square displacement, probability density function and velocity autocorrelation are used to study the transport behavior of the cells.

We observed anisotropy in the diffusion characteristics across all the regions in both streamwise and tangential directions at all applied flow rates. These are seen in both experimental and numerical data. Interestingly, the microalgae particles transport undergoes transition in scaling behavior from slow dynamic at short-time to the fast dynamic at longer-time. This transition is however negligible in the streamwise direction at high flow rate. The multi-scaling features motivated us to use Scaled Brownian Motion to model the MSD. We observed that particles exhibited anomalous transport and normal transport under slow flow and retain the anomaly in fast flow. Due to the transitional effects that may be attributed to variation in fluid or particle parameters over time, such a complex behavior could not be incorporated into a rather simplistic CFD simulation that requires these properties to be fixed before the simulation.

6.2 Suggestion for future works

It will be interesting to extend the analysis via other statistical technique such as wavelet analysis and time-dependent fractal analysis to see if the transition behavior can be tracked locally in time and corroborated visually from the images. There could be crowding or jamming effects in the narrow channel that hinder motion freely. Temporal variation in the statistical properties or scaling exponents can also be captured using multifractional Brownian motion with time dependent Hurst parameter, $H(t)$, hence giving MSD ~ $t^{2H(t)}$, where $0 < H(t) < 1$ (Ayache & Vehel, 2000; Lim, 2001; Muniandy & Lim, 2001). This is an alternative multiscaling generalization of fractional Brownian motion with constant H. While this model is still in the class of Gaussian distributions, other possibility includes exploring the use of Levy walk and Levy flight to characterize large deviation and non-Gaussian statistics. Observing the transport of motile microorganisms using alternative imaging based on fluorescence microscopy has been shown to provide better resolutions to differentiate degrees of freedoms in motion. Apart from this, the inclusion of the inertial effect by the moving mesh of particle-CFD simulation or solving the Maxey-Raley equation should be able to provide detailed insight on the particle dynamics.

In perspective of application, the results of this study are useful for optimization of mixing process, spreading of the microalgae, and the flow implementation in photobioreactors. One anticipates that detailed understanding of passive or driven biomaterial transport is important for microscale process control in future micro-array photobioreactor.

REFERENCES

Al-lwayzy, S. H., Yusaf, T., & Al-Juboori, R. A. (2014). Biofuels from the fresh water microalgae Chlorella vulgaris (FWM-CV) for diesel engines. *Energies*, *7*(3), 1829–1851.

Alves, L. G. A., Scariot, D. B., Guimaraes, R. R., Nakamura, C. V., Mendes, R. S., & Ribeiro, H. V. (2016). Transient superdiffusion and long-range correlations in the motility patterns of trypanosomatid flagellate protozoa. *Public Library of Science ONE*, *11*(3), 1–17.

Ao, X., Ghosh, P. K., Li, Y., Schmid, G., Hänggi, P., & Marchesoni, F. (2014). Active Brownian motion in a narrow channel. *European Physical Journal: Special Topics*, *223*(14), 3227–3242.

Apaza, L., & Sandoval, M. (2016). Ballistic behavior and trapping of self-driven particles in a Poiseuille flow. *Physical Review E - Statistical, Nonlinear, and Soft Matter Physics*, *93*(6), 1–10.

Ariel, G., Rabani, A., Benisty, S., Partridge, J. D., Harshey, R. M., & Be'er, A. (2015). Swarming bacteria migrate by Lévy Walk. *Nature Communications*, *6*, 1–6.

Aris, A. R. (1956). On the dispersion of a solute in a fluid flowing through a tube on the dispersion of a solute in a fluid flowing through a tube. *Proceeding of the Royal Society A*, *235*, 67–77.

Ayache, A., & Vehel, J. L. (2000). The generalized multifractional Brownian Motion. *Statistical Inference for Stochastic Processes*, *3*, 7–18.

Balucani, U., Brodholt, J. P., & Vallauri, R. (1996). Analysis of the velocity autocorrelation function of water. *Journal of Physics: Condensed Matter*, *8*(34), 6139–6144.

Banks, D. S. & Fradin. C (2005). Anomalous diffusion of proteins due to molecular crowding. *Biophysical Journal*, *89*(5), 2960–2971.

Bardin, D., Martz, T. D., Sheeran, P. S., Shih, R., Dayton, P. A., & Lee, A. P. (2011). High-speed, clinical-scale microfluidic generation of stable phase-change droplets for gas embolotherapy. *Lab on a Chip*, *11*(23), 3990–3998.

Batchelor, G. K. (1977). The effect of Brownian motion on the bulk stress in a suspension of spherical particles. *Journal of Fluid Mechanics*, *83*(1), 97–117.

Bechinger, C., Di Leonardo, R., Löwen, H., Reichhardt, C., Volpe, G., & Volpe, G. (2016). Active brownian particles in complex and crowded environments. *Review of Modern Physics*, *88*(4), 1–54.

Beebe, D. J., Moore, J. S., Bauer, J. M., Yu, Q., Liu, R. H., Devadoss, C., & Jo, B.-H. (2000). Functional hydrogel structures for autonomous flow control inside microfluidic channels. *Nature*, *404*, 588–590.

Bees, M. A., & Croze, O. A. (2014). Mathematics for streamlined biofuel production from unicellular algae. *Biofuels*, *5*(1), 53–65.

Bender, C., Sottinen, T., & Valkeila, E. (2011). Fractional processes as models in stochastic finance. In G. Di Nunno & B. Øksendal (Eds.), *Advanced mathematical methods for finance* (pp. 75–103). Berlin: Springer-Verlag.

Berry, H., & Soula, H. A. (2014). Spatial distributions at equilibrium under heterogeneous transient subdiffusion. *Frontiers in Physiology*, *5*(473), 1–8.

Bodrova, A. S., Chechkin, A. V., Cherstvy, A. G., & Metzler, R. (2015). Ultraslow scaled Brownian motion. *New Journal of Physics*, *17*(6), doi:10.1088/1367-2630/17/6/063038.

Bodrova, A. S., Chechkin, A. V., Cherstvy, A. G., Safdari, H., Sokolov, I. M., & Metzler, R. (2016). Underdamped scaled Brownian motion: (non-)existence of the overdamped limit in anomalous diffusion. *Scientific Reports*, *6*, 1–16.

Bolhouse, A. M. (2010). *Rheology of Algae Slurries* (Master's Thesis). Retrieved from https://repositories.lib.utexas.edu/handle/2152/ETD-UT-2010-12-2253.

Brown, R. (1828). XXVII. A brief account of microscopical observations made in the months of June, July and August 1827, on the particles contained in the pollen of plants; and on the general existence of active molecules in organic and inorganic bodies. *Philosophical Magazine*, *4*(21), 161–173.

Bruus, H. (2015). Governing equations in microfluidics. In L. Thomas & A. Lenshof (Eds.), *Microscale acoustofluidics* (pp. 1–28). http://pubs.rsc.org/en/content/ebook/978-1-84973-671-8.

Burada, P. S., Hänggi, P., Marchesoni, F., Schmid, G., & Talkner, P. (2009). Diffusion in confined geometries. *European Journal of Chemical Physics and Physical Chemistry*, *10*(1), 45–54.

Bussell, S. J., Koch, D. L., & Hammer, D. A. (1995). Effect of hydrodynamic interactions on the diffusion of integral membrane proteins: tracer diffusion in organelle and reconstituted membranes. *Biophysics Journal*, *68*(5), 1828–1835.

Campagnola, G., Nepal, K., Schroder, B. W., Peersen, O. B., & Krapf, D. (2015). Superdiffusive motion of membrane-targeting C2 domains. *Scientific Reports*, *5*, 1–10.

Cartwright, J. H. E., Feudel, U., Károlyi, G., de Moura, A., Piro, O., & Tél, T. (2010). Dynamics of finite-size particles in chaotic fluid flows. In M. Thiel, J. Kurths, M. C. Romano, G. Károlyi, & A. Moura (Eds.), *Nonlinear dynamics and chaos: advances and perspectives. Understanding complex systems* (pp. 51–87). Berlin: Springer-Verlag.

Chebbi, R. (2015). Dynamics of blood flow: modeling of the Fahraeus- Lindqvist effect. *Journal of Biological Physics*, *41*(3), 313–326.

Chen, F., Chen, H., & Gong, X. (1997). Mixotrophic and heterotrophic growth of Haematococcus lacustris and rheological behaviour of the cell suspensions. *Bioresource Technology*, *62*(1–2), 19–24.

Chen, Y.L. (2014). Inertia- and deformation-driven migration of a soft particle in confined shear and Poiseuille flow. *Royal Society of Chemistry Advances*, *4*(34), 17908–17916.

Cheng, X., Xu, X., Rice, S. A., Dinner, A. R., & Cohen, I. (2012). Assembly of vorticity-aligned hard-sphere colloidal strings in a simple shear flow. *Proceedings of the National Academy of Sciences*, *109*(1), 63–67.

Cieśla, J., Bieganowski, A., Janczarek, M., & Urbanik-Sypniewska, T. (2011). Determination of the electrokinetic potential of Rhizobium leguminosarum bv trifolii Rt24.2 using Laser Doppler Velocimetry - A methodological study. *Journal of Microbiological Methods*, *85*(3), 199–205.

Claverı, V., Coupier, G., Misbah, C., John, T., & Wagner, C. (2016). Soft matter clusters of red blood cells in microcapillary flow : hydrodynamic versus macromolecule induced interaction. *Soft Matter*, *12*(39), 8235–8245.

Clementi, F., Mancini, M., & Moresi, M. (1998). Rheology of alginate from Azotobacter vinelandii in aqueous dispersions. *Journal of Food Engineering*, *36*(1), 51–62.

Condamin, S., Tejedor, V., Voituriez, R., Be, O., & Klafter, J. (2008). Probing microscopic origins of confined subdiffusion by first-passage observables. *Proceedings of the National Academy of Sciences of the United States of America*, *105*(15), 5675–5680.

Croze, B. O. A., Sardina, G., & Ahmed, M. (2013). Dispersion of swimming algae in laminar and turbulent channel flows : consequences for photobioreactors. *Journal of The Royal Society Interface*, *10*(81), 1–14.

Delignières, D., Torre, K., & Bernard, P. (2011). Transition from persistent to anti-persistent correlations in postural sway indicates velocity-based control. *Public Libarary of Science Computational Biology*, *7*(2), 1–10.

Despósito, M. A., & Viñales, A. D. (2009). Subdiffusive behavior in a trapping potential: Mean square displacement and velocity autocorrelation function. *Physical Review E - Statistical, Nonlinear, and Soft Matter Physics*, *80*(2), 1–7.

Einstein, A. (1905). On the motion of small particles suspended in a stationary liquid, as required by the molecular kinetic theory of heat. *Annalen Der Physik*, *17*, 549–560.

Eral, H. B., Van Den Ende, D., Mugele, F., & Duits, M. H. G. (2009). Influence of confinement by smooth and rough walls on particle dynamics in dense hard-sphere suspensions. *Physical Review E - Statistical, Nonlinear, and Soft Matter Physics*, *80*(6), 1–8.

Fehr, T., & Lowen, H. (1995). Glass transition in confined geometry. *Physical Review E-Statistical, Nonlinear, and Soft Matter Physics*, *52*(4), 4016–4025.

Fujiwara, T. K., Iwasawa, K., Kalay, Z., Tsunoyama, T. A., Watanabe, Y., Umemura, Y. M., … Kusumi, A. (2016). Confined diffusion of transmembrane proteins and lipids induced by the same actin meshwork lining the plasma membrane. *Molecular Biology of the Cell*, *27*(7), 1101–1119.

Genovese, D. B. (2012). Shear rheology of hard-sphere, dispersed, and aggregated suspensions, and filler-matrix composites. *Advances in Colloid and Interface Science*, *171*, 1–16.

Ghosh, S., Mugele, F., & Duits, M. H. G. (2015). Effects of shear and walls on the diffusion of colloids in microchannels. *Physical Review E - Statistical, Nonlinear,* *and Soft Matter Physics*, *91*(5), 1–10.

Gimel, J.C., & Nicolai, T. (2011). Self-diffusion of non-interacting hard spheres in particle gels. *Journal of Physics. Condensed Matter : An Institute of Physics Journal*, *23*(23), 1–10.

Godec, A., Bauer, M., & Metzler, R. (2014). Collective dynamics effect transient subdiffusion of inert tracers in flexible gel networks. *New Journal of Physics*, *16*(9), 1–13.

Guigas, G., Kalla, C., & Weiss, M. (2007). The degree of macromolecular crowding in the cytoplasm and nucleoplasm of mammalian cells is conserved. *Letters Federation of European Biochemical Societies Letters*, *581*(26), 5094–5098.

Gupta, A., Chow, L., Kumar, R., & Ladd, A. (2009). Effect of aspect ratio on inertial migration of neutrally buoyant spheres in a rectangular channel. In *47th AIAA Aerospace Sciences Meeting* (pp. 1–14). Orlando,Florida.

Hagen, B., Ku, F., Wittkowski, R., Takagi, D., Lo, H., & Bechinger, C. (2014). Gravitaxis of asymmetric self-propelled colloidal particles. *Nature Communications*, *5*, 1–7.

Hensley, Z. D., & Papavassiliou, D. V. (2014). Drag coefficient correction for spherical and nonspherical particles suspended in square microducts. *Industrial and Engineering Chemistry Research*, *53*(25), 10465–10474.

Ho, B., & Leal, L. (1974). Inertial migration of rigid spheres i n two-dimensional unidirectional flows. *Journal of Fluid Mechanics*, *65*(2), 365–400.

Hur, S. C., Henderson-maclennan, N. K., Mccabe, R. B., & De, D. C. (2011). Deformability-based cell classification and enrichment using inertial microfluidic. *Lab Chip*, *11*(5), 912–920.

Jeon, J.-H., Chechkin, A. V, & Metzler, R. (2014). Scaled Brownian motion: a paradoxical process with a time dependent diffusivity for the description of anomalous diffusion. *Physical Chemistry Chemical Physics : PCCP*, *16*(30), 15811-15817.

Kapaun, E., & Reisser, W. (1995). A chitin-like glycan in the cell wall of a Chlorella sp. (Chlorococcales, Chlorophyceae). *Planta*, *197*(4), 577–582.

Katayama, Y., & Terauti, R. (1996). Brownian motion of a single particle under shear flow. *European Journal of Physics*, *17*(3), 136–140.

Kaulakys, B., & Alaburda, M. (2009). Modeling scaled processes and $1/f^{\beta}$ noise by the nonlinear stochastic differential equations. *Journal of Statistical Mechanics: Theory and Experiment*, *2009*(2), 1-11.

Klafter, J., & Sokolov, I. M. (2005). Anomalous diffusion spreads its wings. *Physics World*, *18*(8), 29–32.

Kleßinger, U. A., Wunderlich, B. K., & Bausch, A. R. (2013). Transient flow behavior of complex fluids in microfluidic channels. *Microfluidics and Nanofluidics*, *15*(4), 533–540.

Koch, D. L., & Subramanian, G. (2011). Collective hydrodynamics of swimming microorganisms: Living fluids. *Annual Review of Fluid Mechanics*, *43*(1), 637–659.

Koutsoyiannis, D. (2002). The Hurst phenomenon and fractional Gaussian noise made easy. *Hydrological Sciences Journal*, *47*(4), 573–595.

Krieger, I. M., & Dougherty, T. J. (1959). A mechanism for non-Newtonian flow in suspensions of rigid spheres. *Transactions of The Society of Rheology (1957-1977)*, *3*(1), 137–152.

Kurtuldu, H., Guasto, J. S., Johnson, K. A., & Gollub, J. P. (2011). Enhancement of biomixing by swimming algal cells in two-dimensional films. *Proceedings of the National Academy of Sciences of the United States of America*, *108*(26), 10391–10395.

Lan, T., Cheng, K., Ren, T., Arce, S. H., & Tseng, Y. (2016). Displacement correlations between a single mesenchymal-like cell and its nucleus effectively link subcellular activities and motility in cell migration analysis. *Scientific Report*, *6*, 1–12.

Latini, M., & Bernoff, A. (2001). Transient anomalous diffusion in Poiseuille flow. *Journal of Fluid Mechanics*, *441*, 399–411.

Lee, C. Y., Chang, C. L., Wang, Y. N., & Fu, L. M. (2011). Microfluidic mixing: A review. *International Journal of Molecular Sciences*, *12*(5), 3263–3287.

Leptos, K. C., Guasto, J. S., Gollub, J. P., Pesci, A. I., & Goldstein, R. E. (2009).

Dynamics of enhanced tracer diffusion in suspensions of swimming eukaryotic microorganisms. *Physical Review Letters*, *103*(19), 6–9.

Leupold, M., Hindersin, S., Gust, G., Kerner, M., & Hanelt, D. (2013). Influence of mixing and shear stress on Chlorella vulgaris, Scenedesmus obliquus, and Chlamydomonas reinhardtii. *Journal of Applied Phycology*, *25*(2), 485–495.

Liebovitch, L. S., Yang, W., & Luca, D. (1997). Transition from persistent to antipersistent correlation in biological systems, *Public Library of Science Computational Biology, 56*(4), 4557–4566.

Lighthill. (1966). Initial development of diffusion in Poiseuille flow. *Journal of Applied Mathematics*, *2*(1), 97–108.

Lim, S. C. (2001). Fractional Brownian motion and multifractional Brownian motion of Riemann-Liouville type. *Journal of Physics A: Mathematical and General*, *34*(7), 1301–1310.

Lim, S. C., & Muniandy, S. V. (2002). Self-similar Gaussian processes for modeling anomalous diffusion. *Physical Review E - Statistical, Nonlinear, and Soft Matter Physics*, *66*(2), 1–14.

Lin, J., Lin, P., Chen, H., Lin, J., Lin, P., & Chen, H. (2009). Research on the transport and deposition of nanoparticles in a rotating curved pipe. *Physics of Fluids*, *21*(12), 1–12.

Liu, L., Pohnert, G., & Wei, D. (2016). Extracellular metabolites from industrial microalgae and their biotechnological potential. *Marine Drugs*, *14*(191), 1–19.

Loisel, V., Abbas, M., Masbernat, O., & Climent, E. (2013). The effect of neutrally buoyant finite-size particles on channel flows in the laminar-turbulent transition regime. *Physics of Fluids*, *25*(12), 1- 11.

Loisel, V., Abbas, M., Masbernat, O., & Climent, E. (2015). Inertia-driven particle migration and mixing in a wall-bounded laminar suspension flow. *Physics of Fluids*, *27*(12), 123304–123328.

Mandelbrot, B. B. (2010). *Fractals and scaling in finance: discontinuity, concentration, risk* (1st ed.). New York: Springer-Verlag.

Mandelbrot, B. B., & van Ness, J. W. (1968). Fractional Brownian motions , fractional noises and applications. *Society for Industrial and Applied Mathematics Review*, *10*(4), 422–437.

Marvasi, M., Visscher, P. T., & Casillas Martinez, L. (2010). Exopolymeric substances (EPS) from Bacillus subtilis: Polymers and genes encoding their synthesis. *Federation of European Microbiological Societies Microbiology Letters*, *313*(1), 1–9.

Maxey, M. R., & Riley, J. J. (1983). Equation of motion for a small rigid sphere in a nonuniform flow. *The Physics of Fluids*, *26*(4), 883–889.

Mayer, C., Moritz, R., Kirschner, C., Borchard, W., Maibaum, R., Wingender, J., & Flemming, H. C. (1999). The role of intermolecular interactions: studies on model systems for bacterial biofilms. *International Journal of Biological Macromoecules*, *26*(1), 3–16.

Mazo, R. M. (2002). *Brownian motion: fluctuations, dynamics, and applications* (1st ed.). Oxford: Oxford University Press.

Mazza, M. G. (2016). The Physics of Biofilms - An Introduction. *Journal of Physics D: Applied Physics*, *49*(20), 203001–203027.

Meijering, E., Dzyubachyk, O., & Smal, I. (2012). Methods for cell and particle tracking. *Methods in Enzymology*, *504*(9), 183–200.

Mendoza, C. I., & Santamaría-Holek, I. (2009). The rheology of hard sphere suspensions at arbitrary volume fractions: An improved differential viscosity model. *Journal of Chemical Physics*, *130*(4), 44904–44911.

Metzler, R., Jeon, J.-H., Cherstvy, A. G., & Barkai, E. (2014). Anomalous diffusion models and their properties: non-stationarity, non-ergodicity, and ageing at the centenary of single particle tracking. *Physical Chemistry Chemical Physics : PCCP*, *16*(44), 24128–64.

Molz, F. J., Liu, H. H., & Szulga, J. (1997). Fractional Brownian motion and fractional Gaussian noise in subsurface hydrology in subsurface hydrology : A review , presentation of fundamental properties , and extensions, *Water Resources Research, 33*(10), 2273–2286.

More, T. T., Yadav, J. S. S., Yan, S., Tyagi, R. D., & Surampalli, R. Y. (2014). Extracellular polymeric substances of bacteria and their potential environmental applications. *Journal of Environmental Management*, *144*, 1–25.

Muniandy, S. V., & Lim, S. C. (2001). Modeling of locally self-similar processes using multifractional Brownian motion of Riemann-Liouville type. *Physical Review E - Statistical, Nonlinear, and Soft Matter Physics*, *63*(4), 461041–461047.

Mutch, K. J., Laurati, M., Amann, C. P., Fuchs, M., & Egelhaaf, S. U. (2013). Time-dependent flow in arrested states-transient behaviour. *The European Physical Journal Special Topics*, *222*(11), 2803–2817.

Ndikubwimana, T., Zeng, X., He, N., Xiao, Z., Xie, Y., Chang, J. S., … Lu, Y. (2015). Microalgae biomass harvesting by bioflocculation-interpretation by classical DLVO theory. *Biochemical Engineering Journal*, *101*, 160–167.

Novikov, D. S., Jensen, J. H., Helpern, J. A., & Fieremans, E. (2014). Revealing mesoscopic structural universality with diffusion. *Proceedings of the National Academy of Sciences*, *111*(14), 5088–5093.

Ntefidou, M., Iseki, M., Watanabe, M., Lebert, M., & Häder, D.-P. (2003). Photoactivated adenylyl cyclase controls phototaxis in the flagellate Euglena gracilis. *Plant Physiology*, *133*(4), 1517–1521.

Nutku, F., & Aydıner, E. (2015). Current and efficiency of Brownian particles under oscillating forces in entropic barriers. *Chinese Physics B*, *24*(4), 04501–04509.

Qian, H. (2003). Fractional Brownian motion and fractional Gaussian noise. In G. Rangarajan & M. Ding (Eds.), *Processes with long-range correlations: lecture notes in physics* (pp. 22–33). Berlin: Springer-Verlag.

Quemada, D. (1977). Rheology of concentrated disperse systems and minimum energy dissipation principle - I. Viscosity-concentration relationship. *Rheologica Acta*, *16*(1), 82–94.

Reverey, J. F., Jeon, J.-H., Bao, H., Leippe, M., Metzler, R., & Selhuber-Unkel, C. (2015). Superdiffusion dominates intracellular particle motion in the supercrowded cytoplasm of pathogenic Acanthamoeba castellanii. *Scientific Reports*, *5*(2), 11690–11704.

Reynolds, C. S. (1984). *The ecology of freshwater phytoplankton*. Cambridge: Cambridge University Press.

Riley, M. A., Bonnette, S., Kuznetsov, N., Wallot, S., & Gao, J. (2012). A tutorial introduction to adaptive fractal analysis. *Frontiers in Physiology*, *3*(371), 1–10.

Roberts, A. M. (2006). Mechanisms of gravitaxis in Chlamydomonas. *Biological Bulletin*, *210*(2), 78–80.

Roberts, A. M. (2010). The mechanics of gravitaxis in Paramecium. *The Journal of Experimental Biology*, *213*(24), 4158–4162.

Rogers, S. S., Waigh, T. a, & Lu, J. R. (2008). Intracellular microrheology of motile Amoeba proteus. *Biophysical Journal*, *94*(8), 3313–3322.

Rubio, F. C., Mirón, A. S., García, M. C. C., Camacho, F. G., Grima, E. M., & Chisti, Y. (2004). Mixing in bubble columns : a new approach for characterizing dispersion coefficients. *Chemical Engineering Science*, *59*(20), 4369–4376.

Rusconi, R., & Stocker, R. (2015). Microbes in flow. *Current Opinion in Microbiology*, *25*, 1–8.

Sajeesh, P., & Sen, A. K. (2014). Particle separation and sorting in microfluidic devices: A review. *Microfluidics and Nanofluidics*, *17*(1), 1–52.

Santos-Medrano, G. E., Rico-Martinez, R., & Velázquez-Rojas, C. A. (2001). Swimming speed and Reynolds numbers of eleven freshwater rotifer species. In L. Sanoamuang, H. Segers, R. J. Shiel, & R. D. Gulati (Eds.), *Rotifera IX. Developments in hydrobiology,*(pp. 35–38). Dordrecht: Springer Dordrecht.

Sapsis, T. P., Ouellette, N. T., Gollub, J. P., & Haller, G. (2011). Neutrally buoyant particle dynamics in fluid flows: Comparison of experiments with Lagrangian stochastic models. *Physics of Fluids*, *23*(9), 093304–093320.

Schagerl, M., & Künzl, G. (2007). Chlorophyll a extraction from freshwater algae -a reevaluation. *Biologia*, *62*(3), 270–275.

Scheidler, P., Kob, W., & Binder, K. (2000). The relaxation dynamics of a simple glass former confined in a pore. *Europhysics Letters*, *52*(3), 277–283.

Scher, H., & Lax, M. (1973). Stochastic transport in a disordered solid. I. Theory. *Physical Review B - Condensed Matter and Materials Physics*, *7*(10), 4491–4502.

Schindelin, J., Arganda-Carreras, I., Frise, E., Kaynig, V., Longair, M., Pietzsch, T., …

Cardona, A. (2012). Fiji: an open-source platform for biological-image analysis. *Nature Methods*, *9*(7), 676–682.

Schmid-schonbein, B. H., Wells, R., & Goldstone, J. (1969). Influence of deformability of human red cells upon blood viscosity. *Circulation Research*, *25*(2), 131–144.

Schneider, C. a, Rasband, W. S., & Eliceiri, K. W. (2012). NIH Image to ImageJ: 25 years of image analysis. *Nature Methods*, *9*(7), 671–675.

Schubert, M., Preis, E., Blakesley, J. C., Pingel, P., Scherf, U., & Neher, D. (2013). Mobility relaxation and electron trapping in a donor/acceptor copolymer. *Physical Review B - Condensed Matter and Materials Physics*, *87*(2), 1–12.

Schuech, R., & Menden-Deuer, S. (2014). Going ballistic in the plankton: Anisotropic swimming behavior of marine protists. *Limnology and Oceanography: Fluids and Environments*, *4*(1), 1–16.

Sen, P. N. (2004). Time-dependent diffusion coefficient as a probe of geometry. *Concepts in Magnetic Resonance Part A*, *23A*(1), 1–21.

Serag, M. F., Abadi, M., & Habuchi, S. (2014). Single-molecule diffusion and conformational dynamics by spatial integration of temporal fluctuations. *Nature Communications*, *5*, 1-9.

Sharma, K. K., Schuhmann, H., & Schenk, P. M. (2012). High lipid induction in microalgae for biodiesel production. *Energies*, *5*(5), 1532–1553.

Sharma, O. P. (2007). *Textbook of algae*. New Delhi: Tata McGraw-Hill.

Shen, Y., Fan. Z.,Chen, C., & Xu, X. (2014). An auto-flocculation strategy for Chlorella vulgaris. *Biotechnology Letters*, *37*(1), 75–80.

Shevchenko, G. (2015). Fractional brownian motion in a nutshell. In *International Journal of Modern Physics: Conference Series* (pp. 1–14).

Siegle, P., Goychuk, I., Talkner, P., & Hänggi, P. (2010). Markovian embedding of non-Markovian superdiffusion. *Physical Review E - Statistical, Nonlinear, and Soft Matter Physics*, *81*(1), 1–11.

Silbert, L. E., Melrose, J. R., & Ball, R. C. (1997). Colloidal microdynamics : pair-drag simulations of model-concentrated aggregated systems. *Physical Review E*, *56*(6), 18–20.

Sokolov, I. M. (2012). Models of anomalous diffusion in crowded environments. *Soft Matter*, *8*(35), 9043–9052.

Souliès, A., Pruvost, J., Legrand, J., Castelain, C., & Burghelea, T. I. (2013). Rheological properties of suspensions of the green microalga Chlorella vulgaris at various volume fractions. *Rheologica Acta*, *52*(6), 589–605.

Spiechowicz, J., Hänggi, P., & Łuczka, J. (2016). Transient anomalous diffusion in periodic systems: ergodicity, symmetry breaking and velocity relaxation. *Scientific Reports*, *6*, 1–11.

Stone, H. A. (2007). Introduction to fluid dynamics for microfluidic flows. In : H. Lee, D. Ham, & R. M. Westervelt (Eds), *CMOS biotechnology* (1st ed., pp. 5–30). New York: Springer-Verlag.

Tabei, S. M. A., Burov, S., Kim, H. Y., Kuznetsov, A., Huynh, T., & Jureller, J. (2013). Intracellular transport of insulin granules is a subordinated random walk. *Proceedings of the National Academy of Sciences*, *110*(13), 4911–4916.

Tam, C. K. W., & Hyman, W. A. (1973). Transverse motion of an elastic sphere in a shear field. *Journal of Fluid Mechanics*, *59*(1), 177–185.

Tasadduq, B., Wang, G., El, M., Mao, W., Lam, W., Alexeev, A., & Sulchek, T. (2015). Three-dimensional particle tracking in microfluidic channel flow using in and out of focus diffraction. *Flow Measurement and Instrumentation*, *45*, 218–224.

Taylor, G. (1953). Dispersion of soluble matter in solvent flowing slowly through a tube. *Proceeding of the Royal Society A*, *219*(1137), 186–203.

Taylor, P., Havlin, S., & Ben-avraham, D. (1987). Diffusion in disordered media. *Advances in Physics*, *36*(6), 695–798.

Tinevez, J.-Y., Perry, N., Schindelin, J., Hoopes, G. M., Reynolds, G. D., Laplantine, E., … Eliceiri, K. W. (2017). TrackMate: An open and extensible platform for single-particle tracking. *Methods*, *115*, 80–90.

Usabiaga, F. B., Buscalioni, R. D., Griffith, B. E., & Donev, A. (2014). Inertial coupling method for particles in an incompressible fluctuating fluid. *Computer Methods in*

Applied Mechanics and Engineering, *269*, 139–172.

van de Ven, T. G. M. (1977). Diffusion of brownian particles in shear flow. *Journal of Colloid And Interface Science*, *62*(2), 352–355.

Vandamme, D., Foubert, I., & Muylaert, K. (2013). Flocculation as a low-cost method for harvesting microalgae for bulk biomass production. *Trends in Biotechnology*, *31*(4), 233–239.

Viner, A. B., & Kemp, L. (1983). The effect of vertical mixing on the phytoplankton of Lake Rotongaio (July 1979 -January 1981). *New Zealand Journal of Marine and Freshwater Research*, *17*(4), 407–422.

Viswanathan, G. M., Buldyrev, S. V., Havlin, S., da Luz, M. G. E., Raposo, R. P., & Stanley, H.E. (1999). Optimizing the success of random searches, *Nature, 401,* 911–914.

Viswanathan, G. M., Raposo, E. P., & Luz, M. G. E. (2008). Lévy flights and superdiffusion in the context of biological encounters and random searches. *Physics of Life Reviews*, *5*(3), 133–150.

Vlahos, L., Isliker, H., Kominis, Y., & Hizanidis, K. (2008). Normal and anomalous diffusion: A tutorial. In T.Bountis (ed.) *Order and Chaos* (Vol.10, pp. 1–39). Patras University Press.

Volpe, G., Gigan, S., & Volpe, G. (2014). Simulation of the active Brownian motion of a microswimmer. *American Journal of Physics*, *82*(7), 659–664.

von Smoluchowski, M. (1906). Zur kinetischen Theorie der Brownschen Molekularbewegung und der Suspensionen. *Annalen Der Physik*, *326*(14), 756–780.

Vonshak, A., & Borowitzka, M. A. (1991). *Laboratory manual : Research seminar and workshop on mass cultures of microalgae*. Silpakorn University, Thailand.

Walsby, A. E. (1976). The buoyancy-providing role of gas vacuoles in an aerobic bacterium. *Archives of Microbiology*, *109*(1), 135–142.

Wei, Q., & C. Bechinger, P. L. (2000). New bruce ESE file: Single-file diffusion of colloids in one-dimensional channels. *Science Magazine*, *287*(2), 625–628.

Weiss, M., Elsner, M., Kartberg, F., & Nilsson, T. (2004). Anomalous subdiffusion is a measure for cytoplasmic crowding in living cells. *Biophysical Journal*, *87*(5), 3518–24.

Wetzel, M. D., & Campbell, G. A. (2017). Characterizing the flow of slurries using percolation theory based functions. *Polymer Engineering and Science*, *57*(4), 403–416.

Willinger, W., Taqqu, M. S., Leland, W. E., & Wilson, D. V. (1995). Self-Similarity in high-speed packet traffic: analysis and modeling of ethernet traffic Measurements. *Statistical Science*, *10*(1), 67–85.

Xuan, X., Zhu, J., & Church, C. (2010). Particle focusing in microfluidic devices. *Microfluidics and Nanofluidics*, *9*(1), 1–16.

Yeo, K., & Maxey, M. R. (2010). Anomalous diffusion of wall-bounded non-colloidal suspensions in a steady shear flow. *Europhysics Letters*, *92*(2), 24008–24014.

Yukimoto, N., Tsutsui, M., He, Y., Shintaku, H., Tanaka, S., Kawano, S., … Taniguchi, M. (2013). Tracking single-particle dynamics via combined optical and electrical sensing. *Scientific Reports*, *3*, 1–7.

Zausch, J., Horbach, J., Laurati, M., Egelhaaf, S. U., Brader, J. M., Voigtmann, T., & Fuchs, M. (2008). From equilibrium to steady state: the transient dynamics of colloidal liquids under shear. *Journal of Physics: Condensed Matter*, *20*(40), 1–13.

Zheng, X., Hagen, B., Kaiser, A., Wu, M., Cui, H., Silber-li, Z., & Hartmut, L. (2013). Non-Gaussian statistics for the motion of self-propelled Janus particles : Experiment versus theory. *Physical Review E-Statistical, Nonlinear, and Soft Matter Physics*, *88*(32304), 1–11.